

Morphology and Electronic Structure of Gold Clusters on Graphite

Dissertation

Zur Erlangung des Doktorgrades der Naturwissenschaften
des Fachbereichs Physik der Universität Dortmund

vorgelegt von
Ingo Barke

November 2004

Erster Gutachter: Priv. Doz. Dr. H. Hövel
Zweiter Gutachter: Prof. Dr. M. Bayer
Tag der mündlichen Prüfung: 21.12.2004

1	INTRODUCTION	1
2	EXPERIMENTAL METHODS	5
2.1	Scanning Tunneling Microscopy.....	5
2.2	Scanning Tunneling Spectroscopy	8
2.3	Ultraviolet Photoelectron Spectroscopy.....	9
3	SHOCKLEY SURFACE STATES	12
4	PREPARATION OF AU CLUSTERS ON GRAPHITE.....	15
5	CLUSTER MORPHOLOGY	17
5.1	Small Gold Clusters.....	17
5.2	Large Gold Clusters.....	22
6	ELECTRONIC STRUCTURE.....	29
6.1	Large Clusters	29
6.1.1	Scanning Tunneling Spectroscopy.....	30
6.1.2	Photoelectron Spectroscopy	41
6.2	Small Clusters	44
7	GROWTH PROCESS.....	51
7.1	Nucleation Centers	51
7.2	Cluster Location.....	53
7.3	Photoemission Study.....	56
7.3.1	Quantitative UPS of Au Clusters	56
7.3.2	Sample Characterization	59
7.3.3	Photoemission Results	60
7.4	Growth Model.....	67
8	DYNAMIC FINAL STATE EFFECT	70
8.1	Model.....	71
8.2	Experimental Results.....	74
8.2.1	Previous Low-Temperature UPS Experiments	74
8.2.2	Photon Energy Dependence.....	76

9	INTERCOMPARISON OF SPECTROSCOPY RESULTS	83
9.1	Angle Resolved Photoemission Study	84
9.2	Sample Characterization	94
9.3	Simulation	96
10	SUMMARY AND OUTLOOK.....	104
11	APPENDIX.....	107
11.1	UPS Line Shapes for a Finite Angular Resolution.....	107
11.2	Maximum Entropy Deconvolution Techniques.....	112
11.2.1	Motivation.....	112
11.2.2	Bayesian Probability Theory	114
11.2.3	Classic Maximum Entropy Method.....	115
11.2.4	Adaptive Kernels	120
11.2.5	Smoothing.....	123
11.3	“Edge Deconvolution” Technique.....	126
12	REFERENCES.....	128

1 Introduction

For centuries people have been interested in things being too small for human senses, driven by scientific curiosity. Starting from biological cells as the building blocks of life the further exploration led to the atomic structure of matter. Later, the knowledge was extended to the internal structure of atoms, and nowadays twelve elementary particles seem to be sufficient to describe all known form of matter.

But science does not end with the search for the smallest building blocks. The creation of new objects and the investigation of their properties open a wide field of research. On the atomic scale this concept is realized in the field of nanotechnology. Utilizing physical and chemical processes, the synthesis of objects with dimensions in the range of a few nanometers has been achieved. The idea of combining a large amount of nanometer-sized objects to obtain novel macroscopic properties has been realized successfully in a variety of applications.

Matter is more than the sum of atoms. The periodicity of atoms within a three-dimensional lattice causes electronic properties completely different from the discrete states of a single atom. An important consequence is the electronic band structure of crystals which is a key property of every material. Based on the assumption of infinite periodicity the band structures of many bulk materials have been determined theoretically and experimentally with high accuracy. In the limit of very small pieces of bulk matter, i.e. so-called “clusters”, finite size effects can result in altered electronic properties. The investigation of these effects for nanometer-sized metal clusters in view of bulk condensed-matter physics is a focal point of the present work.

One of the most fascinating metals is gold. Its high monetary value, which has exerted a lasting influence on human history, is related to its extraordinary chemical and physical properties. From the practical point of view gold is a well suited material for the cluster experiments presented here because its low chemical reactivity ensures reproducibility and long measuring periods with hardly any contaminations. However, the theoretical quantum-mechanical treatment of gold often proves to be a challenge. The large atomic number leads to pronounced relativistic effects with consequences on various properties, as e.g., bond lengths, catalysis, ionization potentials, magnetic properties, and many more. Even the characteristic color of gold is determined by relativistic effects on the electron band structure [1]. The large spin-orbit coupling requires an appropriate mathematical

description, thus generally the properties of silver are easier to calculate than those of gold. Within this work the well known electronic structure of bulk gold is used for the analysis of the experimental data obtained for gold nanoclusters consisting of several thousand atoms. The electronic properties of small clusters, consisting of less than a hundred atoms are expected to deviate significantly from the bulk material. In this limit the treatment in terms of a bulk crystal fails and the theoretical description becomes extremely complex or (currently) even impossible.

In the last decades the electronic properties of free alkali metal clusters have been successfully described with methods following concepts developed in nuclear physics. The experimental mass abundance spectra of e.g. sodium clusters could be explained by closed shells of the electron configuration [2]. The electronic structure determines significantly the cluster stability and morphology (see Fig. 1a). These effects are much weaker for rare gas clusters. In that case geometric shells closings (cf. Fig. 1b) are favored which lead to icosahedral structures [3]. However, the deposition of a cluster onto a substrate reduces its symmetry, and depending on the cluster-surface interaction this may alter the geometric and electronic structure. The theoretical description of the complete cluster/surface system is extremely demanding, in addition to the difficulties mentioned above. In this work metal clusters are investigated on a graphite substrate and the role of the surface is of special interest. It will be shown that the cluster-surface interaction can result in an asymmetric broadening of spectral features obtained from photoemission experiments. For electron transport studies such as tunneling experiments independent structures can arise due to the coupling between the electrodes and the cluster.

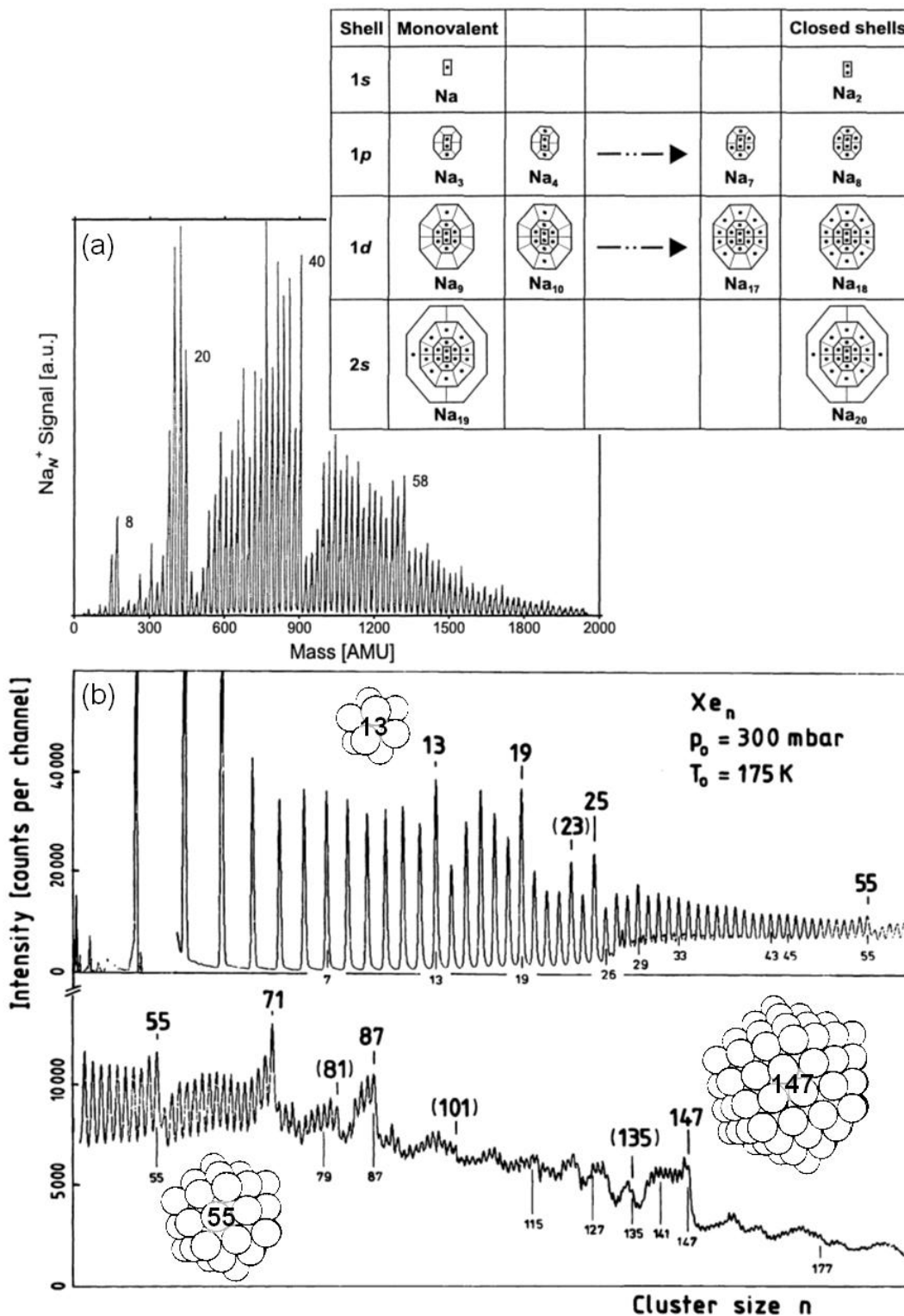


Fig. 1. (a) Mass spectrum of Na clusters. Highly stable clusters occur for “magic numbers” of atoms corresponding to closed electronic shells. In the top right corner the electron configuration arranged in analogy to the periodic table of the elements is shown. From Ref. [4].
 (b) Mass spectrum of Xe clusters. Here the magic numbers are predominantly given by closed geometric shells. The corresponding smallest 3 Mackay icosahedra are displayed with their respective number of atoms. From Refs. [3,5].

The structure of this work is as follows: in Chapter 2 the basics of the analytic techniques are described which were mainly applied in the experiments, i.e., Scanning Tunneling Microscopy and Spectroscopy, as well as Ultraviolet Photoelectron Spectroscopy. In Chapter 3 Shockley surface states are introduced which are a characteristic property of the (111) surfaces of noble metals. In a large part of this work these surface states will play a decisive role for understanding the electronic structure of the clusters. After the preparation of Au clusters on prestructured graphite is presented in Chapter 4, their geometric properties are discussed in Chapter 5. A special focus is on the electronic structure which is discussed in Chapter 6. In Chapter 7 the cluster growth process is analyzed in detail based on Scanning Tunneling Microscopy measurements and the evolution of the electronic structure in photoemission experiments. As will be shown in Chapter 8 the cluster-surface interaction affecting the photoemission process can have an important influence on photoelectron spectra of metal clusters. Finally, the combined knowledge of all effects investigated before is used in Chapter 9 in order to directly compare the photoemission and tunneling results for the same sample. For this analysis it turns out that deconvolution techniques as summarized in the Appendix are advantageous.

2 Experimental Methods

The main experimental techniques used within this work for the study of the geometric and electronic structure of clusters at surfaces are Scanning Tunneling Microscopy (STM), Scanning Tunneling Spectroscopy (STS), and Ultraviolet Photoelectron Spectroscopy (UPS). Each method requires a sophisticated analysis to account for the respective specific effects. In this section a short qualitative overview is given and the reader is referred to the literature for a more detailed and quantitative discussion. Some particular aspects concerning the experiments with supported clusters are mentioned, which will become important for the discussion in the subsequent sections.

2.1 Scanning Tunneling Microscopy

Scanning Tunneling Microscopy is a powerful method for topographic imaging in real-space. It has been developed in 1982 by Binnig and Rohrer [6,7] and has become an important tool for the surface analysis of metals or semiconductors down to atomic resolution. The basic principle is depicted in Fig. 2. An atomically sharp tip is brought in close vicinity to the sample surface and a bias voltage in the range of mV to V is applied. The resulting tunneling current, typically of the order of 1 nA, is exponentially dependent on the tip-sample distance and can thus be used to determine the topography. In the measurements presented in this work we used the constant current mode where the tunneling current serves as a control variable for a feedback loop which adjusts the tip-sample distance according to the user defined set-point current (cf. Fig. 2). The surface morphology is obtained by scanning the surface line-by-line in the lateral direction. The tip movement is realized with piezoceramic elements which are used for coarse positioning, as well as for the scanning procedure. Typical resolutions are about 100 pm in the lateral direction and 1 pm vertically. A more detailed description of STM can be found in Ref. [8].

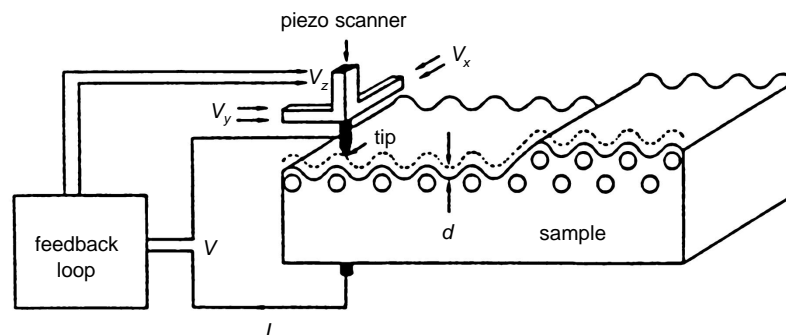


Fig. 2. Basic principle of STM. See text for details. From Ref. [9].

The STM images do not represent the surface geometry directly. For low voltages they correspond to surfaces of constant density of states at the Fermi level E_F [10,11]. In particular for the investigation of three-dimensional morphologies, such as supported clusters, the tip geometry has an important effect on the STM image. Whereas the height is determined correctly if a constant density of states is assumed, the lateral diameter is strongly overestimated (see Fig. 3). Nevertheless, in the case of flat facets on top of the clusters the facet shapes and areas can be obtained accurately from the STM measurements.

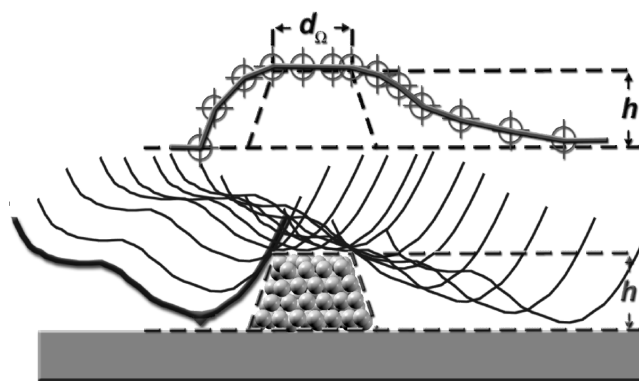


Fig. 3. Schematic representation of the tip movement across a cluster (bottom). The resulting line profile is shown at the top. It directly provides information about the cluster height h and the facet diameter d_Ω , whereas the base diameter is strongly increased by the tip.

The high electric fields between the tip and the surface ($\approx 10^{10}$ V/m) and non-ideal feedback characteristics lead to lateral forces which can be large enough to displace metal clusters on a graphite surface. In order to reduce these forces low tunneling currents of about $I = 10 \dots 100$ pA and gap voltages in the range of $V \approx 2$ V were used within this work. These settings increase the tip-surface distance and reduce the probability of tip induced

cluster displacement. However, the large voltage allows tunneling of states considerable far above or below the Fermi level (dependent on the polarity). Furthermore, the tip-surface distance becomes comparable to the cluster diameter. Using simple geometric arguments this will result in a reduction of possible tunneling paths when the tip is positioned above the cluster. As a consequence the measured height may deviate from the actual morphology. In Fig. 4 the heights of two faceted Au cluster on HOPG determined by STM is plotted versus the gap voltage. A roughly linear decrease is visible and the relative height change is similar for both clusters (Fig. 4b). Above $V \approx 4$ V the linear trend is interrupted (not shown) due to field emission resonances on the HOPG surface [12,13]. If we assume that at $V \rightarrow 0$ the actual geometric height is approached, the measured height leads to underestimated values ($\approx 10\%$) for a typical gap voltage of $V = 2$ V. This error is of the same order of magnitude as the uncertainty of the scanner calibration and the accuracy of geometric models applied for the clusters (see Sec. 5.1 and Sec. 7.2). But if one is interested in accurate absolute numbers the voltage dependent imaged heights have to be corrected according to Fig. 4.

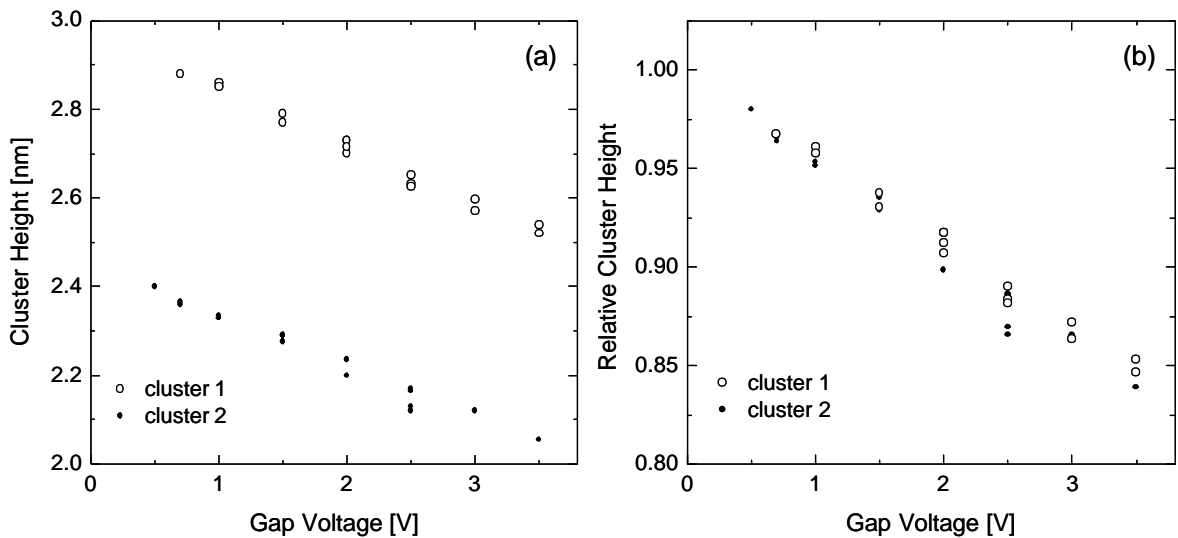


Fig. 4. (a) Measured cluster heights of two individual Au clusters for different gap voltages. Most data points have been measured several times in order to check the reproducibility. (b) The same data as in (a), normalized to the respective linearly extrapolated cluster heights at zero voltage.

2.2 Scanning Tunneling Spectroscopy

In addition to the topographic measurements the scanning tunneling microscope can be operated in the spectroscopy mode for the investigation of electronic properties of the sample system. In this case the lateral position of the tip is kept constant and the tunneling current I is measured dependent on the gap voltage V .

The electronic states involved in the tunneling process are shown in Fig. 5. For positive sample voltages the unoccupied LDOS is accessed (a) while the occupied states are measured using a negative sample bias (b).

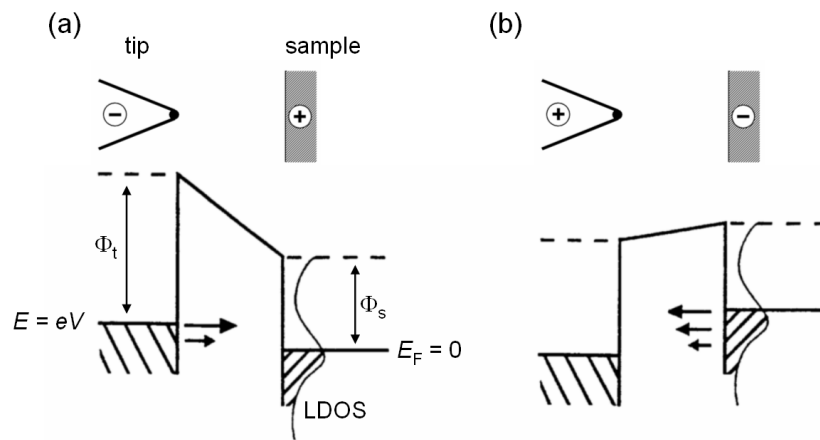


Fig. 5. Energy scheme of the tip/surface system with an external bias V for positive (a) and negative (b) sample voltages. The shape of the potential between tip and surface is dependent on the respective work functions Φ_t and Φ_s . The current I is dependent on the LDOS between the sample Fermi energy E_F and the shifted Fermi level $E_F + eV$ of the tip. The tunneling probability through the potential barrier increases for higher electron energies.

For low voltages and assuming constant tip DOS the differential conductivity dI/dV is directly proportional to the local density of states (LDOS) of the sample surface [11]. The set-point (I, V) before starting the spectroscopy procedure determines the signal amplitude according to the condition

$$I = \int_0^V \left(\frac{dI}{dV} \right)_{\tilde{V}} d\tilde{V}. \quad (1)$$

Low voltages and high currents increase the signal-to-noise ratio but they lead to more instable tunneling conditions particularly for clusters.

If the spectroscopy is repeated for several lateral tip locations the resulting data can either be displayed as a set of voltage dependent dI/dV curves or as so-called dI/dV maps. In the latter case the dI/dV values for all locations at a particular voltage are represented by a gray scale image.

In order to improve the signal-to-noise ratio, in this work a lock-in detection method is used instead of the numerical differentiation of the $I(V)$ curves [14]. A modulation voltage with an amplitude of typically $V_{\text{mod}} = 12$ mV rms is added to the tunneling voltage. The corresponding modulation of the tunneling current is detected by a lock-in amplifier which provides directly a d.c. voltage proportional to the differential conductivity dI/dV . The normalization constant can be obtained by the comparison with the numerical derivative of the simultaneously recorded $I(V)$ curve.

STS combines high energetic and spatial resolution while k resolution can only be achieved in special sample systems (e.g. standing wave patterns for surface states scattered at defects). The energy resolution at low temperatures is limited by the thermal broadening of the tip Fermi edge and may be additionally reduced by electronic noise. In our case the resolution above the temperature of liquid nitrogen ($T = 77$ K) is basically determined by the thermal broadening, thus all STS measurements presented in this work were taken at liquid helium temperature ($T_{\text{STM}} \approx 5$ K). From dI/dV curves of a superconducting Pb sample at low modulation voltages ($V_{\text{mod}} = 1$ mV rms) we estimated the energy resolution limited by electronic noise to be $s_v \approx 5$ meV. For the larger modulation amplitudes used in this work we expect an energy resolution of $s_v = 10 \dots 15$ meV. The second low-temperature effect is the enhanced stability of the tip and the sample on an atomic scale, which improves the reproducibility significantly.

2.3 Ultraviolet Photoelectron Spectroscopy

A complementary method to local STS is Angle Resolved Ultraviolet Photoelectron Spectroscopy (ARUPS). The basic principle is depicted in Fig. 6: photons, usually from a gas discharge lamp, excite electrons in the sample. Within the three-step-model [15] the excited electrons subsequently propagate through the crystal. If their energy exceeds the work function Φ they can escape from the crystal and be detected energetically and angularly resolved with an electron analyzer.

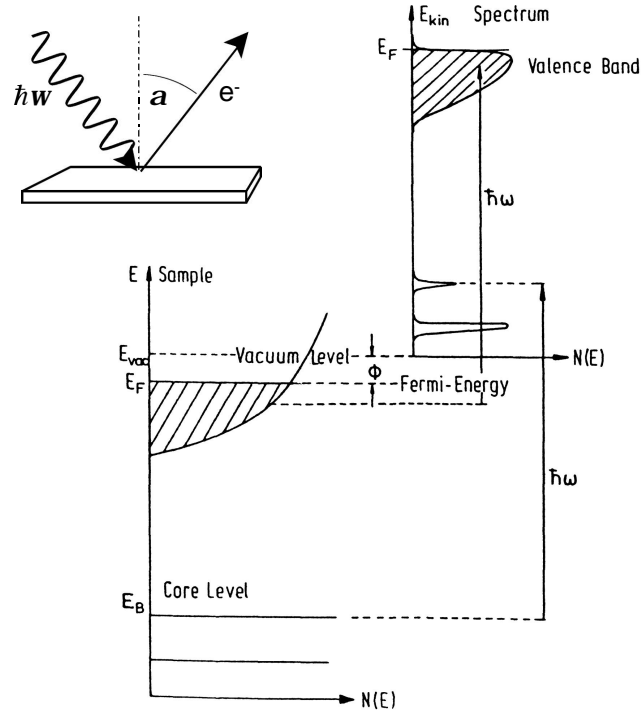


Fig. 6. Geometry (top left) and energy scheme of the photoemission process. The photon excites an electron which can be detected if it leaves the sample. For a constant final-state DOS the spectrum (right diagram) is an image of the sample DOS (bottom) at the energy according to Eq. 2. From Ref. [15].

The kinetic energy E_{kin} of the photoelectron follows the Einstein relation

$$E_{\text{kin}} = \hbar\omega - \Phi - E_b, \quad (2)$$

where $\hbar\omega$ is the photon energy and E_b is the binding energy of the electron before the photoexcitation. In this work all electron energies are given with respect to the Fermi level E_F , thus the explicit knowledge of Φ is not necessary. The energy scheme is illustrated in Fig. 6. In general the photoelectron spectrum (right hand part in Fig. 6) is proportional to the combined DOS (Joint Density Of States, JDOS) taking into account both, the initial and the final electron state. The signal amplitude is additionally modified according to the transition matrix elements between initial and final states.

Since the focus area of the electron analyzer is typically of the order of some square millimeters the UPS spectra reflect spatially averaged information of the sample properties. The variation of the electron emission angle α , however, provides access to the momentum dependent electronic structure, i.e. the dispersion $E(k_{\parallel})$. The parallel component k_{\parallel} of the momentum vector \vec{k} can be obtained directly from the kinetic energy and the emission angle because it is conserved when the electron leaves the crystal. In

contrast, the perpendicular component k_{\perp} is changed and for the reconstruction of the entire three-dimensional band structure $E(\vec{k})$ it has to be either measured (e.g. by triangulation experiments) or approximated by reasonable models [15]. In two-dimensional systems, such as the Shockley surface state (see Chapter 3), the wave vector component k_{\perp} is not defined and the two-dimensional dispersion $E(k_{\parallel})$ describes the band structure completely.

In Table 1 the characteristic properties of the methods STS and UPS as used in this work are compared to each other. In particular the combination of both techniques for the same sample facilitates a complete characterization of the spatially as well as the momentum dependent electronic structure.

STS	UPS
high energy resolution at low temperatures $\Delta E < 10$ meV	high energy resolution $\Delta E < 20$ meV
local sensitivity on an atomic scale	averages over some mm ² sample area
usually no k resolution	k_{\parallel} selectivity through choice of angle
spectroscopy of occupied and unoccupied states	only occupied states are accessible
limited energy range ($\approx \pm 5$ V)	energy range limited by photon energy
tip DOS may induce artifacts	spectrum reflects JDOS
only sensitive to the first atomic layer	detection depth ≈ 1 nm

Table 1. Characteristic Properties of STS and UPS, respectively.

3 Shockley Surface States

The experimental methods described in Chapter 2 allow to investigate the electronic structure of metal and semiconductor surfaces. One of the most prominent features of the (111) surfaces of noble metals is the Shockley surface state [16]. In the course of this work it will play a key role for the interpretation of the experimental results. Two simple models are summarized in this section, which are sufficient to reproduce the experimentally determined surface-state properties at least qualitatively. For a more detailed discussion the reader is referred to, e.g., Refs. [16-19].

Within a one-dimensional model the crystal surface can be represented by a semi-infinite chain of ionic cores with the spacing a , screened by the conduction electrons [17]. The corresponding potential is approximated by its first Fourier component (Nearly Free Electron model, NFE):

$$V(z) = -V_0 + 2V_g \cos(gz)$$

with $g = 2\pi/a$ being the reciprocal lattice vector and V_g defining the amplitude. The surface state solution of the 1D Schrödinger equation is plotted in Fig. 7 (dashed line). The electron probability density exhibits a clear maximum near the surface with an exponentially damped behavior in both directions.

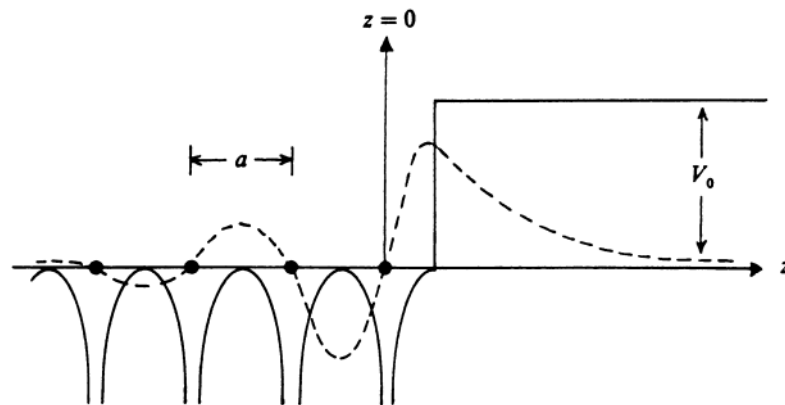


Fig. 7. Potential of a semi-infinite atomic chain as a model for a crystal surface (solid line). The wave function of the associated surface state (dashed line) decays exponentially due to the band gap (left hand side) and the work function (right hand side). From Ref. [17].

The decay of the surface state into the bulk can be interpreted in terms of the projected band gap: for the 1D chain in Fig. 7 the electron band structure exhibits a gap of the width

$2V_g$ within the NFE model. The eigenenergy of the surface state is located within this gap, and it has to decay in the direction of the crystal since these states are forbidden in the bulk. In the three-dimensional case the band gap is formed by the projection of the 3D band structure onto the surface (see Fig. 8). The existence of this gap is essential for the formation of a Shockley surface state.

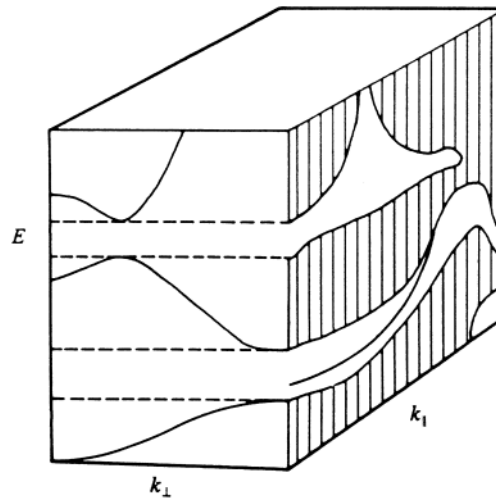


Fig. 8. Projection of the three-dimensional band structure onto the crystal surface. Shockley surface states can exist within the gaps of the surface band structure. The dispersion of a possible surface state is indicated in the lower gap. From Ref. [17].

In particular for the description of so-called image states a second model, the phase accumulation model, has been successfully applied [18,19]. Bound states occur if the overall phase of the electron wave function perpendicular to the surface satisfies the Bohr-like quantization condition

$$\Phi_C + \Phi_B = 2\pi n \quad \text{with} \quad n = 0, 1, 2, \dots$$

In this formula Φ_C and Φ_B are the phase shifts for the reflection at the crystal and the vacuum barrier, respectively. The integer n numbers the image states consecutively, and the surface state is identified by the special case $n = 0$. In Fig. 9 the potential scheme of the phase accumulation model is illustrated.

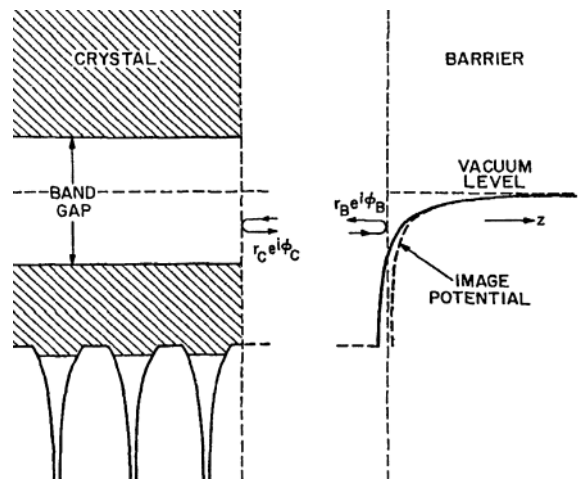


Fig. 9. Schematic representation of the phase accumulation model. See text for details. From Ref. [18].

By calculating the energy-dependent phase shifts Φ_C and Φ_B with appropriate models the energetic position of the surface state can be estimated. Unfortunately the result is sensitively dependent on the position z_0 of the surface plane. However, for a comparative analysis of the surface state for different sample systems, as e.g. rare gas layers on metal surfaces [20], the position z_0 can be used as a fit parameter.

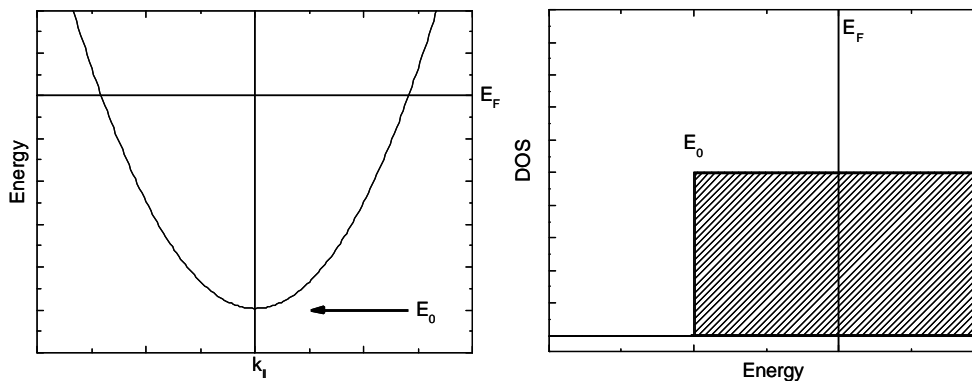


Fig. 10. Parabolic dispersion (left) and step-like density of states (right) for a free 2D electron gas.

Parallel to the surface the electron propagation is not constrained, thus the surface state can be treated as a two-dimensional free electron gas. The corresponding dispersion and the DOS are plotted in Fig. 10. In this parabolic approximation the surface state is fully characterized by the energy onset E_0 and the effective mass m^* .

4 Preparation of Au Clusters on Graphite

In the following the preparation method used for the cluster samples will be described. The clusters are grown by Au evaporation into preformed nanometer-sized pits on Highly Oriented Pyrolytic Graphite (HOPG) [21]. The HOPG substrate assures a weak cluster-substrate coupling and can easily be cleaned in UHV for low adsorbate densities. During the cluster growth the pits serve as condensation centers and allow a narrow size distribution, as well as stable imaging conditions in the STM.

In a first step the HOPG crystal is tape cleaved under ambient conditions and subsequently introduced into the UHV chamber. Annealing at a temperature of 600 °C leads to the desorption of the water film and other adsorbates. As the natural defect density is too low for the needed cluster density [21], about $5 \cdot 10^2$ surface defects per μm^2 are produced by Ar sputtering at a kinetic energy of 100 eV [22]. Outside the vacuum the defects are oxidized at $T = 540^\circ\text{C}$ to one monolayer deep pits with a diameter of a few nanometers. An atmosphere consisting of 2 % O_2 and 98 % Ar at ambient pressure is used instead of air to increase the oxidation time to $t_{\text{ox}} \approx 200$ min for a better control. The prestructured HOPG substrates are subsequently reintroduced into the UHV chamber and characterized by STM images. This allows an appropriate choice of the substrate for further experiments (e.g. high pit densities for UPS, whereas for STM/STS lower densities are feasible as well). Fig. 11 shows an overview image of a prestructured HOPG sample. The typical pit diameter is about 10 nm, but also some larger pits with irregular shapes are visible, which are partly coalesced. This is supposed to originate from catalytic etching processes during the oxidation, induced by impurities on the HOPG surface [23]. Nevertheless, these large pits are not expected to change the growth process significantly because the nucleation starts at step edges rather than in the pit centers (cf. Sec. 7.2).

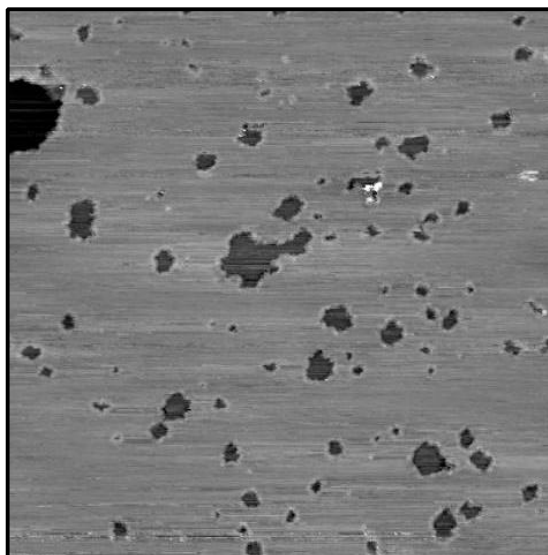


Fig. 11. Nanopits (dark areas) on a HOPG surface. Some adsorbates are imaged as bright spots. Image size: 300 nm \times 300 nm .

Prior to the metal deposition the samples are again annealed at 600 °C in the UHV to remove adsorbates which could serve as unwanted condensation centers. The gold evaporation is carried out with a rate between $3 \cdot 10^{-3}$ ML/s and $1.4 \cdot 10^{-2}$ ML/s at a sample temperature of $T = 350^\circ\text{C}$ using an electron beam evaporator with flux monitor [24]. The elevated temperature is chosen to assure a high mobility on the HOPG surface, which facilitates the formation of nearly equilibrated cluster shapes. Significantly higher sample temperatures are avoided because they result in an extremely low condensation coefficient of the gold. A small fraction of the evaporant is ionized by the electron beam in the evaporator and accelerated by the high voltage. In order to prevent the creation of additional defects induced by these cations the sample is biased at an appropriate positive voltage. In this way the cations are reflected above the sample and do not lead to disturbance of the cluster growth. By choosing different Au fluxes and evaporation times it is possible to vary the coverage over several orders of magnitude and hence to control the cluster size. The evaporator has been calibrated by adsorbing a sub-monolayer amount of gold onto a Au(111) surface [25]. Depending on the sample temperature (here $T \approx 0^\circ\text{C}$) the surface exhibits islands with an appropriate diameter in the range of some 10 nm and a height of one monolayer. The evaporation rate can be deduced from the total volume of all islands on a measured STM frame. The cluster density is essentially predetermined by the pit density. We did not find any indication that the cluster growth differs if we divide the evaporation into multiple steps. Details of the growth process and its kinetics are discussed in Chapter 7.

5 Cluster Morphology

Subsequent to the metal evaporation the samples were investigated by STM in the same UHV system. As will be shown below, it is also possible to gain information about the cluster morphology from UPS measurements. Some samples, in particular with larger clusters, were prepared for ex situ Transmission Electron Microscopy (TEM) measurements after completing the UHV experiments.

In earlier studies Ag clusters have been investigated using the same preparation and analysis methods [21,22,26-29]. For these samples neither a preferential cluster shape, nor a specific orientation was found. UPS spectra were similar to spectra of a polycrystalline Ag crystal and TEM diffraction images exhibited nearly isotropic rings. Au clusters show a different behavior. Our results indicate a transition of growth mode for clusters of about a few thousands of atoms. Consequently, the description of the morphology is divided into two sections, i.e., “small clusters” with significantly less than 10^3 atoms and “large clusters”, consisting of at least a few thousand atoms. The sections 5.1 and 5.2 give an overview of the experimental data and the analysis using different geometric models for the cluster morphology. In Chapter 7 the transition from small to large clusters is discussed in more detail in view of the growth process.

5.1 Small Gold Clusters

Fig. 12 shows the STM image of a Au cluster sample (sample A) with an exposure of about 0.1 monolayers (ML). The clusters are predominantly located at the pit edges, which is clearly visible for larger pits. Whereas the cluster width d is overestimated due to the tip shape, the height h can correctly be determined within a few percent (cf. Sec. 2.1). The statistical analysis of several measured cluster heights reveals the average cluster height $\langle h \rangle$ and the standard deviation s_h . For the sample in Fig. 12 we get $\langle h \rangle = 1.5$ nm and $s_h = 0.4$ nm based on about 300 different clusters.

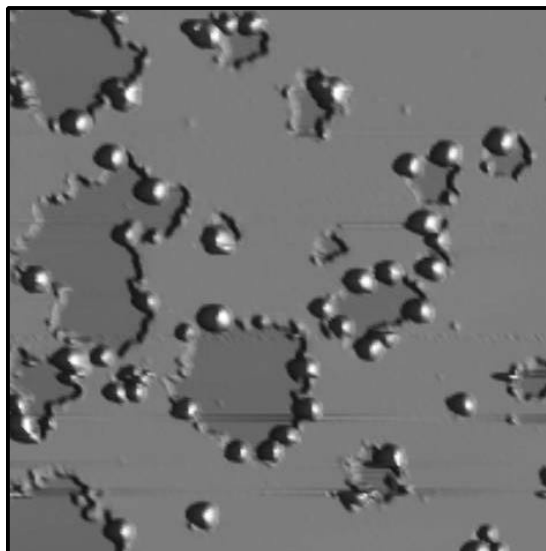


Fig. 12. Pseudo 3D image of small Au clusters on a prestructured HOPG surface with larger pits (sample A). The alignment at the pit edges is clearly visible. Image size: 150 nm \times 150 nm .

For an estimation of the cluster volume, at least the average width to height ratio $\langle d \rangle / \langle h \rangle$ is required. For larger Au clusters it is possible to obtain $\langle d \rangle$ from TEM images, but the diameter of the clusters discussed in this section is near the resolution limit of the TEM used here. One possibility is to investigate larger clusters and to extrapolate $\langle d \rangle / \langle h \rangle$ down to the smaller cluster sizes. As will be shown in the next sections, Au clusters change their morphology at a critical size which is still in the range of the TEM resolution. Earlier UPS and STM results for Ag clusters on graphite [26,28] indicate a nearly constant morphology for a broad range of cluster sizes, i.e., no preferential orientation or faceting. For these clusters we find $\langle d \rangle / \langle h \rangle \approx 1.4$. In a first approximation we assume that for the small clusters considered here the morphology does not change significantly with the cluster size, i.e., $d_i / h_i \approx \langle d \rangle / \langle h \rangle$ for each cluster. Two reasonable geometric models for the cluster shape, accounting for the fixed ratio d/h , are shown in Fig. 13. The ellipsoid model would be favored for non-wetting surfaces, i.e., with a metal-substrate interface energy comparable to sum of the respective surface energies. With $d/h = 1.4$ the truncated sphere model provides a contact angle of 115° , which is in reasonable agreement with the angle of 127° determined for μm sized particles [30]. Hence, we favor the truncated sphere model for the following discussion. The volume then can be calculated using

$$V_{\text{TS}}(h) = \mathbf{p}h^3 \left(\frac{1}{2} \frac{d}{h} - \frac{1}{3} \right). \quad (3)$$

Insertion of $d/h = 1.4$ results in $V_{\text{TS}}(h) \approx 1.15 h^3$. From this result it is evident that the relative uncertainty of the cluster volume is three times larger than for the height. Assuming that the cluster height can be determined with an accuracy about 10% (see Sec. 2.1), the error of the volume will be 30%. However, this is a systematic error which results, e.g., in an imprecise mean cluster size. For the investigation of systematic trends by comparison of different samples this error is not expected to play a major role. Nevertheless we have to keep in mind that all absolute quantities deduced from the cluster volume, such as the number of atoms per cluster N or the condensation coefficient \mathbf{b} , are influenced by a large uncertainty.

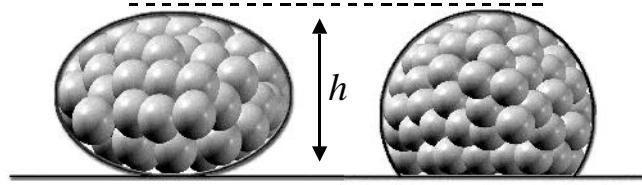


Fig. 13. Two possible geometric models for small Au clusters with given height h . Left: ellipsoidal cluster shape. Right: truncated sphere model.

From the cluster volume we get the number of atoms taking the gold bulk fcc density of 58.9 atoms/nm^3 . Potential deviations from this value are exceeded by the restricted validity of the geometric model and the accuracy of the height determination. Together with the cluster density r_C (i.e. number of clusters per area) deduced from STM or TEM images, the gold coverage Γ_{sample} on the sample and therefore the condensation coefficient $\mathbf{b} = \Gamma_{\text{sample}} / \Gamma_{\text{evap}}$ can be estimated, where Γ_{evap} is the Au exposure from the evaporator.

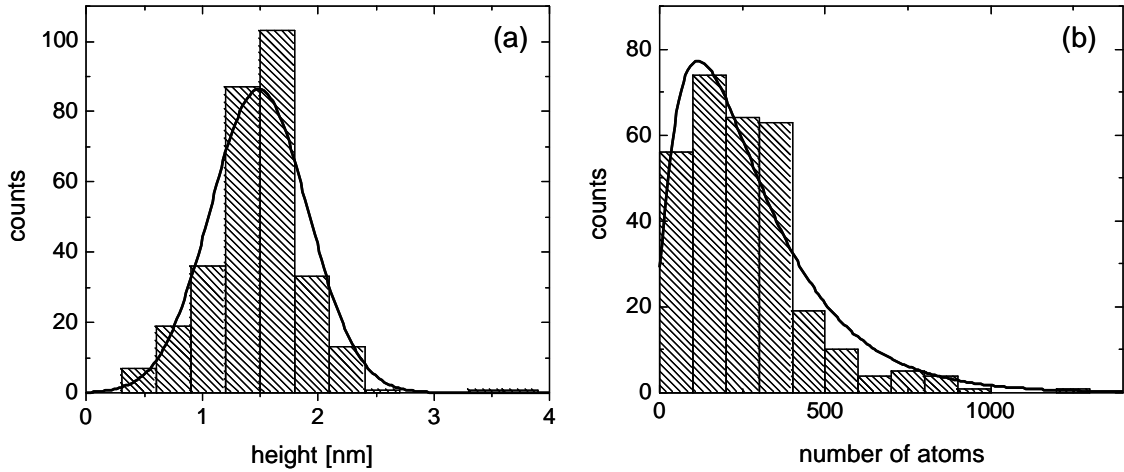


Fig. 14. (a) Histogram of measured cluster heights of sample A. The Gaussian fit (thick line) yields $\langle h \rangle = 1.49$ nm and $s_h = 0.42$ nm .
 (b) Distribution of the number of atoms calculated for each cluster using Eq. 3. The calculated curve (thick line, see Eq. 5) clearly shows the asymmetric shape of the probability density.

Due to the broad height distribution the average volume can not be deduced using the average height, but the full distribution has to be considered. In addition, the asymmetric shape of the resulting size distribution (Fig. 14b) leads to asymmetric errors which can be estimated using

$$s_N^+ = N(\langle h \rangle + s_h) - N(\langle h \rangle) \quad \text{and} \quad s_N^- = N(\langle h \rangle) - N(\langle h \rangle - s_h) \quad (4)$$

$$\text{with} \quad N(h) = 58.9 \text{ nm}^{-3} \cdot V_{\text{TS}}(h) \equiv c \cdot h^3 ; \quad c = 67.8 \text{ nm}^{-3} .$$

Assuming a Gaussian height distribution, the resulting distribution for N transforms to

$$P(N) = P(h) \frac{dh}{dN} = \frac{\sqrt{2}}{6\sqrt{p}} \frac{1}{c s_h} \left(\frac{N}{c} \right)^{-2/3} \cdot \exp \left(- \frac{1}{2} \frac{\left(\left(\frac{N}{c} \right)^{1/3} - \langle h \rangle \right)^2}{s_h^2} \right) . \quad (5)$$

Inserting the parameters for the height distribution of sample A, we get $\hat{N} \approx 120$ for the most probable cluster size. Due to the asymmetric shape (cf. Fig. 14b) the mean value is $\langle N \rangle \approx 280$ and even clusters consisting of more than thousand atoms can be found with the STM.

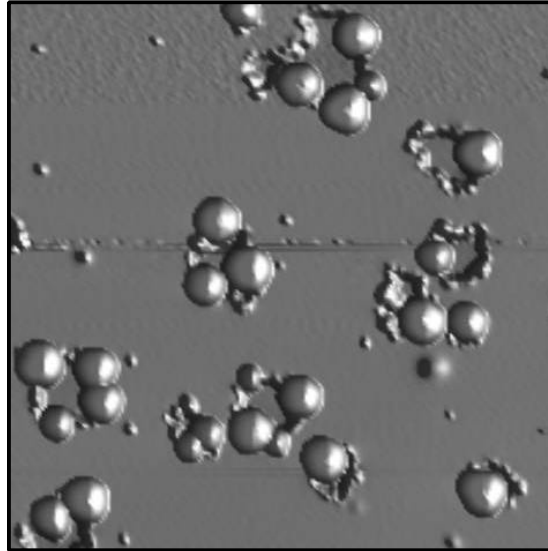


Fig. 15. Pseudo 3D image of the same sample as in Fig. 12 after an additional evaporation step (sample B). Image size: $100\text{ nm} \times 100\text{ nm}$.

An increase of the Au coverage results in larger clusters, whereas the number of clusters essentially remains constant (cf. Chapter 7). A STM image of sample A after an additional Au exposure of about 0.13 ML is shown in Fig. 15 (sample B). In Table 2 the results of the two samples A and B are summarized. Note that the condensation coefficient carries a large error because the systematic absolute uncertainty of 30 % is directly transferred to \mathbf{b} .

	Sample A	Sample B
Au exposure:	$\Gamma_{\text{evap}} = 0.10\text{ ML}$	$\Gamma_{\text{evap}} = 0.23\text{ ML}$
Cluster density:	$r_{\text{c}} = (1800 \pm 100)\text{ nm}^{-2}$	$r_{\text{c}} = (1600 \pm 100)\text{ nm}^{-2}$
height distribution:	$h = (1.5 \pm 0.4)\text{ nm}$	$h = (2.1 \pm 0.4)\text{ nm}$
number of atoms (TS):	$N = 280^{+470}_{-200}$	$N = 700^{+400}_{-380}$
condensation coeff.:	$\mathbf{b} \approx 0.32$	$\mathbf{b} \approx 0.35$

Table 2. Evaporated Au amount and sample properties as measured by STM for samples A and B (cf. Fig. 12 and Fig. 15). The number of atoms per cluster was estimated using the truncated sphere (TS) model. The quoted errors are the standard deviations of the respective distributions.

5.2 Large Gold Clusters

At high Au exposures of more than 0.5 ML we observe regular cluster morphologies with flat, almost hexagonal facets on top. Fig. 16 shows a STM image of a cluster sample after evaporation of 0.9 ML gold (sample C). The actual Au coverage on the sample is significantly lower due to the low condensation coefficient $b < 1$ (see below).

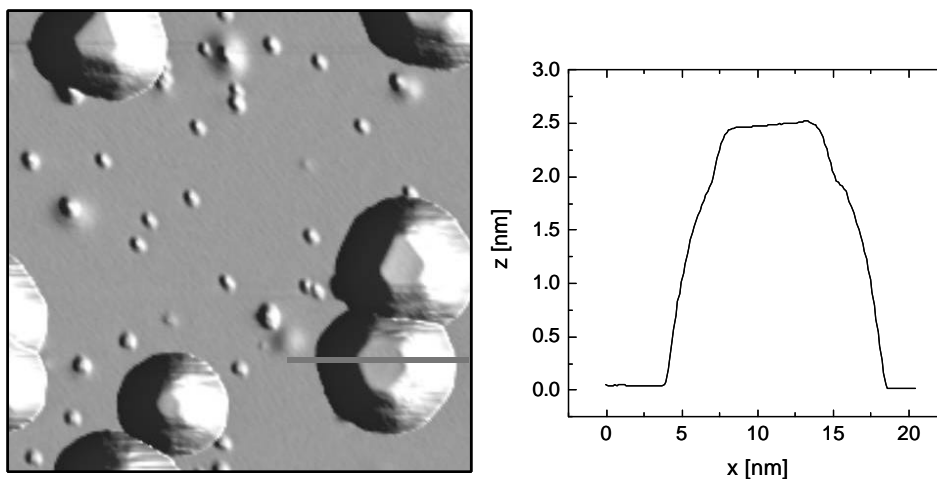


Fig. 16. Left: STM image of large, faceted Au clusters on HOPG (sample C). Image size: 50 nm \times 50 nm. Right: Line profile through a cluster as marked on the left side.

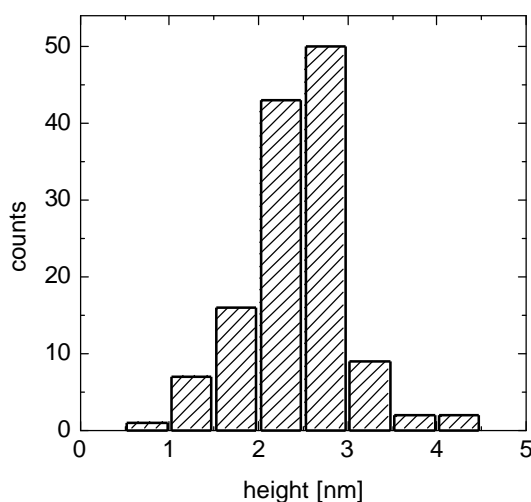


Fig. 17. Height distribution deduced from about 130 different Au clusters of sample C.

In the STM image as well as in the line scans the flat facets can clearly be identified (Fig. 16). From several measured images we get an average cluster height $\langle h \rangle = 2.4$ nm with a standard deviation of $s_h = 0.4$ nm. In Fig. 17 the height distribution of sample C is

displayed. Another interesting statistical quantity is the cluster density r_C , i.e., the number of clusters per area. For the clusters discussed in this section r_C is difficult to determine by means of STM because the probability of tip induced cluster displacement grows strongly with increasing cluster size, leading to underestimated values for r_C . This experimental difficulty is important in particular for larger image sizes, which would be necessary for a statistically accurate analysis. On the other hand also the combination of many smaller topographic measurements is not suited for this analysis due to the unavoidable arbitrary choice of the image location: areas with hardly any clusters are preferentially not imaged and thus do not contribute to the statistics. To overcome these problems, we have applied ex situ TEM for some of the cluster samples after completing the UHV experiments. The measurements were done in cooperation with Dr. Frank Katzenberg (*Fachbereich Bio- und Chemieingenieurwesen*, University of Dortmund). From the TEM image for sample C (Fig. 18) we deduce a cluster density of $r_C = (1390 \pm 70) \mu\text{m}^{-2}$. The error results from the finite number of cluster counts.

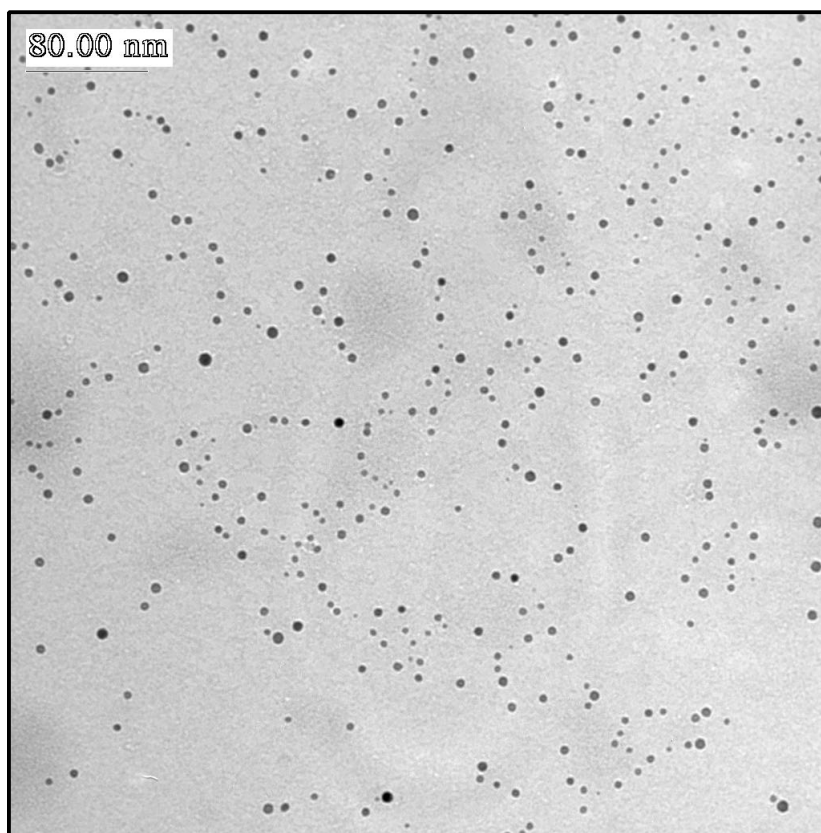


Fig. 18. TEM image of sample C (cf. Fig. 16). The Au clusters are visible as dark spots on the bright background of the HOPG substrate. Image size: 540 nm \times 540 nm .

The orientation of the facets can be determined by TEM diffraction [31] or UPS measurements. Fig. 19 displays an electron diffraction pattern of large gold clusters on HOPG. The most intense ring belongs to the (220) direction, while the (111) ring is much weaker. Additionally, we notice the high index rings (422) and (440) which have already very low intensity for clusters produced by gas aggregation and deposited on the substrate [31]. The high energy electrons in TEM are reflected at the lattice planes almost in grazing incidence. Therefore, only lattice planes perpendicular to the sample surface contribute to the diffraction pattern. The (220), (422) and (440) diffraction rings are the first three belonging to lattice planes perpendicular to the (111) plane. This shows that the clusters are oriented with their (111) plane parallel to the HOPG (0001) surface. The occurrence of diffraction rings instead of discrete spots points to a random lateral orientation. Further investigation of the lateral orientation by STM images of faceted Au clusters also do not favor a particular lateral direction [24].

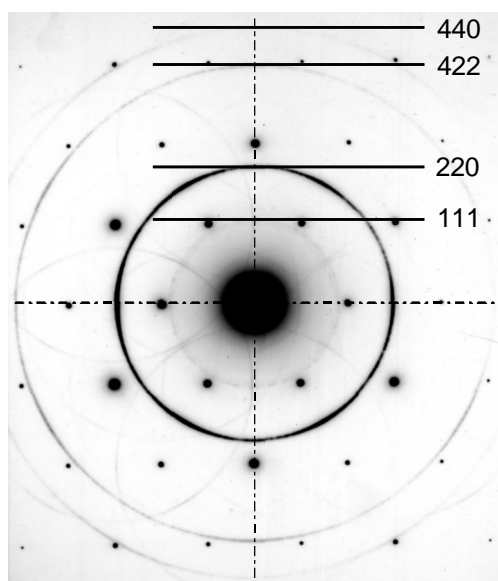


Fig. 19. Electron diffraction pattern of large Au clusters on HOPG. The observed (220), (422), and (440) rings belong to lattice planes perpendicular to the (111) direction. Data from Ref. [31].

The diffraction measurements have to be done *ex situ* which is cumbersome and destructive due to the necessary sample thinning procedure and the transport under ambient conditions. However, the distinction of different orientations is also possible by using *in situ* UPS measurements. The d-band photoelectron spectrum of another cluster sample (sample D) in normal emission is shown in Fig. 20a. For this sample we used similar preparation parameters as for sample C (see Sec. 6.1 for details). The extraction of the Au

signal is done by subtracting the corresponding spectrum of the bare HOPG substrate (see Fig. 20b). This is justified because the relative projected area of the clusters for all samples is below 10 % (cf. Sec.7.3.3). For the larger clusters we introduced a weighting factor, i.e., we subtracted only a fraction of the HOPG intensity to account for the increased Au covered area. The weighting factor was adjusted such that the prominent HOPG structure at $E \approx -8.5$ eV vanishes in the difference spectrum.

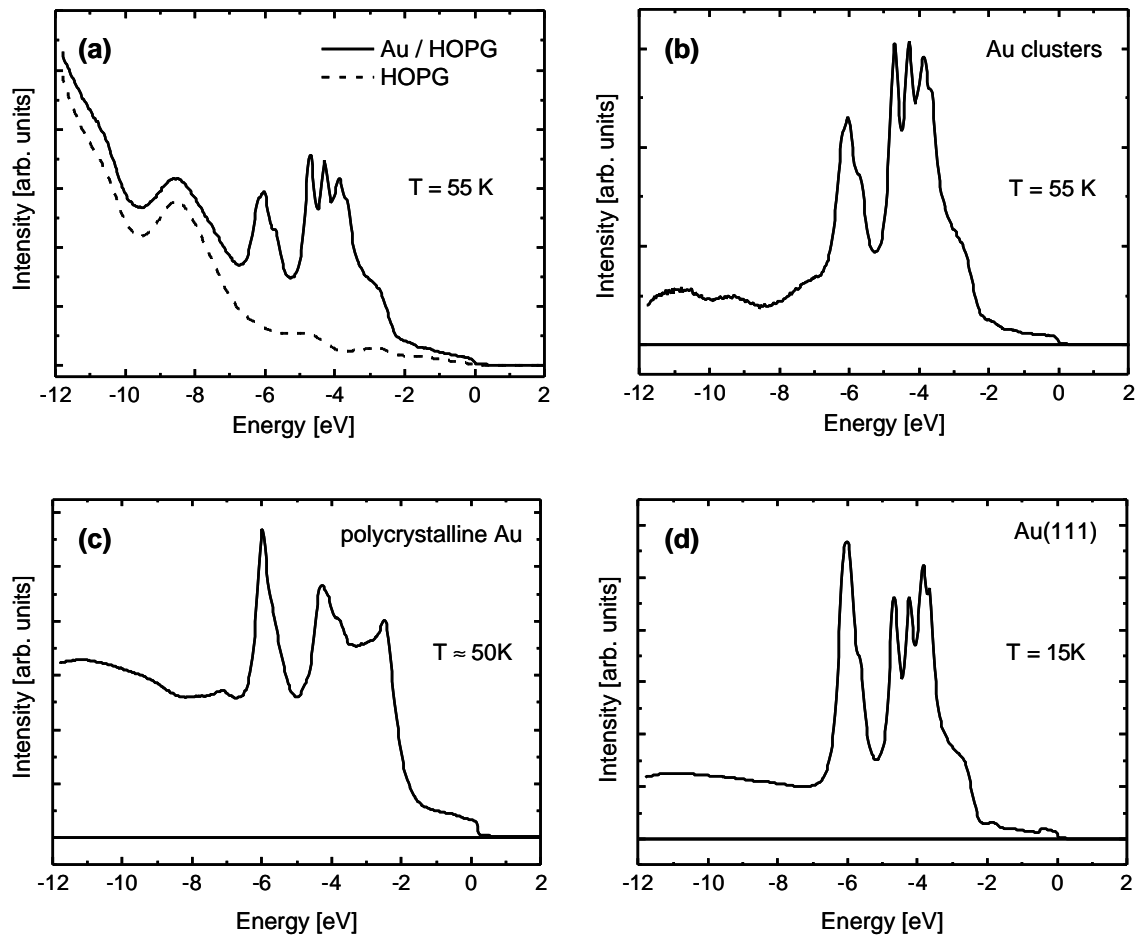


Fig. 20. (a) UPS spectra of the Au d-band structure for sample D with about 1.3 ML evaporated Au. Solid curve: measured spectrum of the cluster sample. Dashed curve: spectrum of the bare HOPG substrate. (b) Difference signal of the two spectra in (a). (c) UPS signal of a polycrystalline gold sample. (d) UPS signal of a Au(111) single crystal. Note the similarity to (b).

The comparison of the cluster spectrum with spectra of a bulk Au(111) surface and a polycrystalline gold sample, respectively, gives evidence for the (111) orientation of the cluster facets. In this way the normal emission UPS d-band spectrum can be used as a fingerprint to identify the crystal orientation. The relative peak intensity between the triple

peak at $E \approx -4$ eV and the peak at $E \approx -6$ eV is different for the Au clusters than for the bulk surface. This may be partly related to the energy dependent escape length of the photoelectrons (see Sec. 7.3.1). For very large clusters the ratio approaches the bulk value (cf. Fig. 47).

Though the overall cluster shape is strongly modified by the tip geometry (cf. Sec. 2.1), the facet shape and its area can be determined correctly from the images. The facet shapes could be classified into four different types which are shown in Fig. 21. Type I and II display a symmetry which is in accordance with the expected shapes for a small fcc crystallite while type III and IV cannot be identified with a corresponding equilibrium morphology [25]. This points to cluster coalescence during the growth process.

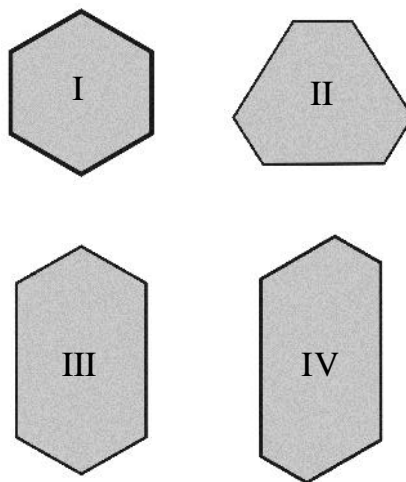


Fig. 21. The four different facet types observed for large Au clusters on HOPG. See text for details.

We have measured the cluster height as well as the facet area Ω for more than 100 clusters on sample C. In Fig. 22 the corresponding diameter $d_{\Omega} = 2\sqrt{\Omega/\rho}$ of a circle with the same area Ω is plotted versus the cluster height. It is remarkable that we could not find any faceted clusters below a cluster height of about 1 nm. We emphasize that despite the faceting the cluster morphology is still three-dimensional. This becomes evident by the combination of STM and TEM of the same sample. The average lateral cluster diameter from the TEM data is $\langle d \rangle = 5.1$ nm. Together with the STM results for the heights we obtain $\langle d \rangle / \langle h \rangle = 2 \dots 3$, in contrast to other, more two-dimensional systems like Ag/Ag(111) ($\langle d \rangle / \langle h \rangle \approx 40$) [32] or Pd/Al₂O₃ ($\langle d \rangle / \langle h \rangle \approx 5$) [33].

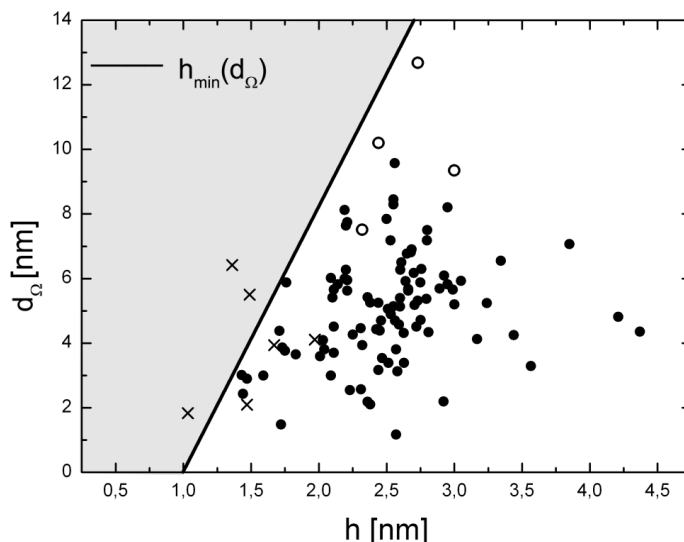


Fig. 22. Facet diameter d_{Ω} versus cluster height h of 104 faceted Au clusters on sample C, determined by means of STM. The open circles indicate clusters with facets of type III or IV (cf. Fig. 21). Their large facet area and asymmetric facet shape can be explained by coalescence processes. The straight line $h_{\min}(d_{\Omega})$ gives a lower limit for the observed cluster heights in dependence on the facet diameter. The crosses indicate clusters grown in pits with a depth of more than 1 ML, therefore their height, measured with respect to the surface, is underestimated.

To obtain a more complete view of the three-dimensional cluster morphology we additionally used geometric models. Knowing the (111) orientation of the top facets, a reasonable model for the large gold clusters is a truncated octahedron [25], which corresponds to the closed-packed fcc lattice. The volume of a truncated octahedron with given height h and facet area Ω (Fig. 23) evaluates to

$$V_{TO} = 0.217 \cdot h^3 + 0.987 \cdot h^2 \sqrt{\Omega} + h\Omega. \quad (6)$$

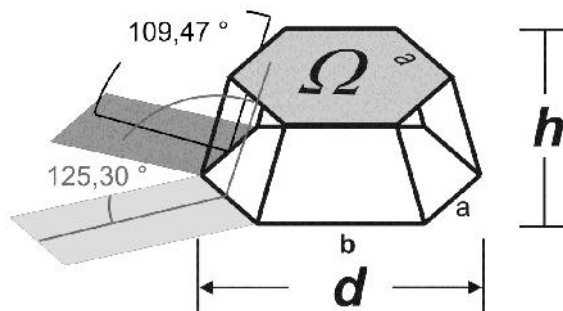


Fig. 23. Truncated octahedron model for the morphology of faceted Au clusters.

In many cases the facet shape of the measured clusters deviates from the perfect hexagon (cf. Fig. 16). Nevertheless, the calculated cluster volume is exact within a few percent, which has been checked by calculating the volume of an asymmetric “octahedron” correctly for the clusters with most asymmetric facets [25].

Alternatively, the facet can be approximated by a circle, leading to a truncated cone for the cluster morphology [34]. The apex angle is chosen to be 60° , which is a reasonable approximation for the (111) and (100) side facet angles of 70.5° and 54.7° , respectively. The cluster volume is then

$$V_{TC} = 0.349 \cdot h^3 + 1.023 \cdot h^2 \sqrt{\Omega} + h\Omega, \quad (7)$$

which differs only a few percent from the octahedron volume for our samples. With these geometric models we can evaluate the number of atoms for each cluster solely using STM data. As a consequence, the entire deposited Au amount Γ and therefore the condensation coefficient \mathbf{b} can be estimated by summing up the volume of all clusters in a certain sample area. A summary of the distribution of measured facet areas and cluster sizes for sample C is given in Table 3. The discussion will be continued using UPS data and introducing a growth model in Chapter 7.

Sample C (Au exposure: $\Gamma_{\text{evap}} = 0.92 \text{ ML}$)			
height distribution:		$h = (2.4 \pm 0.6) \text{ nm}$	
facet areas:		$\Omega = (23 \pm 18) \text{ nm}^2$	
number of atoms (TO):	$N = 5450 \pm 3850$	number of atoms (TC):	$N = 5650 \pm 3930$
cond. coeff. (TO):	$\mathbf{b} \approx 0.47$	cond. coeff. (TC):	$\mathbf{b} \approx 0.49$

Table 3. Some statistically determined data of the cluster sample shown in Fig. 16.

The given errors are deduced from the width of the respective distributions. It is evident that the differences of the results between the truncated octahedron (TO) model and the truncated cone (TC) model are negligible.

6 Electronic Structure

As demonstrated in Chapter 5 the cluster morphology changes from smaller clusters with more undefined shapes towards larger, faceted clusters with well defined crystal orientation. The electronic structure is expected to be significantly influenced by the morphology. Hence, for a correct interpretation of the experimental spectra the knowledge of geometric details will be crucial. In particular for large, faceted Au clusters on graphite this precondition is well fulfilled and a description in view of bulk properties is expected to be appropriate. The situation becomes more complex for smaller clusters, for which the concept of well defined crystal structures and surfaces breaks down.

Here we give an overview of the experimental results and the analysis on a level as published in Refs. [34,35]. In Chapter 9 the discussion will be refined, joining the results of the different experimental techniques.

6.1 Large Clusters

The occurrence of (111) top facets justifies the treatment of the clusters as small single crystallites. In this view the electronic structure is described by the bulk lattice, with additional consideration of the reduced size. However, it is not clear a priori that the properties of a Au crystal are reflected quantitatively by clusters with dimensions of about $25 \times 25 \times 25$ atoms or lower. Besides the geometry also the cluster-surface interaction is expected to exert an influence on the electronic system. Due to the weak coupling between Au and the HOPG surface this effect is neglected in a first step.

Two overview images of the cluster sample discussed exemplarily in this section (sample D) are given in Fig. 24: the TEM image visualizes the lateral arrangement of the clusters and the STM topograph reveals their morphology in more detail. In Fig. 24b the formation of nearly hexagonal top facets is evident, as discussed in Sec. 5.2. The mean cluster height for this sample is $\langle h \rangle = 2.9$ nm and typical facet areas are about $\Omega \approx 40$ nm². The Au exposure was about $\Gamma_{\text{evap}} = 1.3$ ML, but the uncertainty is rather high compared to the other samples of this work because the evaporator calibration was done for different evaporator parameters. The UPS analysis in Sec. 7.3.3 suggests a larger exposure around $\Gamma_{\text{evap}} \approx 1.8$ ML.

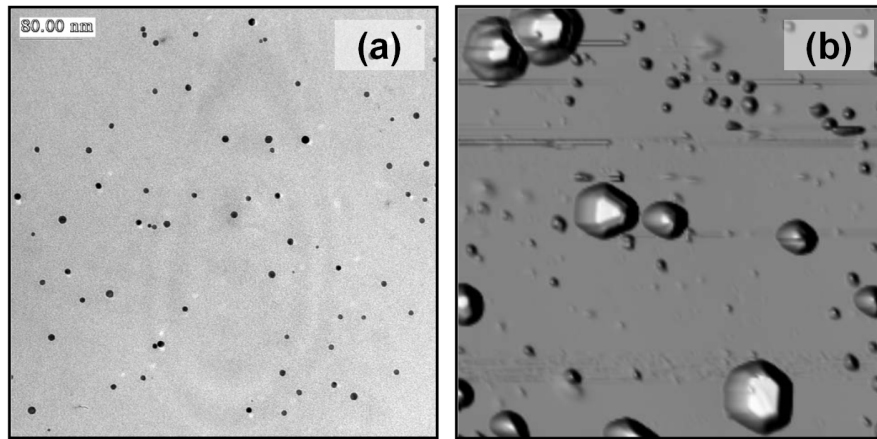


Fig. 24. (a) TEM image ($540 \text{ nm} \times 540 \text{ nm}$) of sample D. (b) 3D display of a STM image ($100 \text{ nm} \times 100 \text{ nm}$) for the same sample. Note the regularly shaped top facets on the larger clusters.

6.1.1 Scanning Tunneling Spectroscopy

First we focus on a cluster with a height of $h = 3.9 \text{ nm}$ and a facet area of $\Omega = 37 \text{ nm}^2$ (Fig. 25). It exhibits a facet shape corresponding to type II of Fig. 21 and the truncated octahedron model results in a cluster size of $N = 1.5 \times 10^4$ atoms.

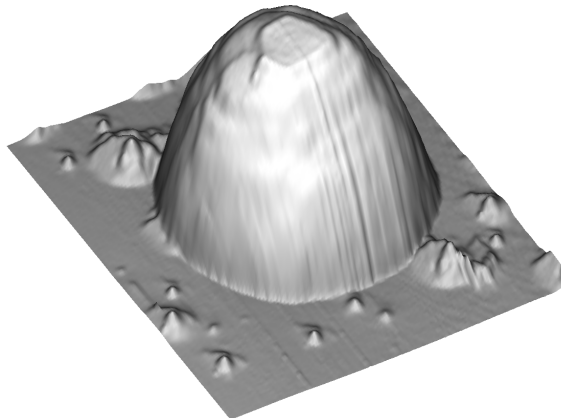


Fig. 25. 3D STM image ($40 \text{ nm} \times 40 \text{ nm}$) of a faceted Au cluster on sample D. The cluster height is $h = 3.9 \text{ nm}$ and the facet area $\Omega = 37 \text{ nm}^2$. The 2D facet silhouette is shown in the inset of Fig. 26.

The flat facets facilitate very stable tunneling conditions on top of the clusters. In Fig. 26 we present dI/dV data taken on the top facet. We compare spectra measured in the center of the cluster facet and spectra averaged over the complete area of the facet. For selected voltages we present dI/dV maps, which show pronounced patterns with nodes

and antinodes, arranged in the approximately hexagonal shape of the facet. Bright (dark) spots in the middle of the dI/dV maps correspond to a higher (lower) dI/dV signal for the spectra taken at the center of the facet as compared to spectra averaged over the whole facet.

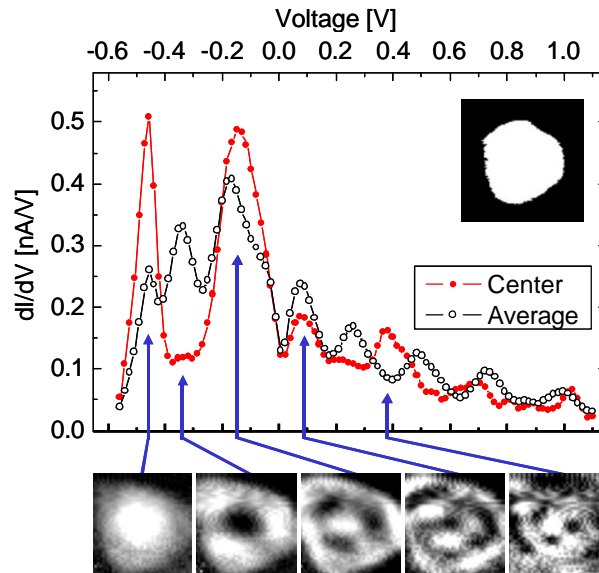


Fig. 26. STS data measured on the (111) top facet of the cluster shown in Fig. 25. Top: dI/dV spectra measured in the center of the facet (full dots) and averaged over the total facet area (open dots), respectively. The facet shape is shown in the inset (10 nm \times 10 nm). Bottom: dI/dV maps (4.5 nm \times 4.5 nm) for five different voltages corresponding to the energy positions in Table 4.

In Fig. 27 the complete data set consisting of 100 dI/dV maps is displayed. The number of nodes and antinodes increases with increasing voltage and even for the largest voltages nodal patterns are observable.

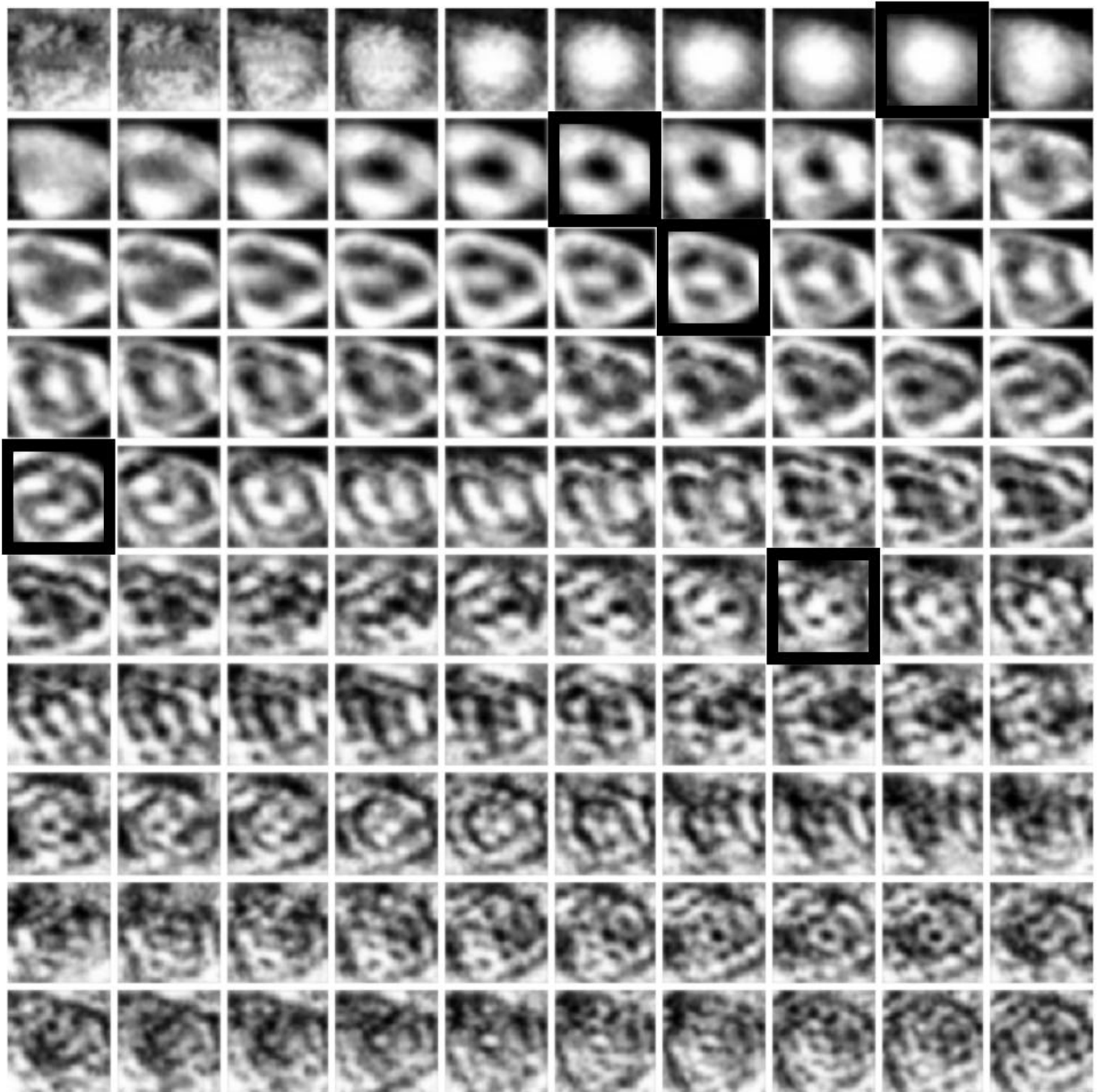


Fig. 27. All 100 dI/dV maps measured on the facet of the cluster in Fig. 25 for the voltage range $V = -0.6 \text{ V} \dots 1.1 \text{ V}$ in steps of 17 mV. The modes shown in Fig. 26 are marked with a black border. All maps are normalized to equal signal amplitude. In order to suppress noise in the images between these modes (where the signal is weak, cf. the animation in Ref. [35]), the images are slightly blurred using a Gaussian convolution.

In Fig. 28a we show another cluster with a height of $h = 2.5$ nm and a facet area of $\Omega = 47$ nm², which results in a cluster size of $N = 1 \times 10^4$ atoms. In the corresponding dI/dV maps (Fig. 28b) again nodal patterns are visible, although the signal-to-noise ratio is lower compared to the maps of Fig. 26. As before, the energy positions of the maps correspond to maxima and minima in the center of the measured dI/dV spectra for this cluster.

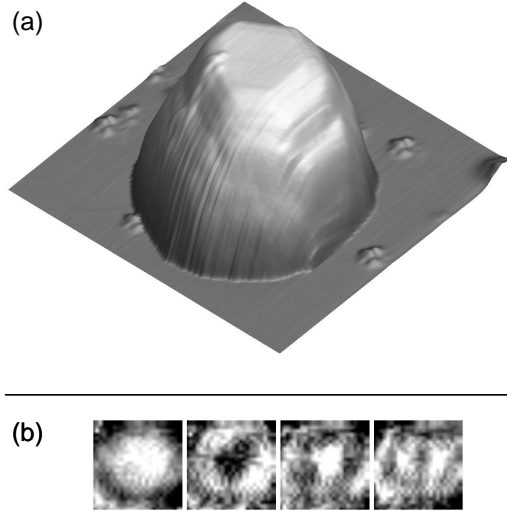


Fig. 28. (a) STM image of a second Au cluster on HOPG (10 nm \times 10 nm). Cluster height: $h = 2.5$ nm. Facet area: $\Omega = 47$ nm². (b) STS maps (5 nm \times 5 nm) analogous to Fig. 26. See Table 4 for the corresponding energetic positions.

The dI/dV maps on the two cluster facets remind of similar patterns which were measured for a two dimensional confinement of the surface state on a Ag(111) surface inside the hexagonal step edges of small 1 ML Ag islands grown on the surface [32,36]. For the silver islands the state with lowest energy $E_1 = -52$ meV without nodes inside the hexagon is close to the onset of the parabolic dispersion of the Ag(111) surface state at $E_0 = -67$ meV. In our data the lowest energy states with $E_1^a = -455$ meV (Fig. 26) respective $E_1^b = -530$ meV (Fig. 28) are close to the corresponding energy for the Au(111) surface which was measured to $E_0 = -487$ meV with UPS [37]. But we want to stress the main difference to previous experiments for metal on metal systems, e.g., in Ref. [36], where the surface state exists in the Ag(111) surface, extending about 12 ML into the bulk [38], and the hexagonal 1 ML islands produce standing wave patterns due to

scattering at the step edges [39-41]. In our experiments the Shockley surface state does not exist in the HOPG substrate but only within the clusters of about 10^4 atoms. This points to an electronic structure of the clusters which is already very close to the bulk, including details like the occurrence of a gap in the surface projected band structure. Due to the small facets the level distance is increased compared to the Ag islands of Ref. [36] and thus most of the states are resolvable with STS without a significant mixing.

In Fig. 29 we show an averaged dI/dV spectrum measured on the cluster of Fig. 26 with $N = 1.5 \times 10^4$ atoms for $V = -1.4 \dots +1.4$ V. Because measurements with $|V| > 0.5$ V induced the danger of tip changes, we measured only single dI/dV spectra and no dI/dV maps for this extended energy range. In addition to the peaks already visible in Fig. 26 one can observe a strong step like structure at about -0.5 eV which is typical for a two dimensional Shockley surface state as described in Chapter 3 (see Fig. 10), and its energy is close to the corresponding step for a Au(111) surface. Similar spectra were obtained for the cluster of Fig. 28 with $N = 1 \times 10^4$ atoms, but not on other, generally smaller clusters without such a pronounced nodal pattern on the facet (see below).

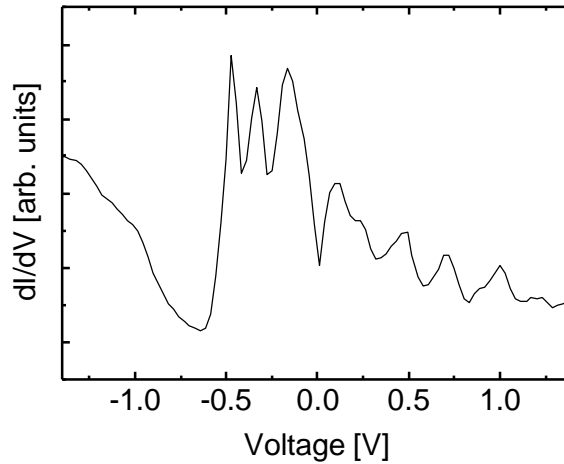


Fig. 29. Average over 14 single dI/dV spectra on different positions spread over the (111) facet for the same cluster as in Fig. 26 ($N = 1.5 \times 10^4$ atoms). STS measured for an extended energy range.

We can describe the experimental data quantitatively using the model of Ref. [36], describing the two dimensional confinement of Shockley surface states, if we allow for a cluster size dependent energy shift of the surface state dispersion (cf. Table 4). The model of Ref. [36] gives

$$E_n^{calc} = E_0 + (I_n / \Omega) \cdot (m_e / m^*) \quad (8)$$

with the values of I_n for a hexagonal confinement. For m^* we use the effective mass $m^* = 0.26 m_e$ of the Au(111) surface state (cf. Sec. 6.1.2). As the only free parameter we adjust the surface state onsets $E_0^a = -528$ meV and $E_0^b = -588$ meV for the two clusters of Fig. 30 so that the energies $E_1^{a,b}$ are identical in experiment and theory, respectively. We obtain an excellent agreement for the energies corresponding to the peaks in the dI/dV spectra and for the measured dI/dV maps with the calculated state densities shown in Ref. [36]. In Table 4 the calculated and measured energy levels are summarized. The respective theoretical and experimental standing wave patterns are displayed in Fig. 30. The energy axis is scaled in such a way that it is independent of the facet area Ω . The different modes are consecutively numbered with regard to their energies E_n with $n \geq 1$.

n	I_n [eV nm ²]	$E_n^{a,calc}$ [meV]	E_n^a [meV]	$E_n^{b,calc}$ [meV]	E_n^b [meV]
1	0.7085	(-455)	-455	(-530)	-530
2	1.795	-342	-336	-441	-420
3	3.213	-195	-	-325	-
4	3.712	-143	-148	-284	-270
5	4.716	-38	-	-202	-
6	5.211	13	-	-161	-
7	5.951	90	92	-101	-105
8	6.945	193	-	-20	-
9	8.666	372	-	121	-
10	8.918	398	382	142	-

Table 4. Measured energy positions $E_n^{a,b}$ for the two clusters (a) (cf. Fig. 25) and (b) (cf. Fig. 28) and theoretical energy levels $E_n^{a,b,calc}$ for a 2D confined electron gas in a hexagonal facet using the theory and prefactors I_n from Ref. [36]. We estimate the error of the experimental energies to ± 15 meV. The accuracy of the theoretical values is determined by the error of $\pm 5\%$ for the facet area. Modes which could not be observed in STS are printed gray.

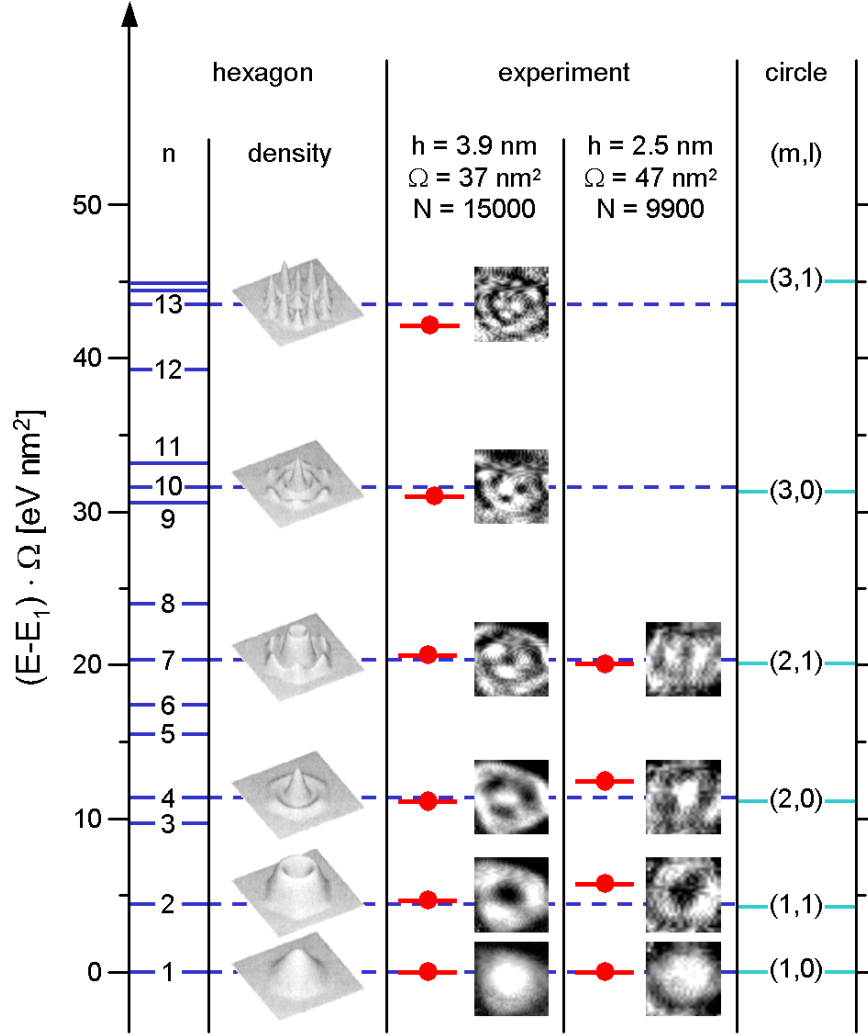


Fig. 30. Left column (“hexagon”): energies for the different quantized modes (numbered with $n = 1 \dots 13$) of a two-dimensional electron gas confined to a hexagonal box calculated using the theory from Ref. [36]. For those modes which are clearly visible in the experiment we display in addition the corresponding calculated state densities as given in Ref. [36]. Middle column (“experiment”): Measured energies and dI/dV maps for the two clusters of Fig. 26 and Fig. 28. Right column (“circle”): energies for the modes with $l = 0$ and $l = 1$ of a two-dimensional electron gas confined to a circular box [42]. The vertical axis is scaled in a way that it is independent of the respective facet area Ω .

In addition the modes are compared to the eigenstates inside a 2D circular box of radius r . The wavefunction is given by $\mathbf{y}_{m,l}(\mathbf{r}, \mathbf{f}) \propto J_l(k_{m,l} \mathbf{r}) e^{i\mathbf{f} \cdot \mathbf{r}}$ with the Bessel function J_l and the wavenumber $k_{m,l} = z_{m,l}/r$. With given radius r the m^{th} zero crossing $z_{m,l}$ of the l^{th} order Bessel function defines the energy $E_{m,l} = \hbar^2 k_{m,l}^2 / (2m^*)$ [42]. This gives $E_{m,l} = E_0 + (\hbar^2 \mathbf{p} / 2) \cdot \mathbf{z}_{m,l}^2 / (\Omega \cdot m^*)$ for the energies of the different modes. As it can be

seen in Fig. 30 the energy positions of the modes which were clearly observed in the experiment (cf. Fig. 26, Fig. 27 and Fig. 28) correspond nicely to the modes with angular momentum $l = 0, 1$; and the corresponding calculated energy positions in the hexagonal confinement differ only by a small amount. Consequently the energy difference between the surface state onset and the lowest energy mode, scaled with the facet area, i.e., $(E_1 - E_0) \cdot \Omega$ is also nearly identical for the hexagon confinement (2.725 eV nm^2) and the circular confinement (2.662 eV nm^2).

In order to fit the absolute energetic position of the first center antinode mode E_1 , the minimum of the parabolic dispersion of the surface state at E_0 has to be shifted to lower energies compared to the onset of the surface state band on a macroscopic gold surface ($E_0^{\text{bulk}} = -487 \text{ meV}$) [37]. This can be related to the shift of the surface state to lower energy for thin metal films due to the interaction with the substrate within the decay length of the surface state [43] or with possible shifts due to film strain [44]. The influence of a field induced Stark shift [45,46] is small here because of the large tunneling resistance of about $R \approx 10^{10} \Omega$. We use the two fix points for $E_0(h)$ given above together with the limiting value $E_0(\infty) = -487 \text{ meV}$ to set up a parameterization of $E_0(h)$ as used in [43]. This results in the formula

$$E_0(h) = -487 \text{ meV} - 491 \text{ meV} \cdot \exp(-h / 1.581 \text{ nm}). \quad (9)$$

Together with the model for the confinement of the two dimensional electron gas to a hexagonal box from Ref. [36] we can now calculate predicted energy positions for all different clusters. The cluster height determines the surface state onset, while the scaling for the peak positions is given by the facet area. To test this, we show in Fig. 31 measured STS curves for six different faceted gold clusters. We have indicated the energy positions predicted for the states with $n = 1$, $n = 4$ (and $n = 2$) in Fig. 31 with solid (and dashed) lines, respectively. For the three largest clusters almost all of the modes can be identified in the dI/dV spectra. The mode at -441 meV for the $N = 9.9 \times 10^3$ cluster is visible as a shoulder, however it can be clearly identified in the corresponding dI/dV maps (cf. Fig. 30). The mode at -9 meV for the $N = 1.1 \times 10^4$ cluster is suppressed by a dip at the Fermi energy (see below).

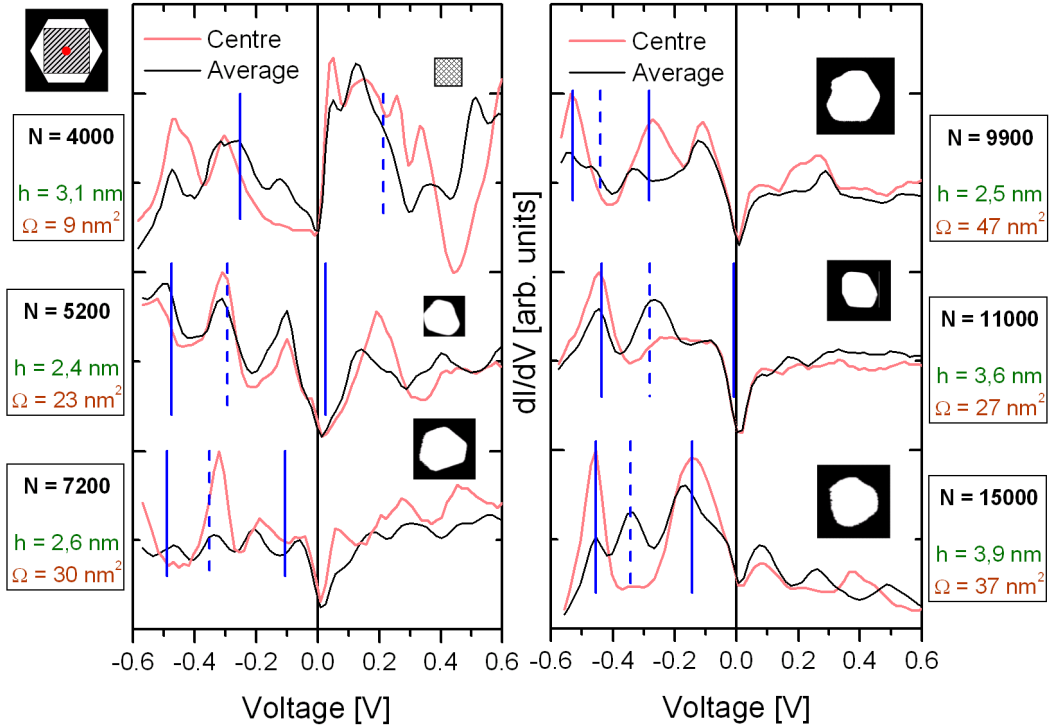


Fig. 31. STS data measured at $T = 5$ K for six individual gold clusters. The height h , the top facet area Ω and the number of atoms N according to the truncated cone model are given for each cluster. In addition the shape of the facet is indicated with STM images (except for the smallest cluster, for which the facet area was estimated using the topographic image measured simultaneously with the dI/dV data). Again two spectra are displayed for each cluster: one measured in the center of the facet and one averaged over the whole facet area. The typical averaging area with respect to the hexagonal facet is indicated in the upper left corner (hatched region). The vertical solid (dashed) lines indicate the energy positions predicted for the states with $n = 1, 4$ ($n = 2$) for the model of a hexagonal box discussed in the context of Fig. 30.

The agreement for the three smallest clusters is much worse. For the clusters with $N = 7.2 \times 10^3$ and $N = 5.2 \times 10^3$ one can observe a peak near the energy predicted for the E_2 mode, but the peaks for E_1 are not visible, and no agreement at all is obtained for the cluster with $N = 4.0 \times 10^3$.

For all measured clusters in Fig. 31 we observe a minimum in the dI/dV curves which is located at $V = 0$, i.e. at the Fermi energy. It can be excluded that this feature is caused by an artifact within the lock-in detection because we see it identically in the $I(V)$ curves after numerical differentiation, albeit with a smaller signal-to-noise ratio. One would not expect the Fermi energy to be special, neither for surface nor for volume states, if the

spectra simply represent the density for the confined and quantized states. Therefore this minimum indicates that the spectra cannot be interpreted solely as given by the local density of states. Effects like the charge transport in the tip/cluster/surface system (cf. discussion in Sec. 6.2), perhaps in combination with the vanishing density of states at the Fermi energy for the HOPG substrate, have to be considered additionally.

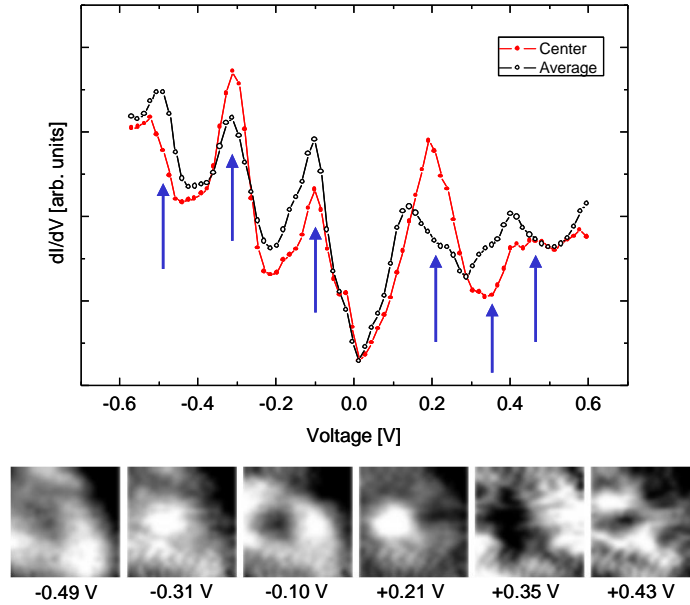


Fig. 32. dI/dV spectra (dots: center of facet; circles: average over facet area) and dI/dV maps of a smaller faceted cluster with $h = 2.4$ nm, $\Omega = 23$ nm² and $N = 5.2 \times 10^3$ atoms (cf. Fig. 31). The center of the facet corresponds to the bright spot in the map for $V = +0.21$ V .

In Fig. 32 we show dI/dV spectra and maps for the cluster with $N = 5.2 \times 10^3$ atoms. An alternation between a maximum and a minimum in the center of the facet area is also present in this case, and the nodal pattern is still visible, but much less pronounced than in the case of the larger clusters discussed in the context of Fig. 26 and Fig. 28. This corresponds to the smaller differences between the dI/dV spectra measured in the center or taken as the average over the whole facet area. The description using a confined Shockley surface state does not fit to this case, as it gets obvious for the peak at -0.31 eV which is predicted to be a mode with $n = 2$, i.e. with a node in the center of the dI/dV map, in contrast to the measured antinode in the center.

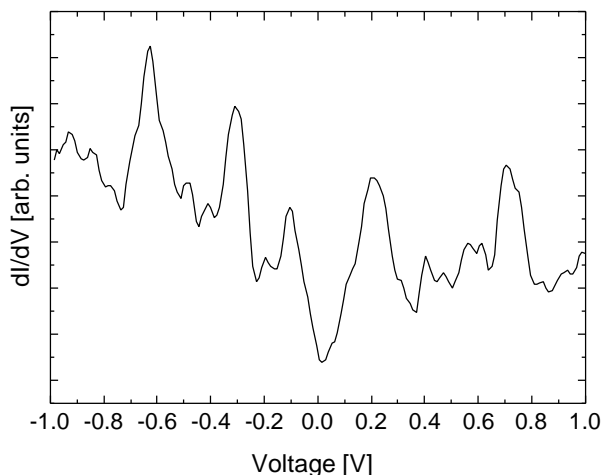


Fig. 33. Average over several single dI/dV spectra measured on the top facet of the cluster with $N = 5.2 \times 10^3$ atoms for an extended energy range. For this cluster no characteristic step structure is identifiable, in contrast to the spectrum of Fig. 29.

The difference to the larger clusters is underlined by the dI/dV spectra measured for an extended energy range ($V = -1 \dots +1$ V) shown in Fig. 33. In contrast to the spectrum in Fig. 29, on the cluster with $N = 5.2 \times 10^3$ atoms we do not observe such a pronounced step-like onset of the peaks in the dI/dV spectra, near the minimum of the surface state band on a macroscopic gold surface. In this context it is remarkable that for the cluster with $N = 1.5 \times 10^4$ atoms not only the energetic positions and the patterns of the different modes fit to the theory for a confined surface state (cf. Fig. 30). In addition also the shape of the dI/dV spectra measured in the center and on the whole facet (cf. Fig. 26) is in very good agreement with measured and calculated spectra for a slightly distorted hexagonal Ag(111) island as shown in Fig. 8 of Ref. [36] (of course with a different absolute energy scale). In particular this is valid for the enhancement of the first mode at E_1 and the almost complete suppression of the second mode at E_2 in the center of the facet. Some remnant of this pattern is visible in Fig. 31 also for the clusters with $N = 1.1 \times 10^4$ and $N = 9.9 \times 10^3$ atoms but for smaller sizes the spectra are different as discussed, e.g., in the context of Fig. 32 above. We expect that there exists a minimum facet size or a minimum cluster height, below which the surface state disappears.

6.1.2 Photoelectron Spectroscopy

With UPS it is not possible to address single clusters as with STS, but given the typical focal area of the analyzer (10^7 nm^2) and a cluster density of $r_c \approx 10^3 \text{ nm}^{-2}$ we always average over about 10^{10} clusters for our samples. So different from scanning tunneling experiments, where the size distribution allows to gather information about a broader range of cluster sizes and morphologies with a single sample preparation, in the case of UPS different cluster sizes lead to a loss of information, mainly due to inhomogeneous broadening.

The d-band spectra of large, faceted Au clusters (Fig. 20) are already very close to the bulk Au(111) spectra. This indicates that the bulk like treatment of these clusters is justified. Above a critical cluster size the d-band structure does not change significantly, hence the size distribution does not lead to noticeable spectral broadening. Nevertheless, other influences on the UPS curves as, e.g., the dynamic final state effect (cf. Chapter 8) have to be considered, which also may include a size dependence.

The Shockley surface state on the cluster facets described in the previous section should also be visible in UPS spectra near the Fermi edge. Angular resolved spectra for a Au(111) film on mica (thickness $\approx 10^2 \text{ nm}$) with an angular resolution of $\pm 1^\circ$ are shown in Fig. 34. In normal emission, i.e., at the Γ point of the surface Brillouin zone, the surface state peak is located about 430 meV below the Fermi level. With increasing emission angle it shifts towards higher energies until it crosses the Fermi level and becomes unoccupied. The parabolic shift reflects the free electron like nature of the surface state. We performed a detailed analysis, taking into account the finite angular and energetic resolution of the setup [20]. The semi-analytical model and data processing steps are summarized in Appendix 11.1. The fit of the model to the experimental data reveals the surface state onset $E_0^{bulk} = (-445 \pm 5) \text{ meV}$ and the effective mass $m^* / m_e \approx 0.25$. ARUPS measurements of a Au(111) single crystal with extremely high resolution ($\Delta E \approx 3.5 \text{ meV FWHM}$; $\mathbf{s}_a \approx 0.15^\circ$) result in $E_0^{bulk} = -487 \text{ meV}$ and $m^* / m_e = 0.26$ [37]. The discrepancy of the onset energies is probably caused by residual stress of the Au film of mica, forming μm sized crystallites with large cloughs in between [20]. More recently, a value of $E_0^{bulk} = (-479 \pm 2) \text{ meV}$ has been reported [47], which reduces the discrepancy to $\approx 30 \text{ meV}$. The splitting of the surface state due to the spin-orbit interaction reported in Ref. [37] is only visible for angular resolutions significantly better than $\pm 1^\circ$.

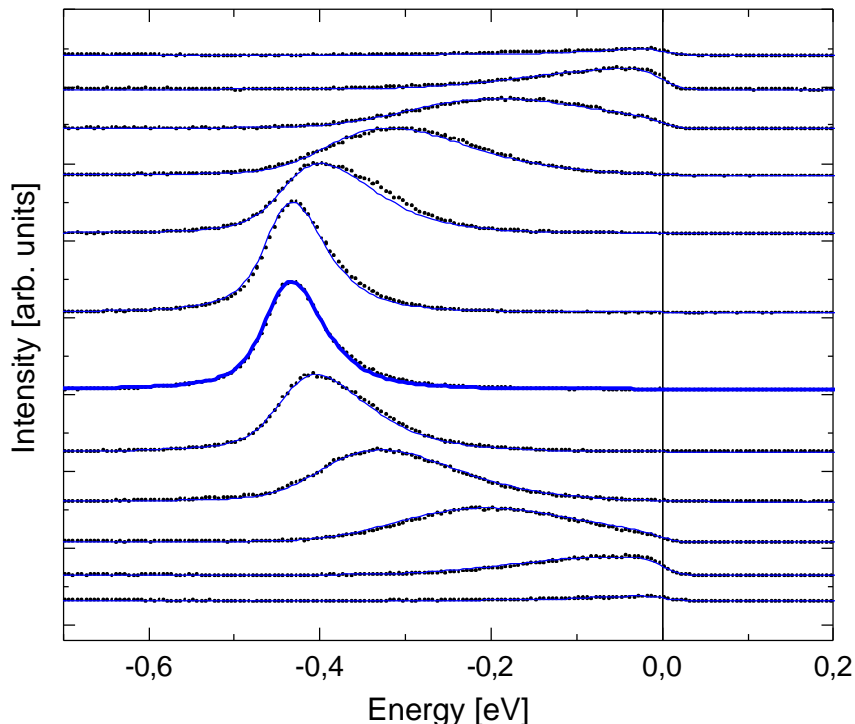


Fig. 34. Angle resolved photoelectron spectra (dotted curves) of a Au(111) film (thickness $\approx 10^2$ nm) grown on mica after background subtraction (see Appendix 11.1 for details). The emission angle is varied from about -5° (bottom) to $+6^\circ$ (top) in steps of 1° . The curves are shifted vertically for clarity. The sample temperature was $T = 50$ K and the photon energy $\hbar\omega = 21.2$ eV. The blue solid lines represent the fit for a parabolic dispersion including a model for the finite experimental angular and energetic resolution (cf. Appendix 11.1). The agreement between experiment and calculation is nearly perfect. The calculated spectrum closest to normal emission is plotted with a thick line.

The spectra in Fig. 35 were measured for the cluster sample discussed in Sec. 6.1.1. They also show, on top of the Fermi level onset an extra peak at an energy of about -0.5 eV for normal electron emission, i.e., $k_{\parallel} = 0$, which disappears for angles $\pm 3^\circ$ off normal emission. In addition a significant broadening occurs, together with an asymmetric behavior with regard to the emission angle. These effects are discussed in more detail in Chapter 9. The peak position in normal emission is similar to the bulk Au(111) surface, except for a shift of about 0.1 eV to lower energies for the cluster sample. As demonstrated in Sec. 6.1.1, the surface-state onset is shifted to lower energies for smaller cluster heights.

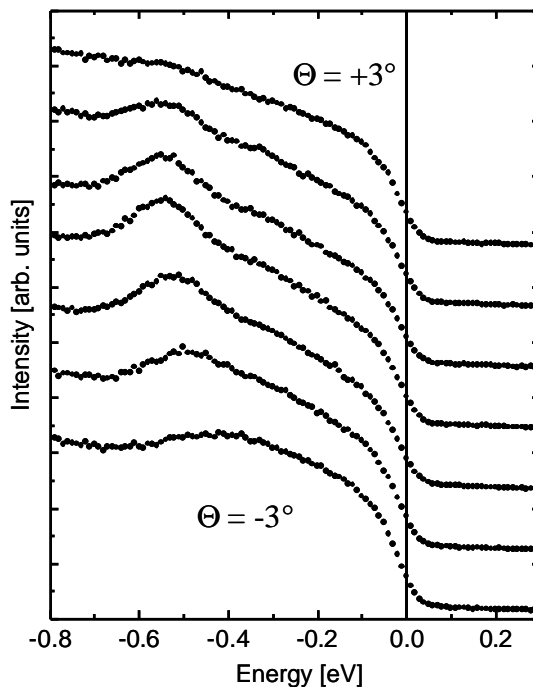


Fig. 35. Angle resolved photoelectron spectra of cluster sample D, measured at $T = 50$ K. The emission angle was increased in steps of 1° from about -3° to 3° . Instead of the continuous dispersion of the surface state (cf. Fig. 34), its peak intensity essentially gets broader and vanishes at higher emission angles. The shape of the Fermi edge is characteristic for Au clusters on graphite. It is discussed in detail in Chapter 8.

The broad structure in the UPS spectra of Fig. 35 is supposed to be given by the average over the first confined state E_1 for different clusters. The disappearance of the peak structure for off-normal emission can be explained as a remnant of the two dimensional dispersion for a surface state. Similar effects occur at vicinal Ag(111) [48] and Au(111) [49] surfaces for the direction perpendicular to the steps. For E_n with $n > 1$ corresponding peak structures are not visible in Fig. 35 due to the averaging over a broad range of facet sizes and cluster heights and additional effects in the photoemission process. These influences are discussed in detail in Chapter 9. Due to the broad features and the weak dispersion of the cluster spectra the finite angular resolution of the analyzer (cf. Appendix 11.1) does not result in a significant effect on the line shapes.

6.2 Small Clusters

The topographic imaging of smaller, non faceted clusters is in general easier than for the large clusters discussed in the last section. The probability for tip induced cluster displacement is significantly reduced, allowing larger image sizes and therefore more efficient measurements. However, for scanning tunneling spectroscopy on single clusters the situation is different. While the flat top facets of large clusters enable stable tunneling conditions for several hours, in absence of a facet residual lateral forces are hardly avoidable. In particular during the spectroscopy process this can lead to a displacement of the cluster. For this reason it is crucial to locate the tip exactly on top of the cluster center, i.e. the highest position in the topograph (cf. Sec. 2.1). Unfortunately this is a challenging task due to drifts induced thermally or by the STM piezo crystals [50]. Fig. 36 illustrates the typical experimental procedure we used for STS measurements on small Au clusters on HOPG.

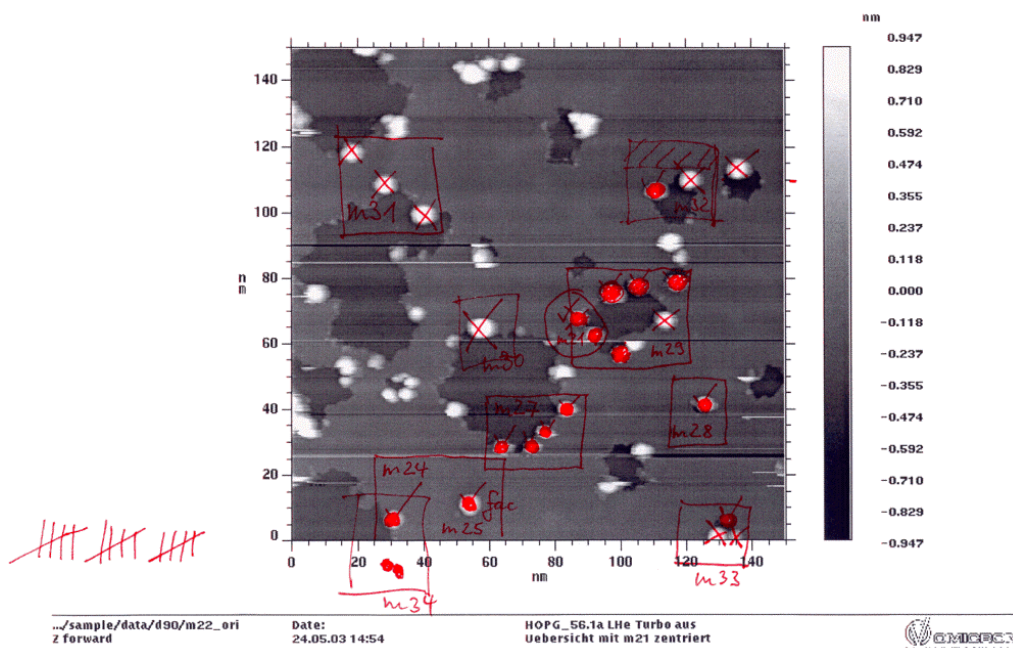


Fig. 36. Laboratory work sheet illustrating the experimental procedure for STS on top of single Au clusters on HOPG (sample A). Starting from the overview image (same as Fig. 12) we zoomed into smaller frames (squares). Crosses mark clusters which were removed from their sites during spectroscopy. Successfully measured clusters are indicated by full circles and check marks (here 15 clusters). Image size: 150 nm \times 150 nm .

Earlier STS studies for silver clusters on HOPG exhibited prominent structures in the dI/dV curves [29]. Although a tendency to lower peak distances for larger clusters is

observable, a systematic size dependence of the peak positions is not evident from these data. In the corresponding study of small gold clusters presented here we focused on systematic trends in a large number of measurements performed on individual clusters.

In Fig. 37 the averaged dI/dV curves for 61 different clusters are summarized. They are arranged by the cluster height and normalized to the same amplitude. For each Au cluster we took about 10 dI/dV curves and only if they were identical within the signal-to-noise ratio they were accepted and averaged. At first glance the richly structured spectra seem to show hardly any systematic behavior. However, for certain height ranges the curves exhibit striking similarities or systematic trends (thick curves). The red curves indicated with “m24” and “m34” illustrate the reproducibility of the spectra. The same cluster ($h = 1.6$ nm) was measured twice, some hours apart, with several tip preparation steps in between. The spectra “m24” and “m34” belong to the clusters marked in the lower left corner of Fig. 36. The two dI/dV curves are nearly identical, except for the sharp peak around -1 V which has shifted to lower energies. This fits well into a more general observation: we could distinguish between two different types of structures. On the one hand we observe quite sharp peaks, which are dependent on the actual tip condition as well as on the exact lateral position on top of the cluster. The position dependent shifts are typically of the order of a few 10 meV. The other, mostly broader structures seem to represent more intrinsic properties of the cluster/surface system.

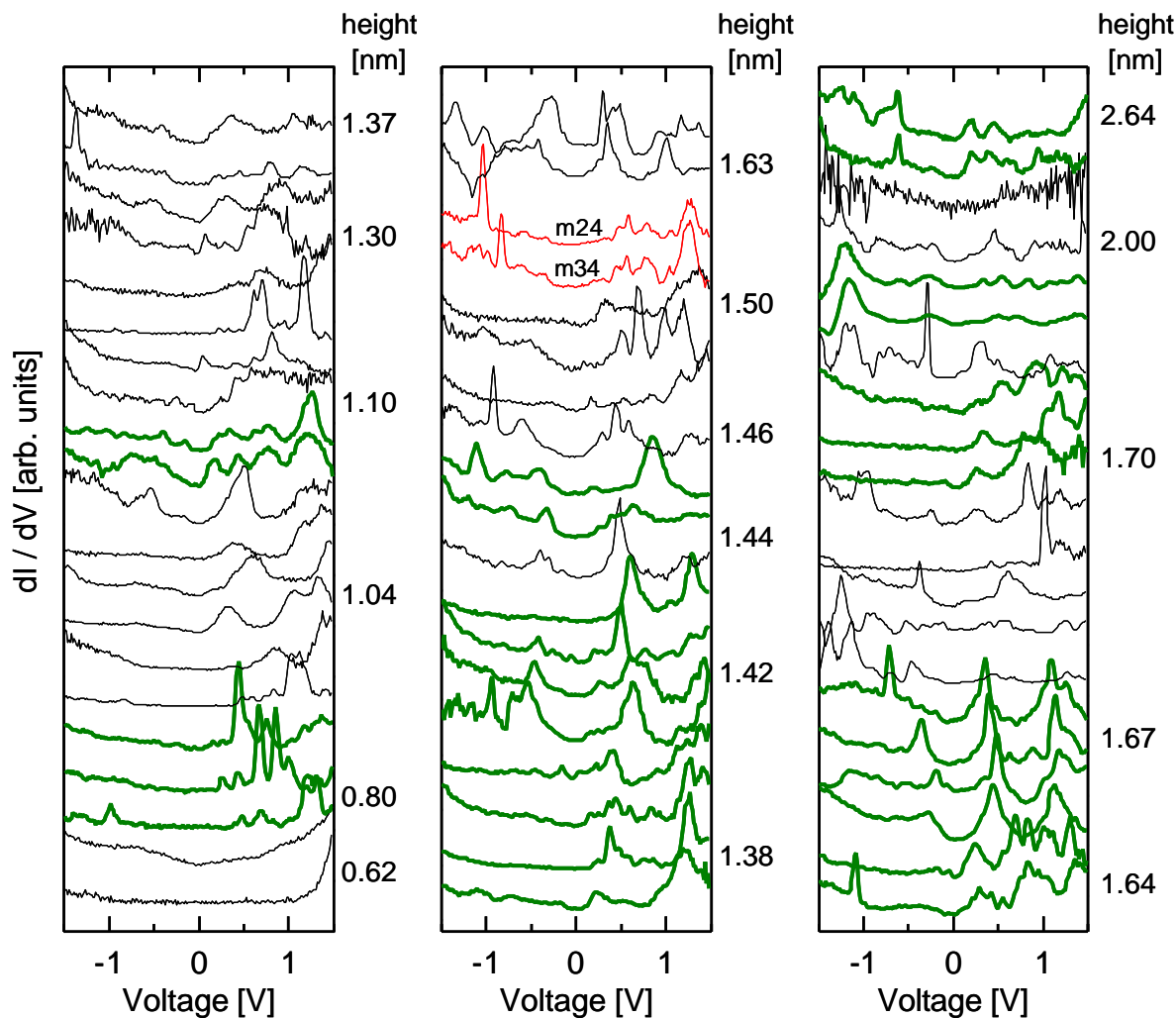


Fig. 37. Averaged dI/dV curves of 61 different small, non faceted Au clusters on HOPG. The spectra have been taken in arbitrary order and then arranged in the plot by the corresponding cluster height. Hence the cluster heights are not equidistant. Systematic trends are indicated by thick green lines. The red spectra marked with “m24” and “m34” are measured on the same cluster (see text).

The theoretical description of the observed structures is extremely difficult. We expect three main effects which could in principle contribute to the dI/dV curves. First, in the limit of a very few atoms one would expect a discrete DOS arising from the molecular electronic levels. Calculations based on a parameterized tight binding model for free Cu-clusters indicate a transition to a continuous DOS at about 100 atoms [51]. The average number of atoms for the clusters of sample A is about $N = 280$ (cf. Table 2), thus the observation of discrete molecular states may appear to be improbable. In the limit of

non-degenerated (except for the spin degeneracy) electron states the mean energy spacing near the Fermi edge would be [29]

$$dE = 2\mathbf{p}^2 \hbar^2 / (mk_F V), \quad (10)$$

where m is the electron mass, k_F is the Fermi wave vector, and V is the cluster volume.

In the case of highly symmetric particles, however, the multiple degeneracy increases the mean level distance. In analogy to the electronic shell structure of alkali clusters [2,52] peaks in the DOS correspond to shell closings at so-called “magic” cluster sizes. For a spherical metal particle the electronic structure can be calculated using self-consistent jellium techniques [53] or semiclassical approaches [54] developed originally by Gutzwiller [55] and Balian and Bloch [56]. In a simple periodic orbit approach the mean length $\langle L \rangle$ of classical orbits determines the main shell oscillation periodicity. For a spherical cluster of the radius R one gets $\langle L \rangle = 5.42 R$ [53], which results in an energy spacing of [29]

$$\Delta E = \hbar^2 k_F \mathbf{p} / (2.71 m R). \quad (11)$$

These main shell closings for high symmetry particles give an upper limit for the observed peak distances. In Fig. 38 the two limits for Au clusters according to Eqs. 10 and 11 with $k_F = 1.2 \text{ \AA}^{-1}$ are shown together with the area of measured peak distances estimated from Fig. 37. Since the experimental energy spacing remains within the two limits, the interpretation in terms of discrete, partly degenerated electron states is plausible. This is supported by the striking similarities and systematic trends of spectral features in Fig. 37 (green curves) for similar cluster heights, particularly around $h \approx 1.1 \text{ nm}$, $h \approx 1.4 \text{ nm}$, and $h \approx 1.67 \text{ nm}$, respectively.

A direct quantitative comparison between theory and experiment is not feasible due to the imperfect knowledge of the cluster size and morphology. Even if we knew the exact position of every Au atom the calculation of the electronic structure would be extremely complex due to the large number of atoms and the specific properties of Au, as e.g. large relativistic effects [1,57]. In a bulk-like approach the application of the semiclassical methods mentioned above would require the analysis of periodic orbits taking into account the anisotropic electron band structure of gold and potentially the formation of facets as discussed in Ref. [58].

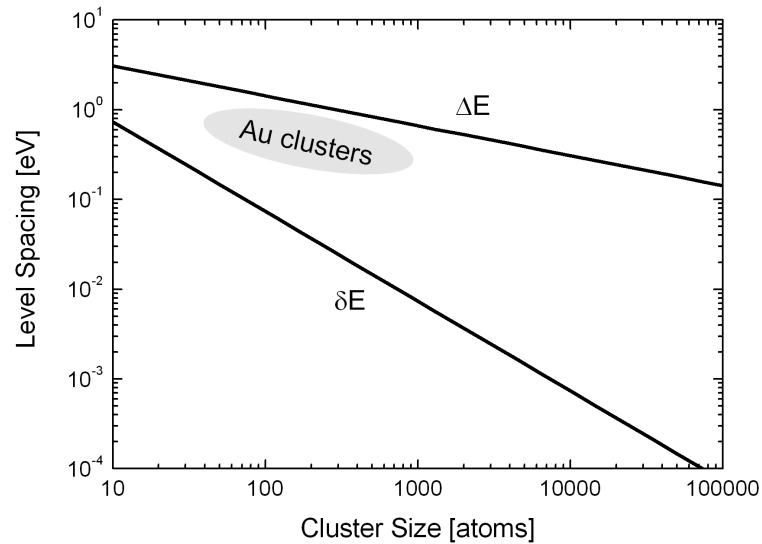


Fig. 38. Upper (ΔE) and lower (δE) limit of the energy spacing close to the Fermi level according to Eqs. 10 and 11. The range of measured peak distances in the STS curves (see Fig. 37) are indicated by an oval area. Adapted from Ref. [29].

The third effect is connected to the experimental setup. The tunneling current is not solely dependent on the electronic structure of the cluster, but the physics of the entire tip/cluster/surface system has to be taken into account. If the cluster-substrate interaction is low the system corresponds to a double-barrier tunnel junction (DBTJ) [59]. It consists of a metal island coupled to two electrodes via tunneling junctions. The equivalent circuit diagram and the corresponding setup during our experiment are shown in Fig. 39.

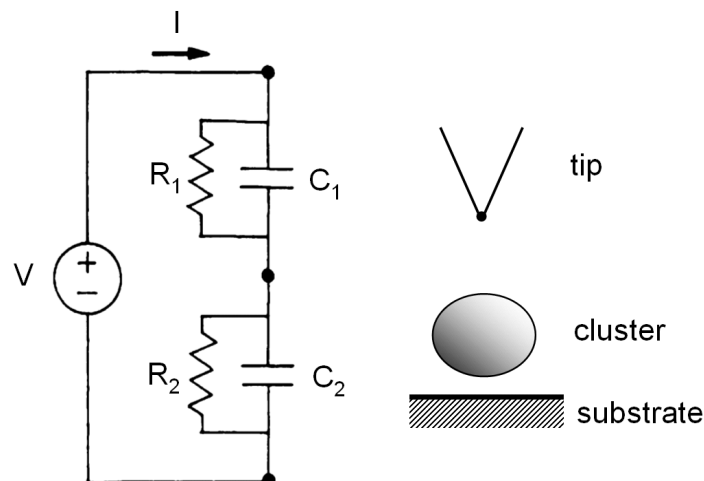


Fig. 39. Circuit diagram of a double barrier tunnel junction (left). In the STM setup (right) R_1 and C_1 correspond to the tunneling path between tip and cluster, whereas the electron transport from the cluster into the substrate is determined by R_2 and C_2 .

The expected $I-V$ curves can be calculated with rate equations [60] which can be easily solved numerically. Their detailed shape depends strongly on the choice of the capacitances $C_{1,2}$ and the resistances $R_{1,2}$, but typical curves exhibit step-like features as shown in Fig. 40. These steps are caused by single electron charging of the island and they would lead to peaks in the differential conductivity dI/dV . For certain ranges of the parameters the $I-V$ curves consist essentially of a sum of equally spaced and thermally broadened steps. In the limit $R_1 \gg R_2$ and $C_1 \geq C_2$ the step distance is given by $\Delta V = e/C_1$. The energetic positions of the steps and the width of the “Coulomb blockade” (i.e. the region with zero current at low voltages) is dependent on the offset charge Q_0 on the cluster which can be induced by work-function differences [60]. From typical tunneling distances and cluster sizes we estimate the capacitance between cluster and tip to be about $C_1 \approx 10^{-19}$ which would lead to $\Delta V \approx 1$ V. This is significantly more than the observed peak distances in the dI/dV spectra in Fig. 37. But as pointed out above, we can distinguish between two different kinds of STS peaks, and possibly the sharp species is connected to the influence of the DBTJ. This is in agreement with the fact that these sharp peaks depend on the lateral tip position [29] as well as on the tip condition (see Fig. 37, dotted red curves). However, a quantitative analysis would require a systematical investigation of the Coulomb effect, e.g., by varying the tip-cluster distance and hence the parameters R_1 and C_1 . This is very difficult because it would require stable STS measurements on the same cluster for a broad range of different tunneling parameters without changing the tip shape.

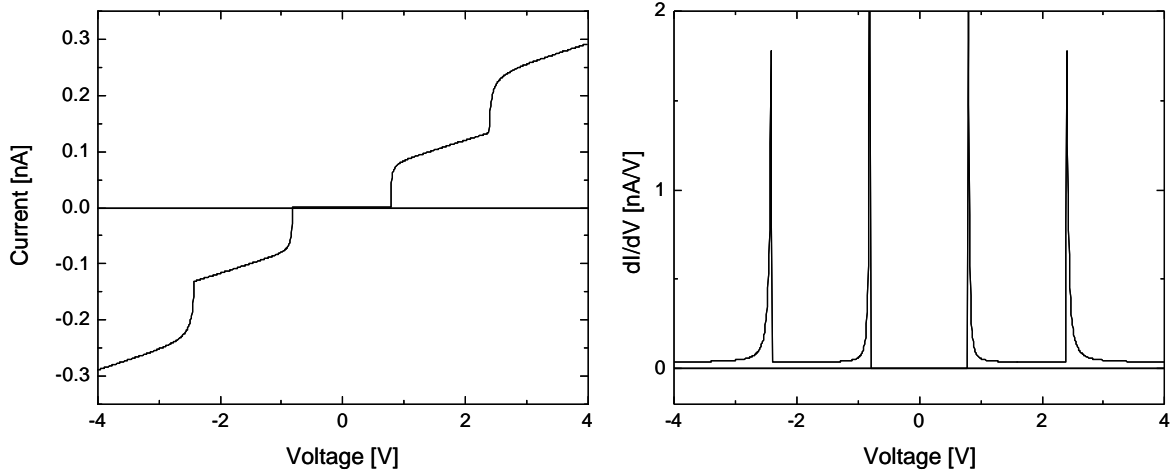


Fig. 40. $I-V$ (left) and dI/dV (right) curves calculated numerically by solving the rate equations for a DBTJ. The parameters were $R_1 = 10^{10} \Omega$, $R_2 = 10^8 \Omega$, $C_1 = 10^{-19} \text{ F}$, $C_2 = 5 \cdot 10^{-20} \text{ F}$, and $Q_0 = 0$ with the notation of Ref. [60]. Finite values for the offset charge Q_0 result in a horizontal shift of the steps and a corresponding change of the peak positions in the dI/dV curves. Also the width of the “Coulomb blockade” with $I = 0$ around $U = 0$ is dependent on Q_0 .

In this section we have discussed different mechanisms leading to a peak structure in the differential conductivity for small clusters. However, the observed features in the dI/dV spectra of small Au clusters on HOPG cannot be finally explained on a quantitative level. Due to the undefined morphology compared to large, faceted Au clusters (cf. Sec. 5.2) the systematic investigation of the electronic structure is difficult. A promising approach is the utilization of an alternative preparation method, the controlled deposition of size-selected clusters under soft-landing conditions [61,62]. The well defined and tunable cluster sizes would reduce the morphology uncertainty and thus facilitate more targeted measurements. In addition the direct comparison to the electronic properties of free Au clusters is possible. Such experiments are planned subsequent to this work as a topic of future projects.

7 Growth Process

In Chapter 5 we divided the discussion of the cluster morphology into two parts: for small, non-faceted clusters we used a truncated sphere model, whereas for large, faceted clusters the truncated octahedron model was favored. In this section the growth process will be discussed based on combined STM and UPS results, starting from a few adatoms, undergoing the mentioned morphology transitions, until approaching crystal equilibrium shapes

7.1 Nucleation Centers

During the deposition the metal atoms adsorb on the substrate and form a two dimensional phase of diffusing particles [63] until they either condense to clusters or finally desorb again. The key role of the nanometer sized pits on the HOPG substrate (cf. Chapter 4) is to provide appropriate condensation centers which capture the metal atoms and hence serve as starting locations for subsequent nucleation processes. In the Au cluster STM images we observe clusters at the edge of the pits as well as at monoatomic HOPG steps. Thus graphite sites with low coordination number are apparently preferred for the cluster growth. Once a critical nucleus has developed, the probability of the formation of further nuclei in its vicinity is much lower than the capture of additional atoms, resulting in a growth of the existing cluster. This explains the rather low width of the measured cluster height distribution and the absence of an accumulation of small clusters (cf. Fig. 14 and Fig. 17). In addition the cluster density r_c , i.e. the number of clusters per area remains essentially constant during the growth, even if the pits are large enough to allow the formation of several clusters at their edges. The constant cluster density can be checked by STM measurements of the same substrate after each evaporation step. Fig. 41 shows an overview image of sample B and sample C. The preparation parameters of these samples were presented in the sections 5.1 and 5.2, respectively. For the right image the gap voltage was set to 10 V in order to increase the tip-sample distance for a lower probability of tip induced cluster movement. According to Fig. 4 the cluster heights are largely underestimated, but this is of minor interest in this context. The number of clusters has not changed drastically, though the gold exposure Γ_{evap} of sample C was increased by a factor

of 4 with respect to sample B. The ratio of the actual Au coverages Γ_{sample} on the samples is even larger (cf. Sec. 7.3.3).

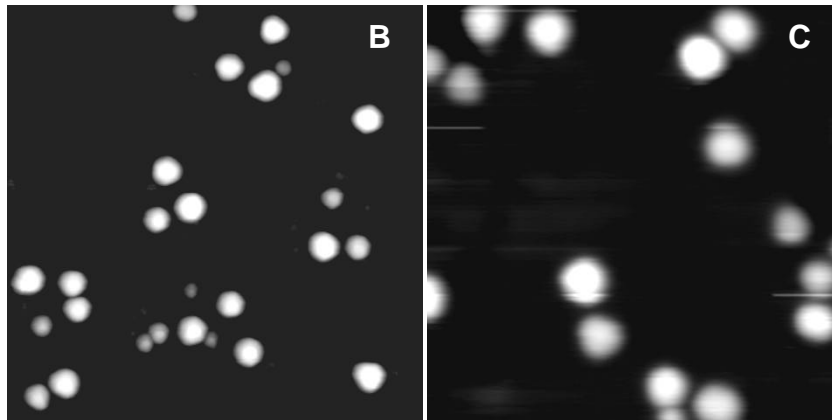


Fig. 41. Gray scale STM images ($100 \text{ nm} \times 100 \text{ nm}$) of sample B (left) and sample C (right). The number of clusters per area is hardly dependent on the Au exposure.

The probability for a gold atom to be captured by an existing nucleus is not equal to 1. This means that the condensation coefficient $\mathbf{b} = \Gamma_{\text{sample}} / \Gamma_{\text{evap}}$ is lower than 1, as already estimated from the STM images (cf. Chapter 5). If the mean adatom diffusion length \mathbf{l}_{diff} before desorption (see Sec. 7.4) is much larger than the typical cluster-cluster distance, the condensation coefficient will approach 1. At $T = 350^\circ\text{C}$ the diffusion length is about $\mathbf{l}_{\text{diff}} \approx 6 \text{ nm}$ [64], which is in our case lower than the most cluster distances (see, e.g., Fig. 18). As a consequence, a low value of \mathbf{b} corresponds to a small influence of neighboring clusters on the growth. This is confirmed by the fact that no significant correlation could be found between the local cluster density and the corresponding sizes: if the diffusion length was large compared to the cluster distances, clusters close to each other would share the diffusing atoms in the same area, which would lead to smaller sizes than for areas with a low cluster density. Hence, for the further investigation of the growth process it is sufficient to reduce the problem to the growth of a single cluster, neglecting the influence of the surroundings (approximation of independent clusters).

7.2 Cluster Location

In this section we will analyze in a first step the exact lateral location of the Au clusters with respect to the nanopit edges. In other words, we would like to distinguish between the growth on the bottom of the pit and on the top plane of the HOPG substrate. Usual STM images as e.g. Fig. 12 are not well suited for this problem because of the unknown influence of the tip on the cluster morphology (cf. Sec. 2.1). Assuming a symmetric lateral morphology, the highest point of the imaged cluster corresponds to its center, independent of the tip shape. But the exact location of the pit edge below the cluster is not known and due to the curved pit shape with kinks and edges a simple interpolation of the pit through the cluster is not possible.

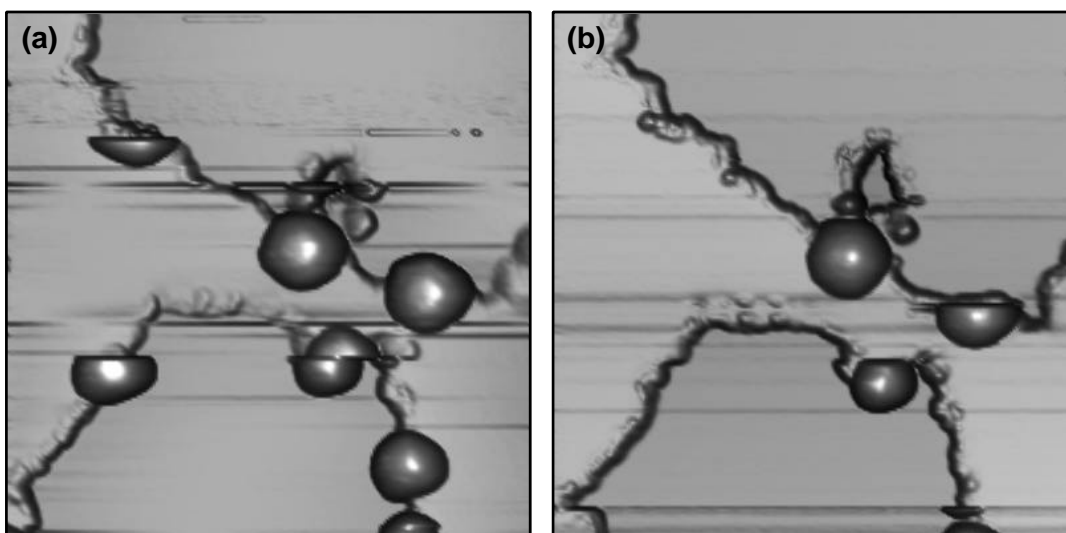


Fig. 42. Pseudo 3D STM images of sample A before (a) and after (b) the tip induced displacement of three clusters. Two of them (at the edge of the lower pit) could be imaged sufficiently to allow the determination of their lateral positions. Image size: $42\text{ nm} \times 42\text{ nm}$.

To overcome this problem we make use of an otherwise unwanted effect, the displacement of single clusters from their sites induced by lateral tip-cluster forces. In Fig. 42 two STM images of the same sample area are shown before (a) and after (b) the tip induced cluster movement. The two lower clusters in Fig. 42a are missing in the second image (b). Fitting the pit contour of image (b) to the corresponding visible part of (a) the lateral cluster location can be reconstructed. The result is shown in Fig. 43, together with the expected true cluster diameter according to $d/h = 1.4$ (cf. Sec. 5.1). The centers of the clusters are located very close to the pit contour, i.e., each cluster is grown partly on the

upper and partly on the lower graphite plane. We have verified this finding for 15 other clusters which were displaced between two STM scans [24].

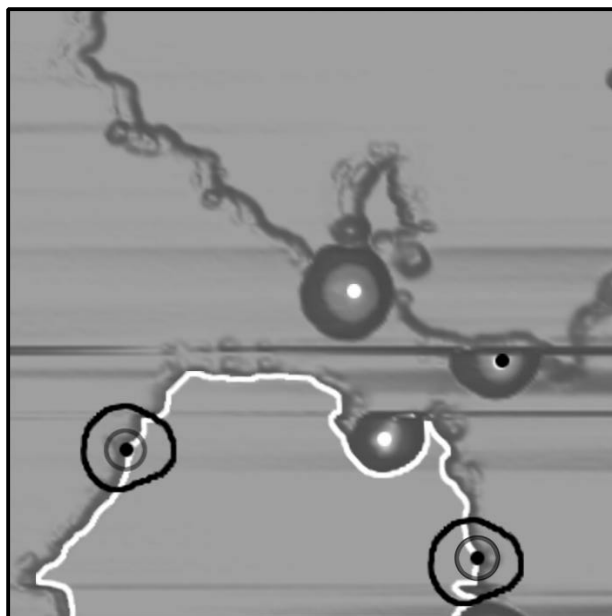


Fig. 43. Reconstructed cluster locations with respect to the pit edge. The white pit contour and the white marked locations of the three upper fixed clusters are deduced from the STM image in Fig. 42b. The cluster locations indicated by black dots are obtained by fitting the pit contour of Fig. 42a to the white line. The outer cluster contours (thick black lines) contain the tip induced broadening, whereas the smaller circles around the black dots represent the expected actual cluster shape according to the truncated sphere model (cf. Sec. 5.1). The white line was generated by an automatic contrast enhancement procedure resulting in the artifact of a continued line around the cluster at the top pit edge. Image size: $42\text{ nm} \times 42\text{ nm}$.

The cluster location is probably not determined predominantly by the growth dynamics: in this case we would expect that clusters at small pits show the tendency to grow in the direction off the center because the larger fraction of the Au atoms approaches from the upper plane during the evaporation. In the STM images we could not find evidence for this effect. Instead we assume that the location as well as the morphology will be basically given by the minimization of the overall energy. This is consistent with the formation of well defined facets for larger clusters (cf. Sec. 5.2) and means that the position at the pit edge is one aspect of the equilibrium state. For Au clusters with a diameter in the micrometer range it is well known that the time which is necessary to reach the equilibrium shape is of the order of a few days, even if the temperature is chosen to be just below the melting point [65]. During the preparation of our gold clusters the temperature of

$T = 350\text{ }^{\circ}\text{C}$ is kept for only a few minutes before cooling down the sample. In order to check if this is enough for clusters with a diameter of a few nanometers we estimate the order of magnitude of the relaxation time for the equilibrium shape using a formula which is derived in Ref. [66] and used in Ref. [65] for Au crystals with micrometer dimensions:

$$t = \frac{r^4 k T \mathbf{s}}{24 \mathbf{g} D_s \mathbf{n}^2}, \quad (12)$$

where r is the cluster radius, k is Boltzmann's constant, \mathbf{g} is the surface energy ($\approx 1\text{ J/m}^2$ [67]), D_s is the surface diffusivity ($\approx 10^{-15}\text{ m}^2/\text{s}$ at $350\text{ }^{\circ}\text{C}$ [68]), \mathbf{n} is the atomic volume ($1.7 \cdot 10^{-29}\text{ m}^3$ for Au), and $1/\mathbf{s}$ is the number of atoms per surface area ($7 \cdot 10^{-20}\text{ m}^2$). The formula is based on the assumption that the shape is in first order described by a sphere and that surface diffusion is the dominating mechanism for morphology changes. Depending on the cluster size, we get relaxation times between $t \approx 10^{-4}\text{ s}$ (for $r = 1\text{ nm}$) and $t \approx 10^{-2}\text{ s}$ (for $r = 4\text{ nm}$). This means that the preparation time is several orders of magnitude longer than the relaxation time, therefore we expect essentially the formation of equilibrium shapes of the cluster/surface system. For well defined crystalline surfaces, however, additional effects may occur which increase the relaxation time, such as the Ehrlich-Schwoebel barrier [69-71]. The location of the nucleation centers at the pit edges indicates a potential minimum for diffusing Au atoms at these sites. In view of the equilibrium state the cluster tends to maximize the number of atoms in contact with these low energy sites. As a consequence, the cluster center will approach the pit edge, in agreement with our STM analysis.

For the cluster volume determination in Chapter 5 we measured the cluster height with respect to the upper HOPG plane. With the analysis of this section the height is systematically too low for all clusters. The height underestimated by 0.35 nm (one layer of HOPG) on a part of the cluster basis results in an error of the volume which ranges from less than 10 % for samples C and D up to about 15 % for the small clusters of sample A. Thus this error may be neglected compared to the systematic error of the volume determination (about 30 %, cf. Chapter 5).

7.3 Photoemission Study

The investigation of the growth process consisting of several evaporation steps is difficult to realize by means of STM. Besides the time consuming counting procedure and the instable imaging of larger clusters, the sample has to be transferred into the STM after each evaporation step. Under these circumstances it is hardly possible to guarantee the sample cleanliness for a large number of evaporation steps which is necessary in order to avoid influences of adsorbates on the growth process. Therefore we decided here to study the cluster growth solely by UPS. It is clear that all results of this section are based on average information of the inhomogeneous sample. The distribution of quantities like the cluster size is not taken into account explicitly, but we henceforth focus on the respective mean values.

7.3.1 Quantitative UPS of Au Clusters

From the UPS spectra of the clusters, such as shown in Fig. 20 (a) and (b), we can extract basically two kinds of information: first the structure of the curves can be analyzed qualitatively by comparison with known bulk structures, in this manner the evolution of the bulk band structure can be investigated. Secondly, the overall Au intensity can serve as a measure for the actual coverage Γ_{sample} on the sample and hence for the condensation coefficient $\mathbf{b} = \Gamma_{\text{sample}} / \Gamma_{\text{evap}}$. Since the cluster density \mathbf{r}_c remains essentially constant, the coverage is proportional to the average cluster volume V . However, the quantitative analysis of intensities is not straightforward, mainly due to the finite escape depth of the photoelectrons in the material. In this section this effect is taken into account explicitly in order to derive more detailed information about the cluster growth process.

Within the three-step model (cf. Sec. 2.3), after the photon excitation the electron propagates through the sample until it reaches the surface. The probability of the escape of an electron through the surface is dependent on its initial depth \bar{z} and is limited by the finite inelastic mean free path (IMFP) I . The number of emitted electrons per area and time $n(\bar{z})d\bar{z}$, originating from a certain depth \bar{z} , can be expressed by:

$$n(\bar{z})d\bar{z} = n_0 \cdot e^{-\bar{z}/I} d\bar{z}, \quad (13)$$

where n_0 is the number of exited photoelectrons per time and sample volume. Since the photon penetration depths exceeds by far the electron IMFP, n_0 is assumed to be constant

within the range of interest. We now consider the photoelectron intensity of a single Au cluster on a surface. The total signal is the sum over the intensities from all depths \bar{z} , weighted with the respective projected areas $A_{\perp}(\bar{z})$. Assuming a reasonable cluster shape with a contact angle $\leq 90^{\circ}$ and $dA(z)/dz \leq 0$, the area $A_{\perp}(\bar{z})$ is simply the cross sectional area $A(z)$ of the cluster at the height $z = \bar{z}$ (now with $z = 0$ at the surface). The number of photoelectrons per time for such a cluster is

$$n = n_0 \cdot \int_0^h A(z) e^{-z/l} dz. \quad (14)$$

At this point we have to introduce a morphology model in order to specify $A(z)$. The simplest case is a cuboid or a cylinder ($A(z) = A_0 = \text{const}$), resulting in

$$n = n_0 \cdot A_0 \cdot I \cdot (1 - e^{-h/l}). \quad (15)$$

Assuming a constant morphology during the growth, i.e., $V = ah^3$, we get

$$n(V) = n_0 \cdot V^{2/3} \cdot a^{1/3} \cdot I \cdot \left[1 - \exp\left(-\frac{1}{I} \left(\frac{V}{a}\right)^{1/3}\right) \right]. \quad (16)$$

The overall UPS intensity I is in addition dependent on the cluster density r_c :

$$I \propto r_c \cdot n(V). \quad (17)$$

Two limits are obvious from Eq. 16: for small clusters the Intensity is directly proportional to the average cluster volume, independent of the morphology model, because the IMFP is well above the cluster heights. For very large clusters the signal is proportional to $I \cdot A_0 = I \cdot a^{1/3} \cdot V^{2/3}$, since the emission from the projected cluster surface dominates. In this limit the intensity is a measure for the fraction of the gold covered substrate area, rather than for the cluster volume, especially in comparison with the bulk Au UPS signal (where the coverage is complete). Consequently, the volume determination is strongly influenced by the chosen morphology model in this limit. Fig. 44 illustrates the change of the photoelectron intensity depending on the cluster volume. The electron escape depth for gold has been determined from the semi-empirical formula

$$I = \frac{A}{E_{\text{kin}}^2} + B\sqrt{E_{\text{kin}}} \quad \text{with } A = 177 \text{ nm} \cdot \text{eV}^2 \text{ and } B = 0.054 \text{ nm} \cdot \text{eV}^{-1/2}, \quad (18)$$

which is given in Ref. [72]. The reference energy for E_{kin} is the Fermi level of the sample ($E_{\text{kin}} = \hbar\mathbf{w} + E$, where E is the energy with respect to the Fermi level as given in the UPS plots). For HeI radiation and the kinetic energy of the electrons in the range of the d-bands of Au we obtain $l \approx 1.0$ nm. The energetic dependence of l is not taken into account here, but we will come to this point below. A cylindrical cluster morphology reveals

$$a = \frac{\mathbf{P}}{4} \left(\frac{d}{h} \right)^2 \approx 0.79 \cdot \left(\frac{d}{h} \right)^2. \quad (19)$$

For the diameter-to-height ratio d/h we use the value which describes the larger clusters ($d/h \approx 2.5$, cf. Sec. 5.2) because for the small clusters the geometric model is less relevant. This is plotted in Fig. 44 together with the limits discussed above. The lower d/h ratio results in a slightly lower count rate (dashed curve) due to the smaller projected surface fraction, but the general trend is unaltered.

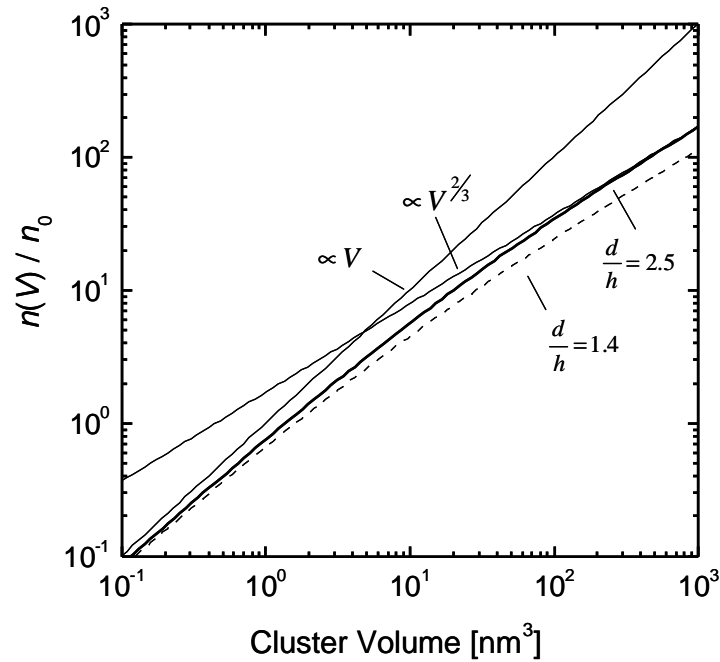


Fig. 44. Calculated photoelectron intensity versus cluster volume, determined with Eq. 16. A cylindrical morphology is used with $d/h = 2.5$ (thick line). The thin lines mark the two asymptotes (see text). In addition the result for $d/h = 1.4$ is presented (dashed line), which corresponds to the experimental findings for small, non faceted clusters. The electron escape depth is set to $l = 1$ nm.

The model can easily be extended to more complicated morphologies like the truncated cone. However, the deviations from the simple cylinder model are negligible compared to

the d/h uncertainty. For clusters larger than about 100 nm^3 the limit $n_{V \rightarrow \infty} = n_0 \cdot A_0 \cdot I$ is nearly reached, thus the UPS intensity should correspond to the projected area of these large clusters:

$$\frac{I_{\text{cluster}}}{I_{\text{bulk}}} \approx r_C \cdot A_0. \quad (20)$$

This is only valid with the constraint $r_C \cdot A_0 \ll 1$ because the total projected area differs from the model $A_0 = a \cdot V^{2/3}$ if the clusters get in contact to each other in the limit of large A_0 . The signal finally approaches the upper limit $r_C \cdot A_0 = 1$ given by a thick gold film and gets constant.

7.3.2 Sample Characterization

The HOPG substrate used for the UPS experiments in Sec. 7.3.3 is shown in Fig. 45a. The surface consists of extremely small, but quite monodisperse nanopits. The number of pits per area is about $r_{\text{pits}} \approx 1300 \text{ nm}^{-2}$ and we expect the formation of one cluster per pit for this sample, resulting in the same cluster density r_C . Thus, this substrate is comparable to that of sample C (cf. Fig. 16 and Fig. 18). For STM measurements the cluster sample after the Au evaporation (sample E) is not well suited because the small pits provide a smaller contact area between HOPG edges and clusters than the previous samples. Hence the probability for tip induced displacement is significantly increased and stable images are difficult to obtain.

The Au evaporation was carried out at $T = 350^\circ\text{C}$ in analogy to the previous samples A ... D. We divided the evaporation into 6 steps, changing the respective exposure such that in each step i the total Au exposure Γ_{evap}^i (i.e. the sum over all previous evaporation steps) is increased by a factor of $\Gamma_{\text{evap}}^i / \Gamma_{\text{evap}}^{i-1} \approx 2.3$. Thus, the evaporated gold amount was changed in constant steps on a logarithmic scale, starting from $\Gamma_{\text{evap}}^1 = 0.04 \text{ ML}$ up to $\Gamma_{\text{evap}}^6 = 2.8 \text{ ML}$. After each step the sample has been cooled down to room temperature and the UPS measurement was started.

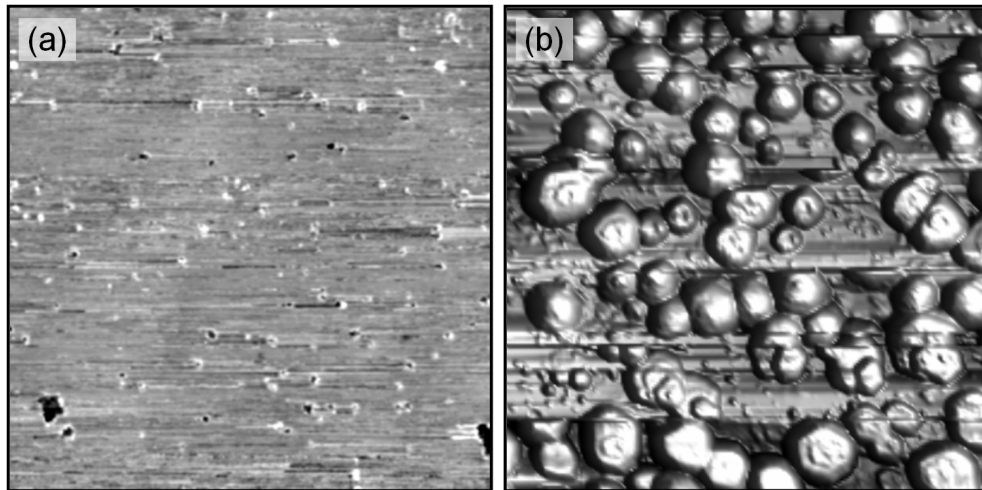


Fig. 45. (a) STM image ($300 \text{ nm} \times 300 \text{ nm}$) of the substrate of sample E, which was used for the UPS experiment. Several pits are only visible as bright spots because of their small diameter.
 (b) Pseudo 3D image ($200 \text{ nm} \times 200 \text{ nm}$) of the same sample after the last evaporation step ($\Gamma_{\text{evap}} = 2.8 \text{ ML}$).

Subsequent to the UPS study we tried to apply STM for the largest clusters ($\Gamma_{\text{evap}} = 2.8 \text{ ML}$), but it was only possible to achieve a rough estimation about the cluster heights and it was extremely difficult to image larger sample areas, such as shown in Fig. 45b. The figure is dominated by the displacement of several clusters during the scan, only a fraction of the clusters could be imaged successfully. The cluster height ranges from $h \approx 3 \text{ nm}$ up to $h \approx 7 \text{ nm}$ and we estimate the average height to $\langle h \rangle \approx 5 \text{ nm}$. The cluster density is consistent with the pit density of Fig. 45a.

7.3.3 Photoemission Results

First we focus on the Au 5d-band structure at the energy of $-7 \text{ eV} \dots -2 \text{ eV}$ with respect to the Fermi level. In Fig. 46 normal emission spectra at $T = 300 \text{ K}$ with low angular resolution ($\pm 8^\circ$) are shown for the lowest and the highest Au coverage, respectively. The HOPG substrate signal has been measured before under the same conditions and is subtracted in order to extract the Au signal (cf. Fig. 20). For each spectrum the Fermi energy was determined separately on a tantalum foil. Whereas the spectrum for the small clusters contains only two broad peaks, the large clusters in the right part of Fig. 46 exhibit all essential structures of the bulk Au(111) surface.

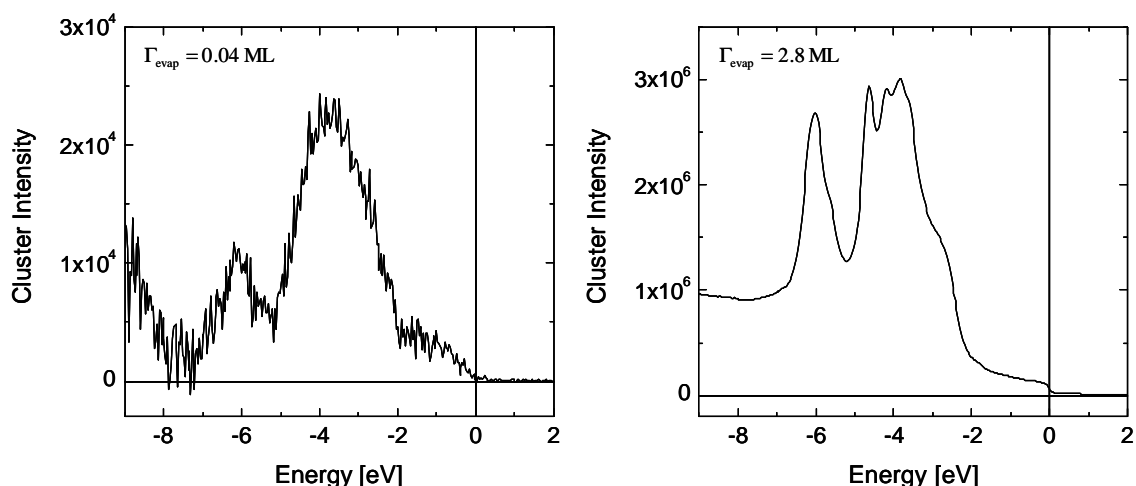


Fig. 46. Photoelectron spectra after subtraction of the HOPG background (cf. Fig. 20) for the lowest (left) and the highest (right) gold exposure used in the experiment. The evaporation was done at $T = 350^\circ\text{C}$, whereas the measurement was performed at room temperature.

Another striking difference is the intensity ratio between the first feature at -6 eV and the second one around -4 eV , which has not reached the bulk value even for the largest clusters with several 10^4 atoms (cf. the low temperature spectrum in Fig. 20d; the ratio does not change significantly at $T = 300\text{ K}$). For possible origins of this effect one might think of the energy dependence of the electron escape depth l , since the electron energies of the two features differ by $\approx 2\text{ eV}$. This effect is expected to be most relevant for small clusters, because then the intensity is proportional to the cluster volume, independent of l (cf. the discussion in the context of Eq. 16). In contrast, the bulk intensity is directly proportional to l . Therefore, the maximum relative change of the intensity ratio can be estimated by $l(17.5\text{ eV})/l(15\text{ eV})$, according to the kinetic energy of the electrons for the two structures. The application of Eq. 18 yields an upper limit of about 25%, which is evidently lower than the observed change. As a result, the increase of the relative intensity of the first structure at -6 eV can only partially be related to the electron escape depth. More likely, the UPS data indicate a change of the actual electronic band structure. This is consistent with the expected size of less than 100 atoms for the small clusters in Fig. 46 (left part). For such small Au particles theoretical and experimental investigations for free clusters [57] as well as photoemission experiments on supported clusters [73] indicate deviations from the bulk behavior. A direct theoretical comparison of the density of states between large metal clusters and the bulk material is given in Ref. [51] for the case of copper.

The evolution of the d-band structure for all Au coverages is visible in Fig. 47a. Note the logarithmic scaling which is used in order to allow a quantitative representation of all spectra in a single plot. The relative intensity of the first peak at -6 eV increases gradually. In contrast, the fine structure in the second feature appears quite suddenly at an exposure around 0.5 monolayers. With regard to the STM measurements for sample B (Fig. 15) and sample C (Fig. 16), the occurrence of the (111) fine structure is in coincidence with the formation of the hexagonal facets discussed in Sec. 5.2. This gives further evidence for a transition of the cluster morphology to well defined crystallites at $\Gamma_{\text{evap}} \approx 0.5 \text{ ML}$.

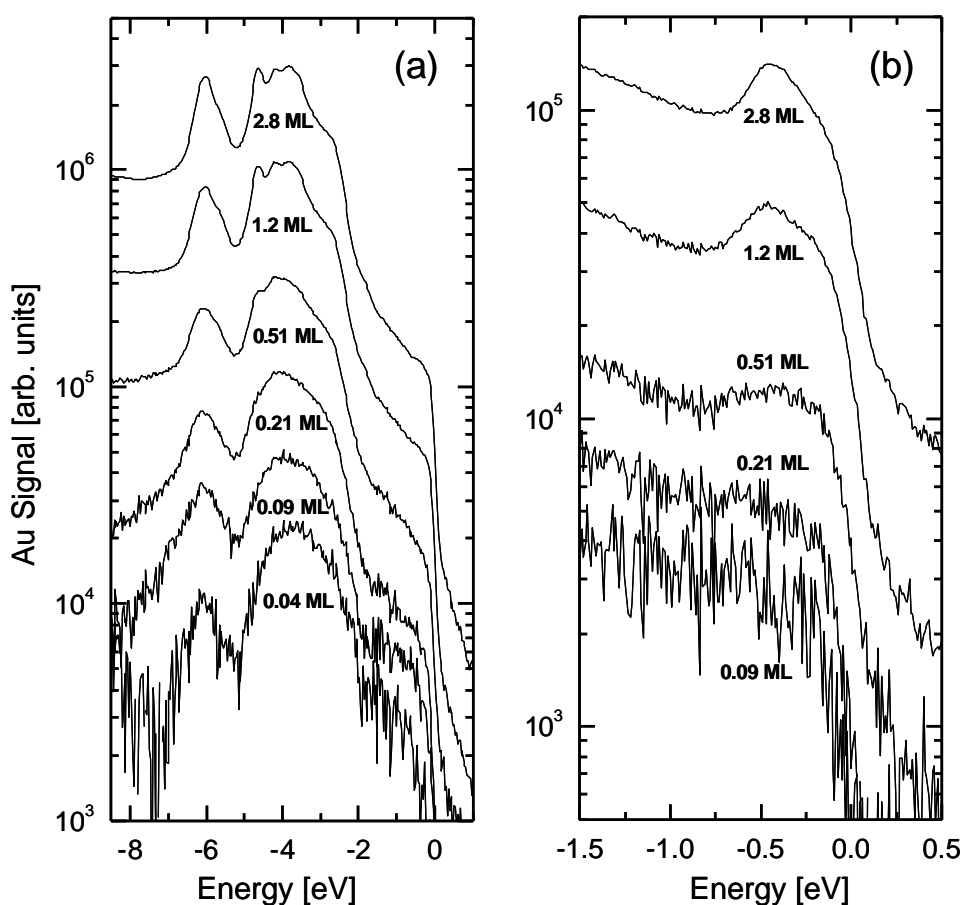


Fig. 47. (a) Background corrected UPS results for 6 different gold exposures for sample E on a logarithmic scale. The Au d-band intensity varies over more than 2 orders of magnitude. The non-vanishing signal above the Fermi level is caused by satellites in the HeI radiation line. (b) Normal emission photoelectron spectra with $\pm 1^\circ$ angular resolution for the region near the Fermi level after subtraction of the HOPG background. For $\Gamma_{\text{evap}} \geq 0.5 \text{ ML}$ the surface state peak is clearly observable. The spectrum for the lowest coverage ($\Gamma_{\text{evap}} = 0.04 \text{ ML}$) is not shown because of the poor signal-to-noise ratio.

The morphology change is also confirmed by UPS measurements near the Fermi level with high angular resolution ($\pm 1^\circ$). In Fig. 47b the peak of the Shockley surface state (cf. Sec. 6.1) occurs at $\Gamma_{\text{evap}} \approx 0.5 \text{ ML}$, in analogy to the Au(111) fine structure of Fig. 47a. Since a well defined (111) surface is necessary for the formation of a Shockley surface state (see Chapter 3), this behavior is not unexpected.

For the following discussion we focus on the evolution of the overall intensity of the d-band spectra of Fig. 47a. The structural change, as well as the mentioned change of the intensity ratio between the two main features is not taken into account. Instead, we assume that the integrated intensity is a measure for the Au quantity on the sample, additionally accounting for the finite photoelectron escape depth as discussed in Sec. 7.3.1. This simplification is tolerable because we are interested in the growth process on a semi-quantitative level. The cluster size dependent change of the UPS d-band spectra will certainly affect the extracted Au quantity, but the errors are expected to remain in the range of a few percent. The intensity change of the first structure at -4 eV , probably one of the largest error sources, result in an underestimated intensity integral of $\approx 10\%$ for the smallest clusters. For the following analysis such deviations are not relevant.

In Fig. 48 the integrated 5d peak intensities are shown in a double logarithmic plot for all six Au coverages of sample E (full circles). The summation is performed over the d-band region ($-7 \text{ eV} \dots -11 \text{ eV}$) of the background corrected data in Fig. 47a. The data points can be fitted quite accurately by a straight line with the slope $m = 1.19 \pm 0.03$, corresponding to the power law

$$I(\Gamma_{\text{evap}}) = c \cdot \left(\frac{\Gamma_{\text{evap}}}{1 \text{ ML}} \right)^m, \quad (21)$$

where I is the integrated photoelectron intensity and c is the intensity at $\Gamma_{\text{evap}} = 1 \text{ ML}$. With regard to the discussion of the coverage-dependent photoelectron intensity in Sec. 7.3.1 this slope corresponds clearly to an increasing condensation coefficient.

The d-band intensities for the samples A, B, C (cf. Sec. 5.2), D (cf. Sec. 6.1), and F (see Sec. 9.2 for a description of sample F) are additionally plotted in Fig. 48. To account for variations in the photon flux and the counter efficiency, the data points for each sample were normalized with respect to the HOPG feature at $E \approx -8.5 \text{ eV}$ (see Fig. 20a, dashed line), which were measured immediately before the respective cluster sample. The exponent derived above is confirmed by the samples A-C, which were also prepared using the same substrate. The different vertical positions of the data points is caused by the

varying cluster density r_c which is included in the prefactor c . The nearly identical prefactors for the samples A-C, as well as E and F are in good agreement with the similar measured cluster densities.

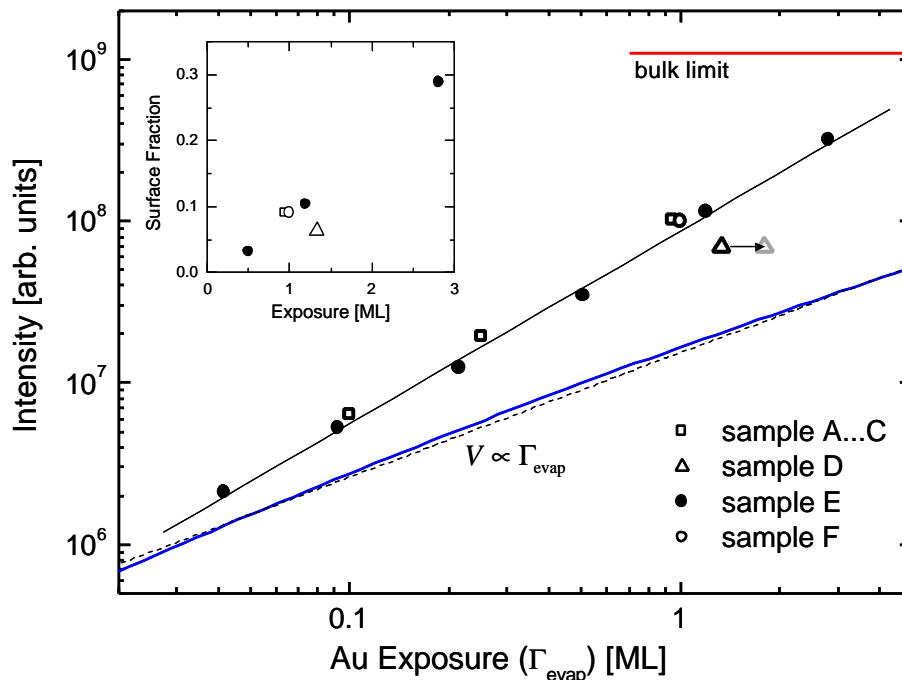


Fig. 48. Double logarithmic plot of the integrated d-band UPS intensity versus the evaporated Au amount for all samples A-F (symbols). The thin solid line is the linear fit for sample E. The expected intensity increase on the assumption of a constant condensation coefficient, i.e., $V \propto \Gamma_{\text{evap}}$ is calculated according to Eq. 16 (thick blue line). The dashed blue line represents the corresponding linear fit. Both curves are shifted arbitrarily in the vertical direction. The red horizontal line in the top right corner (“bulk limit”) is the measured intensity for a bulk Au(111) single crystal surface. For clusters with $\Gamma_{\text{evap}} \geq 0.5 \text{ ML}$, i.e., $\langle V \rangle > 30 \text{ nm}^3$ the limit (20) should become applicable. The corresponding fraction of the Au covered substrate is shown in the inset on a linear scale.

We note that the data point for sample D contains a large error in the horizontal direction, because of the less accurate calibration of the evaporator (cf. Sec. 6.1). The comparison of the mean cluster size derived by STM measurements with those of samples C and F indicates a higher actual Au exposure. This is in agreement with the large difference of the cluster densities $r_c^{\text{C,F}}/r_c^{\text{D}} \approx 3\dots 4$. The supposed true exposure is marked by an arrow in the figure.

The information we are interested in is the dependence of the condensation coefficient on the Au exposure:

$$\mathbf{b}(\Gamma_{\text{evap}}) = \frac{\Gamma_{\text{sample}}}{\Gamma_{\text{evap}}} = \frac{\mathbf{r}_c \cdot \frac{\mathbf{S}}{\mathbf{n}} \cdot V(\Gamma_{\text{evap}})}{\Gamma_{\text{evap}}}, \quad (22)$$

where $1/\mathbf{S}$ is the number of atoms per area for a ML Au and \mathbf{n} is the atomic volume. Note the assumption of independent clusters as discussed in Sec. 7.1. If the condensation coefficient \mathbf{b} was constant during the growth process, i.e., $V \propto \Gamma_{\text{evap}}$, the expected intensity would follow the blue thick line in Fig. 48, which was calculated using Eq. 16 (with $d/h=2.5$) and gives the intensity $I(V)$ in dependence on the cluster volume. We estimated $V(\Gamma_{\text{evap}}=1 \text{ ML})=100 \text{ nm}^3$ from the STM results in Sec. 5.2 and Sec. 9.2, and the curve is shifted in the vertical direction by an arbitrary amount to allow a direct comparison with the experimental data points. Apparently, the slopes of the expected and the measured curves differ significantly from each other, indicating an increase of \mathbf{b} . In order to achieve a more quantitative description of this increase, we approximate the $I(V)$ curve with a power law in analogy of Eq. 21. The result, yielding a slope of $m_{\text{theo}} = 0.77 \pm 0.04$, is indicated in Fig. 48 by a dashed line. In the further discussion we will restrict all curves in Fig. 48 to the power law approximation, i.e., straight lines in the double logarithmic plot. From the combination of $I(V) \propto V^{m_{\text{theo}}}$ and $I(\Gamma_{\text{evap}})$ following Eq. 21 one gets

$$V(\Gamma_{\text{evap}}) \propto (\Gamma_{\text{evap}})^{m/m_{\text{theo}}}, \quad (23)$$

and the condensation coefficient increases according to $\mathbf{b}(\Gamma_{\text{evap}}) \propto (\Gamma_{\text{evap}})^l$ with an exponent of $l = m/m_{\text{theo}} - 1$ (see Eq. 22). For the obtained slopes this results in $l = 0.5 \pm 0.1$, where the error results from the respective statistical standard deviations of the linear fits. The total error is expected to be larger due to the limited validity of the involved models. Nevertheless, the UPS intensity provides clear evidence for an increase of the condensation coefficient. This fact is in agreement with kinetic growth models which will be discussed in Sec. 7.4.

In the limit of large clusters Eq. 20 is applicable, yielding the fraction of the Au covered substrate area without the use of any geometrical model. In Fig. 48 the integrated intensity of a Au(111) single crystal (measured at room temperature) is indicated by a horizontal red line in the top right corner. The inset shows the d-band intensity, normalized to the bulk signal for the larger clusters on a linear scale. This gives directly the surface fraction of the clusters and is thus provides a complementary information to the STM measurement,

which mainly provides the cluster height. The additional information can be used to verify the truncated cone (or octahedron) model for the cluster morphology as presented in Sec. 5.2. Using the model we calculate the fraction of the interface areas between the clusters and the substrate with respect to the total area. The results for the different samples using the truncated cone model are summarized in Table 5. The good agreement between the UPS data and the model confirms the suggested morphology. The STM values were calculated using $r_c \cdot \langle A_0 \rangle$, where r_c is the cluster density and $\langle A_0 \rangle$ the mean bottom area of the truncated cones. The differences between the truncated cone model and the truncated octahedron model are negligible (cf. Sec. 5.2).

sample	surface fraction (UPS)	surface fraction (STM + model)
C	9.2 %	9.1 %
D	6.3 %	≈ 5 %
F	9.0 %	8.2 %

Table 5. Ratio between the Au/HOPG interface area and the total sample area, determined by UPS (2nd column) and STM (3rd column), respectively. The accuracy of the STM value for sample D is rather low because of the poor STM statistics (only 13 clusters).

For all samples of Fig. 48, except for the largest clusters on sample E, the maximum gold covered surface is about 10 % of the total area. This justifies a posteriori the background subtraction procedure for the UPS data and the calculation of the projected area (cf. Eq. 20) using the truncated cone model.

The comparison of the last two evaporation steps of sample E results in an increase of the projected area by a factor of ≈ 2.8 , which is very close to the increase of the evaporated Au amount of $\Gamma_{\text{evap}}^6 / \Gamma_{\text{evap}}^5 \approx 2.3$. This can only be explained by a predominant two dimensional growth of these large clusters. From the STM image of the sample after the last evaporation step (Fig. 45b) one can estimate a diameter-to-height ratio of $d/h \approx 4...5$ for the larger clusters, which is significantly more than the measured $\langle d \rangle / \langle h \rangle \approx 2...3$ for samples C and F (in both cases the truncated cone diameter at the half height is taken). Thus a transition from 3D to 2D growth at a cluster size of $N \approx 10^3...10^4$ is also confirmed by the photoemission measurements.

7.4 Growth Model

In this section we try to interpret the experimental growth results in view of a microscopic kinetic model. Since many of the required parameters like the diffusion length before desorption I_{diff} or the size dependent morphology (described, e.g., by d/h) are not known with a high quantitative accuracy, the analysis will remain on a qualitative level. In addition non ideal experimental conditions complicate the modeling as, e.g., potential deviations from the perfect statistical distribution of nucleation centers (particularly for large pits, cf. Sec. 7.1) or the diffusion along monoatomic steps or pit edges.

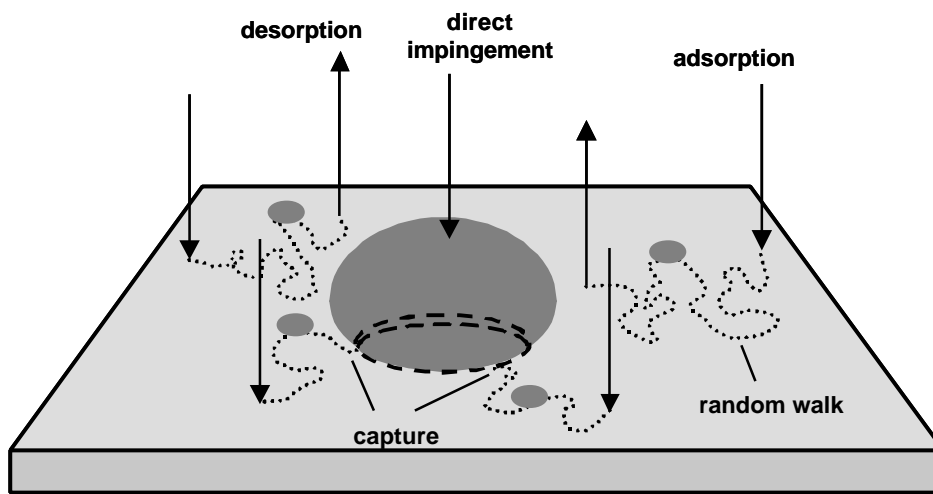


Fig. 49. Schematic representation of the cluster growth process. See text for details.

Simple growth models have been successfully applied for diffusing Au atoms on graphite in the past [63,64,74]. Here we use the model presented in Refs. [63,64]. The assumed growth mechanism is illustrated in Fig. 49. The adsorbed Au atoms diffuse on the surface, performing a random walk. After a typical path length I_{diff} they desorb again. If an atom hits a nucleation center or an existing cluster during the random walk, it is captured and the cluster size increases. Another contribution to the growth is given by the direct impingement of Au atoms from the gas phase. For both processes we assume that the sticking coefficient between the Au atom and the cluster is equal to 1, i.e., once an atom is linked to a cluster, the probability of a later escape is negligible.

For a cluster with a circular ground area (radius R) the capture probability of an adatom in a distance r is [63]

$$P_c(r, R) = \frac{K_0(r/I_{\text{diff}})}{K_0(R/I_{\text{diff}})}, \quad (24)$$

where K_0 is the zero order modified Bessel function of the second kind. For an infinitesimal Au exposure $d\Gamma$ (in ML) the number of captured atoms dN_{capt} is the integral over all distances r from the cluster edge R to the outer border of the capture zone r_l , multiplied by the number of atoms per area $d\Gamma_A = d\Gamma/s$. Here, s is the area per atom for one monolayer (in $\text{ML} \cdot \text{m}^2$). Within the approximation of independent clusters (i.e., $r_l \rightarrow \infty$) the integration yields

$$dN_{\text{capt}} = 2p \frac{d\Gamma}{s} \int_R^{\infty} \frac{K_0(r/I_{\text{diff}})}{K_0(R/I_{\text{diff}})} r dr = 2p \frac{R I_{\text{diff}}}{s} \frac{K_1(R/I_{\text{diff}})}{K_0(R/I_{\text{diff}})} d\Gamma. \quad (25)$$

Note that in the right part of the equation the order of the Bessel function in the numerator has increased to one. The second contribution dN_{imp} due to the direct impingement of Au atoms is proportional to the projected area of the cluster:

$$dN_{\text{imp}} = \frac{p R^2}{s} \cdot d\Gamma. \quad (26)$$

The volume V of a cluster in dependence of the gold exposure Γ_{evap} is then

$$V(\Gamma_{\text{evap}}) = p \frac{n}{s} \left(2 I_{\text{diff}} \int_0^{\Gamma_{\text{evap}}} R(\Gamma) \cdot \frac{K_1(R(\Gamma)/I_{\text{diff}})}{K_0(R(\Gamma)/I_{\text{diff}})} d\Gamma + \int_0^{\Gamma_{\text{evap}}} R^2(\Gamma) d\Gamma \right), \quad (27)$$

where n is the atomic volume of gold. Eq. 27 can be solved iteratively, starting at a sufficiently small value Γ_{evap}^0 . In each iteration step i the corresponding volume V^i can be evaluated with the given Γ_{evap}^i , which provides the bottom radius R^{i+1} for the next step. The number of atoms per cluster is $N(\Gamma_{\text{evap}}) = V(\Gamma_{\text{evap}})/n$. The result depends strongly on the chosen morphology model $R(V)$. Two limits are considered here: the 3D growth is modeled by a cylindrical geometry with $d/h = 2.5$ (cf. Sec. 7.3.1), whereas for a 2D growth we assume islands with a height of one monolayer. The results are shown in Fig. 50 together with the experimental mean cluster size from STM measurements of samples A, B, C and F, respectively. As the only parameter we adjusted I_{diff} to obtain a considerable agreement between theory and experiment, which is the case for $I_{\text{diff}} = (8 \pm 1) \text{ nm}$. This is

still consistent with the value $I_{\text{diff}} = (5.8 \pm 2.4) \text{ nm}$ deduced in Ref. [64] for the same temperature $T = 350^\circ\text{C}$ as used here.

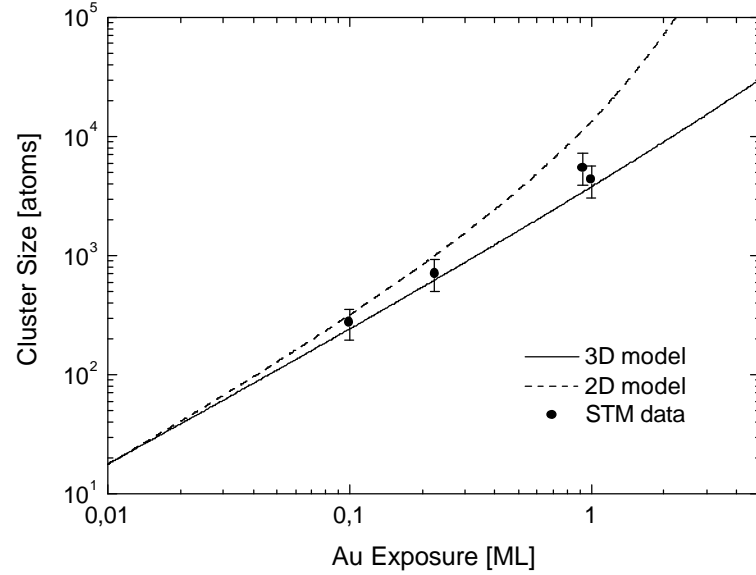


Fig. 50. Simulated cluster size versus the Au exposure from the evaporator in a double logarithmic plot. In the case of a 2D monolayer growth (dashed line) the cluster size increases faster than for a 3D cylinder morphology (solid line) due to the larger capture radius and the increased direct impingement probability. The measured data points represent the mean cluster size determined by STM. The error of 30 % is estimated from the imprecise heights (cf. Sec. 5.1).

As pointed out above, the hitherto analysis of the cluster growth has been done on a semi-quantitative level due to the simplifications induced by the models and the limited experimental accuracy. The contribution of the direct impingement is expected to lead to a predominant vertical growth caused by the Ehrlich-Schwoebel barrier [69-71] at the edge of the top facets. This would result in a deviating bottom radius R in Eq. 27. In addition the overlap of the capture areas of neighboring clusters are expected to influence the growth, particularly for large clusters [63].

However, the essence of this section is the observation of an increasing condensation coefficient, i.e., $m/m_{\text{theo}} > 1$, together with the plausibility check using a simple growth model. For the preparation of samples with large clusters the observed change of the condensation coefficient has to be taken into account. Due to the nonlinear behavior for larger exposures even a deviation of a few percent of the evaporated Au amount may result in a drastic change of the cluster sizes.

8 Dynamic Final State Effect

The photoemission data of supported metal clusters presented hitherto were discussed in view of the initial density of states. Generally, the measured quantity in UPS is the joined density of states (cf. Sec. 2.3), thus final state effects have to be taken into account. The final state in the case of free clusters is characterized by the excited photoelectron and the corresponding hole in the cluster (see Fig. 51a). The lifetime of the positive charge on the isolated cluster is large compared to other timescales of the experiment, allowing a description from the static point of view. If the clusters are coupled to a substrate, the situation is different and the dynamics of the photoemission process becomes important (Fig. 51b). In this section a simple model is discussed which allows to describe the influence of this “dynamic final state effect” on a quantitative level. For the experimental investigation of this effect silver as a cluster material is better suited than gold because of the absence of the surface state near the Fermi edge due to the more spherical morphology, showing no indication for flat top facets [27,28]. Nevertheless, the application on Au clusters is straightforward, as will be shown in Sec. 9.1.

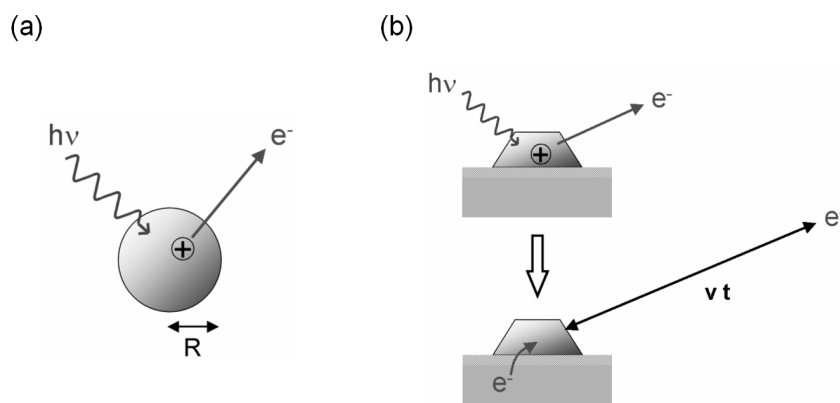


Fig. 51. Schematic illustration of the photoemission process from a metal cluster.

(a) For a free cluster the photohole persists within the relevant electron-hole interaction time and the kinetic energy of the photoelectron is lowered according to Eq. 30.

(b) Immediately after the photoexcitation in a supported cluster the electron-hole interaction is analogous to (a). At a certain time t the photohole may be screened or neutralized and the corresponding change of the interaction affects the kinetic energy of the electron. The smaller the distance vt is at the time t , the larger the influence on the kinetic energy is.

8.1 Model

Already several years ago so-called “postcollision effects” were the subject of intense research. Originally investigated for collisions between atoms and ions [75], the interest shifted to core level photoemission experiments, where slow “threshold” electrons are influenced significantly by these effects because they are still close to the primary ionized atom on the timescale of the core hole decay, which is partly accompanied by an Auger electron emission (for a review see e.g. Ref. [76]). The closer the threshold electron is to the excited atom during its core hole decay, the larger is the energy loss for the threshold electron and the energy gain for the Auger electron. The statistical nature of the core hole decay leads to a distinct broadening of the corresponding threshold and Auger electron lines. Often, semiclassical theories are sufficient to reproduce the experimental data [77].

If molecules adsorbed on a surface are studied, the postcollision process gets modified by screening [78], which mainly reduces the total magnitude of the energetic shifts, leading to smaller broadening effects, i.e. to more narrow electron lines. In addition screening charge transfer effects can lead to double peak structures [79].

For free, i.e. non-deposited molecules or clusters, the singly positive charge state due to photoelectron emission from valence states close to the Fermi energy by ultraviolet or X-ray photons remains constant over a time scale sufficient to let the photoelectron completely escape (cf. Fig. 51a). As a result, well defined, sharp spectral electron lines are obtained. Higher charge states which occur for multiple photoionization lead to the superposition of several photoelectron spectra with relative shifts given by the charging energy [80]. In the case of large metal clusters, the energy difference between two charge states can be calculated in good approximation by the classical value given by $e^2/4\pi\epsilon_0 R$ with R being the cluster radius. For the absolute energetic position with respect to the corresponding bulk material (defined by the limit $R \rightarrow \infty$) the size dependent change of the work function has to be considered in addition. For the difference between the ionization energy of a cluster and the work function of the corresponding bulk material this can be approximated by an additional factor α of the order of 1, depending mainly on the electron density of the metal [81].

For metal clusters deposited onto a substrate, the size dependent energetic shift is altered due to the additional interaction with the surface (cf. Fig. 51b). However, unlike the postcollision induced effects for threshold electrons described above, here they lead to an enhanced broadening of the spectral lines. This can be attributed to the statistical nature of the screening or charge transfer processes itself. The total energy is not shared by the

photoelectron and an Auger-electron, but some fraction is transferred to the cluster/surface system. As a consequence, characteristic distortions of the spectral features close to the Fermi level occur. It turned out that a semiclassical model was sufficient to reproduce the dynamic final state effect in the experimental data (see Sec. 8.2). Within the model, the elimination of the positive charge is described by a characteristic time t . The probability that the charge is eliminated during the time interval $[t, t + dt]$ is given by [27,28]

$$P(t) dt = (1/t) \exp(-t/t) dt. \quad (28)$$

In order to calculate the energy of the electron arriving at the electron analyzer, we need the potential $W(r)$ acting on the electron on its way from the cluster to infinity, with r being the distance from the center of the cluster. A simple formula is given by

$$W(r) = W_{\max} - \frac{ae^2}{4\pi\epsilon_0} \frac{1}{r}, \quad (29)$$

which fits the limiting cases $W(R) = 0$ and $\lim_{r \rightarrow \infty} (W_{\max} - W(r)) \propto 1/r$. If the influence of the positive charge vanishes at the time t , the total energy loss of the photoelectron compared to the case of a neutral cluster is $W(R + vt)$, where v is the photoelectron velocity. Thus, the constant W_{\max} in Eq. 29 corresponds to the maximum energy shift for $t \rightarrow \infty$. In the case of a free cluster this shift is roughly the difference between its ionization potential and the work function of the bulk material [82]. A semiclassical density variational calculation for free silver clusters has shown that the shift follows the relation

$$W_{\max}^{\text{free}} = \frac{ae^2}{4\pi\epsilon_0} \frac{1}{R} \quad (30)$$

with $a = 0.41$, in agreement with experimental results for small silver clusters [83]. For supported clusters, however, the actual maximum shift W_{\max} may differ from Eq. 30. Details of the cluster-surface coupling and of the individual cluster morphology are expected to induce deviations from the simple potential expression in Eq. 29, as well as from the assumption of a universal characteristic time t according to Eq. 28. In practice we will treat W_{\max} as a fit parameter and use Eq. 30 for a plausibility check of the result. The statistical nature of the time t (cf. Eq. 28) leads to a distribution of energy shifts, even if all clusters are identical in radius and coupling to the substrate. The time distribution (Eq. 28) can be transformed into an energetic one:

$$P(W)dW = P(t(W)) \frac{dt}{dW(t)} dW, \quad W \in [0, W_{\max}]. \quad (31)$$

Inserting $W(R + vt)$ one gets with $C = R/vt$

$$P(W)dW = \frac{CW_{\max}}{(W_{\max} - W)^2} \exp\left(-\frac{CW}{W_{\max} - W}\right) dW. \quad (32)$$

This function is plotted in Fig. 52a for several values of C , giving the magnitude of the cluster-substrate interaction. For $C \ll 1$ (i.e., $t \rightarrow \infty$) the distribution approaches a \mathbf{d} function located at $W = W_{\max}$. For $C \gg 1$ (i.e., $t \rightarrow 0$) the photohole is immediately eliminated and $P(W)$ approaches a \mathbf{d} function centered at $W = 0$.

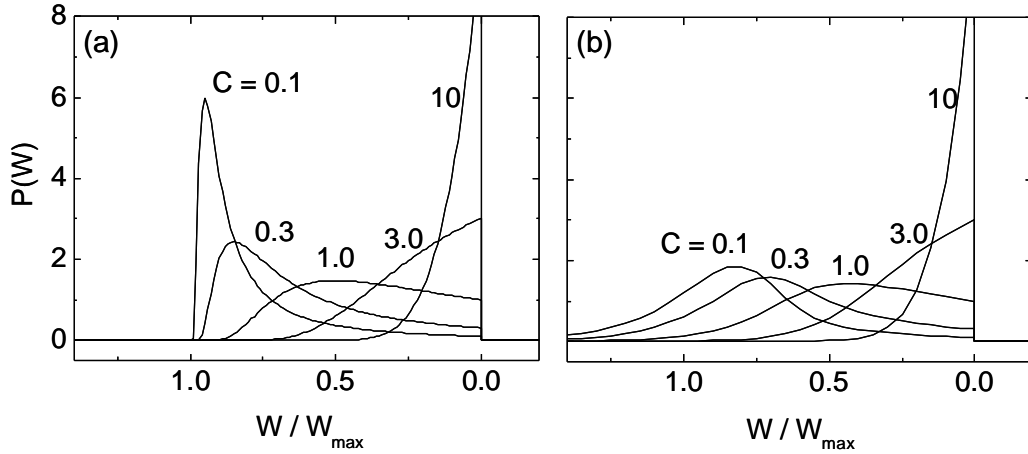


Fig. 52. Calculated distributions $P(W)$ for different coupling values C . The curves were calculated for (a) monodisperse clusters according to Eq. 32 and (b) for a size distribution of $R = \langle R \rangle \pm 0.2\langle R \rangle$ using Eq. 34. From Ref. [28].

The expected experimental spectrum $d(E)$ can be calculated by a convolution of the intrinsic function $f(E)$ (which approaches the bulk spectrum for large clusters) with the distribution of energy shifts $P(W)$:

$$d(E) = P(E) \otimes f(E) = \int_{-\infty}^{+\infty} P(W) f(E - W) dW. \quad (33)$$

Resolution induced broadening effects are neglected here. The afore mentioned limiting case $C \ll 1$ results in a simple shift of the spectrum by W_{\max} , whereas the effect vanishes for $C \gg 1$. In the intermediate region the shift is associated with a broadening of spectral features.

If we assume a radius dependency of W_{\max} according to Eq. 30 the cluster size distribution will affect the shape of $P(W)$:

$$P(W) = \int_0^{+\infty} g(W_{\max}) \frac{CW_{\max}}{(W_{\max} - W)^2} \exp\left(-\frac{CW}{W_{\max} - W}\right) dW_{\max} , \quad (34)$$

with $g(W_{\max})$ being the probability function of W_{\max} . The result for a Gaussian radius distribution with $R = \langle R \rangle \pm 0.2\langle R \rangle$ is plotted in Fig. 52b for the same values of C as for the monodisperse clusters. Interestingly, the size distribution does only provide a significant influence in the range $C < 1$. For broader size distributions of the width $s \equiv s_R / \langle R \rangle \geq 0.5$ a log-normal distribution should be used instead of the Gaussian in order to avoid an unphysical step at $R = 0$ (cf. Eq. 41 in Sec. 9.2).

8.2 Experimental Results

The change of the Fermi-edge shapes induced by the dynamic final state effect is most clearly seen at low temperatures where the thermal broadening is negligible. These low temperature spectra, which were the topic of a previous study [27], are reviewed in Sec. 8.2.1.

The influence of the electron velocity can be investigated even at room temperature, in spite of the thermal broadening, if the photon energy is varied over orders of magnitude [84]. This concept was tested during this work and is discussed in Sec. 8.2.2.

8.2.1 Previous Low-Temperature UPS Experiments

We now investigate the shape of the Fermi edge, which can be approximated by a step function for low temperatures. The dynamic final state model predicts spectra as shown in Fig. 53 for several coupling values $C = 10^{-3} \dots 10^2$. For uniform cluster sizes one gets the dashed curves and the consideration of a size distribution with $R = \langle R \rangle \pm 0.2\langle R \rangle$ results in the solid curves in Fig. 53. In the intermediate region $C \approx 1$ the dashed spectra are nearly identical to the solid ones. Whereas the upper edge is always rounded for inhomogeneous cluster samples, a characteristic sharp kink at the Fermi energy exists for both regimes.

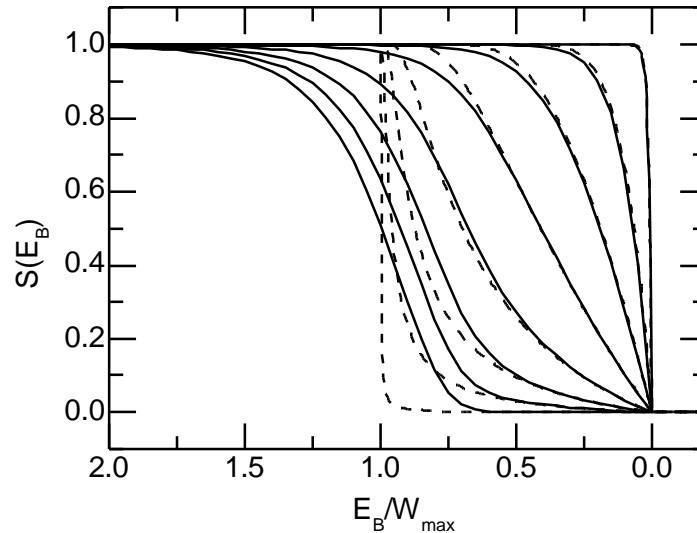


Fig. 53. Expected shapes of the Fermi edge within the dynamic final state model. The abscissa is rescaled in order to drop the dependence on W_{\max} and the intensity is normalized to 1. For monodisperse clusters the two limiting cases $C \ll 1$ and $C \gg 1$ result in sharp edges (dashed lines), whereas a finite size distribution (here $R = \langle R \rangle \pm 0.2\langle R \rangle$) results in a broadening, in particular for $C \ll 1$ due to the corresponding distribution of W_{\max} (solid lines). From Ref. [27].

The photoelectron spectrum for silver clusters with $\langle h \rangle = (3.9 \pm 0.8)$ nm (i.e. $R = \langle R \rangle \pm 0.2\langle R \rangle$), measured at $T = 40$ K (see Fig. 54, top) could be described by the model by choosing $C = 3.0$ and $W_{\max} = 0.49$ eV. According to Eq. 30 the latter value deviates significantly from the charge energy $W_{\max}^{\text{free}} = 0.23$ eV of a free silver particle with $R = 2.5$ nm, which is the radius of a sphere with the same volume as the average cluster size within the truncated sphere model (cf. Eq. 3). But this is not unexpected as discussed above. The fit value of C corresponds to $t = 0.3 \cdot 10^{-15}$ s, pointing to an electron dynamics on the femtosecond timescale.

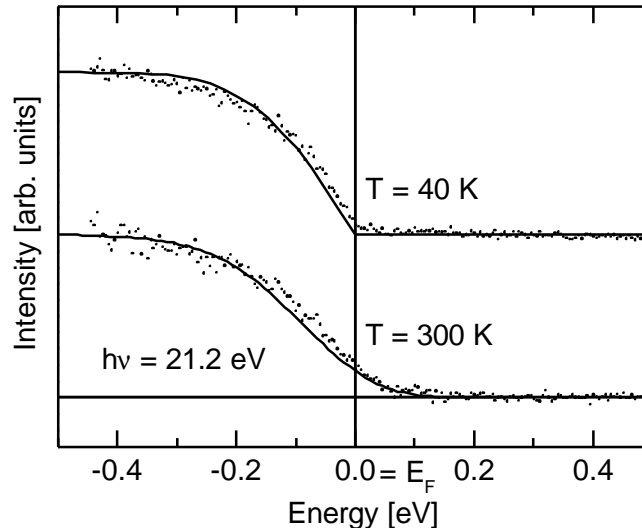


Fig. 54. UPS spectra (dots) near the Fermi energy at $T = 40$ K (top curve) and at room temperature (bottom curve), respectively. The solid lines are the corresponding model fits (see text). For the convolution according to Eq. 33 we used a step function for the upper curve and a room temperature Fermi function for the lower one. From Ref. [27].

At room temperature the characteristic kink at the Fermi level vanishes and the spectrum seems to be very similar to a shifted Fermi edge (Fig. 54, bottom). This shows that the measurements at low temperatures are advantageous for the investigation of the dynamic final state effect. Nevertheless, the full information about $P(W)$ is in principle also contained in the room temperature spectra and utilizing sophisticated deconvolution techniques it is possible to extract it (cf. Sec. 8.2.2).

8.2.2 Photon Energy Dependence

Within the dynamic final state model presented in Sec. 8.1 the shape of the spectra is determined by the parameters W_{\max} and C . Since C is proportional to the inverse photoelectron velocity v^{-1} , the choice of the photon energy is expected to affect the curves in a characteristic manner. In this subsection the role of the photon energy is investigated systematically by combining UPS and X-ray photoelectron spectroscopy (XPS) for the same sample. The experiments were done in cooperation with the University of Ulm (H.-G. Boyen, P. Ziemann) and the University of Basel (M. G. Garnier, P. Oelhafen) [84].

The preparation of the cluster sample followed the method described in Chapter 4. Here, silver atoms were evaporated onto the substrate held at room temperature. The cluster size

could be estimated in situ by using the UPS signal of the Ag d-bands and comparing it to former combined UPS/STM studies [26]. The UPS spectrum of the clean HOPG was determined before the evaporation to allow for later background subtractions. Additionally, after completion of the XPS/UPS experiments, the cluster size distribution was measured by STM ex situ. In this way, an average cluster height of $\langle h \rangle = (6.1 \pm 1.4)$ nm was determined. From this value an average cluster radius can be deduced assuming a diameter-to-height ratio of $\langle d \rangle / \langle h \rangle \approx 1.4$ (cf. Sec. 5.1).

The photoelectron spectra were measured with an electron spectrometer using monochromatized Al K_a radiation ($\hbar\omega = 1486.6$ eV) as well as by UPS using a gas discharge lamp (HeI, $\hbar\omega = 21.2$ eV). All spectra were taken with the sample at room temperature. For the XPS data, an overall energy resolution of 0.36 eV full width at half maximum could be achieved. The resolution is significantly improved for the UPS measurements and, in this case, the broadening of the bulk Fermi edge is mainly given by the thermal width. For XPS as well as for UPS a polycrystalline Ag sample was measured with identical electron spectrometer parameters providing a reference for the position of the Fermi edge, the thermal broadening and the energy resolution.

The experimental photoelectron spectra close to the Fermi edge are shown in Fig. 55. Using both photon energies, the spectra obtained for the Ag clusters are compared to those of the polycrystalline Ag bulk sample. For clusters containing approximately 10^4 atoms (according to Eq. 3) as used here we can assume that the initial state electronic structure of the clusters is very close to the corresponding bulk material with a clear Fermi edge, as it was observed with photoelectron spectroscopy for free Al clusters of this size [80]. The HOPG background spectrum was subtracted from the UPS data. For the XPS signal, however, a background subtraction was not necessary, since the clean HOPG substrate contributes only a negligible intensity. For each XPS spectrum two lines are given in Fig. 55: The thin lines represent the data as measured; for the thick lines a smoothing over 13 data points was performed. The excellent agreement obtained for both bulk data sets demonstrates that, within the given broadening, the smoothing procedure does not change the shape of the spectra.

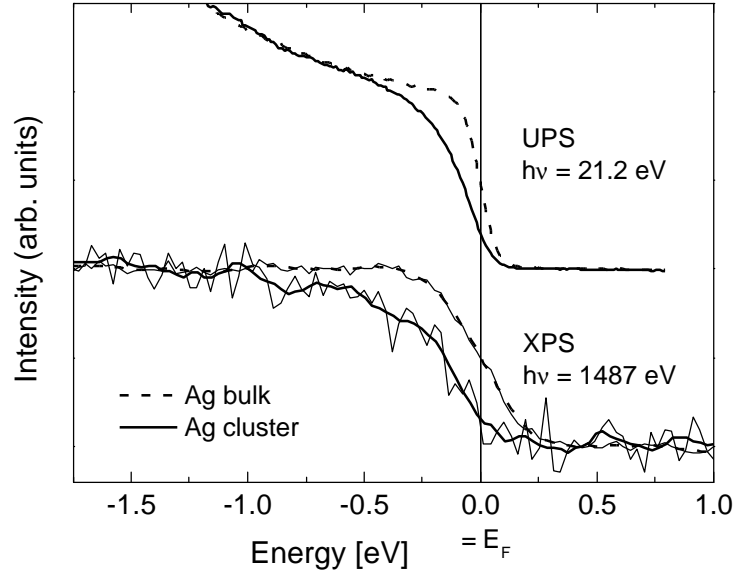


Fig. 55. Photoelectron spectra as experimentally determined by UPS (top) and XPS (bottom) on Ag bulk samples (dashed lines) or Ag clusters on a HOPG substrates (solid lines). For the UPS cluster spectrum, the background signal measured for the clean HOPG sample was subtracted, while in case of XPS the corresponding background was negligible. In all cases, otherwise identical parameters were used. For XPS two lines are given for each spectrum: the thin lines give the data as measured, the thick lines are obtained by averaging over 13 data points. The spectra are vertically shifted for clarity.

To analyze the cluster spectra, first the dynamic final state effect is considered by convoluting the measured spectrum for the bulk sample with $P(W)$. The bulk spectrum naturally includes all processes leading to broadening, thermal effects as well as those due to the finite energy resolution. A log-normal distribution was assumed for the cluster sizes with a relative width of $s = 0.2$. This corresponds to the cluster size distribution for our preparation method as experimentally observed by STM and TEM [22] in agreement with the cluster height distribution determined here.

The convoluted spectra should now fit to both, the UPS and XPS data, simultaneously, with two additional conditions: the same parameter W_{\max} has to be used in both cases, and we demand $C_{\text{XPS}} = C_{\text{UPS}}/10$, because this is the prediction of the dynamic final state model for electrons at the Fermi level with

$$\frac{\nu_{\text{XPS}}}{\nu_{\text{UPS}}} = \sqrt{\frac{\hbar\omega_{\text{XPS}} - \Phi}{\hbar\omega_{\text{UPS}} - \Phi}} \approx 10, \quad (35)$$

using the photon energies given above and the bulk Ag work function $\Phi = 4.7$ eV [85]. Considering exclusively UPS spectra, it turned out that the fitting procedure does not lead

to an unique result. Different C and W_{\max} pairs reproduced the shape of the cluster UPS spectrum with the best fitting obtained in the limit of extremely large C and unphysical large W_{\max} , e.g. $C_{\text{XPS}} = 10$ and $W_{\max} = 100$ eV. Only by simultaneously fitting the XPS spectra with an identical W_{\max} and a fixed $C_{\text{XPS}} = C_{\text{UPS}}/10$, it is possible to arrive at unique and meaningful parameters $C_{\text{UPS}} = 2$, and correspondingly, $C_{\text{XPS}} = 0.2$. The resulting $W_{\max} = 0.33$ eV is again about a factor of two larger than the value of $W_{\max}^{\text{free}} = 0.15$ eV (see discussion in Sec. 8.1), calculated according to Eq. 30 with an equivalent radius of a sphere representing a volume equal to the average cluster size using the truncated sphere model. The comparison between experimental and calculated spectra and the respective $P(W)$ distributions are shown in Fig. 56.

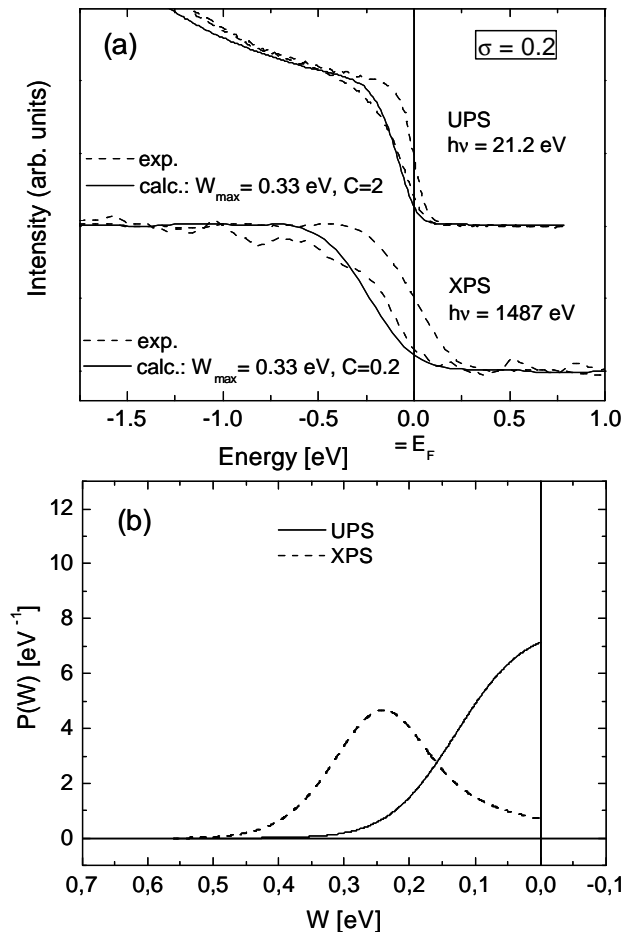


Fig. 56. (a) Experimental cluster and bulk photoelectron spectra (dashed lines, cf. Fig. 55) and fit of the cluster data by convoluting the bulk spectra with $P(W)$ (solid lines). For the statistical broadening we used $\sigma = 0.2$, which corresponds to the distribution of cluster heights as measured by STM. (b) $P(W)$ as assumed for the fit of the UPS and XPS spectra in Fig. 56a.

The experimental shape of the Fermi level onset is not fully reproduced by the calculated spectra in Fig. 56a, which is most obvious for the UPS data due to the better energy resolution and statistics as compared to XPS. The agreement can be clearly improved by allowing for a broader statistical distribution of W_{\max} using $s = 0.5$. A good simultaneous fit to both, the UPS and XPS spectra is then obtained, as shown in Fig. 57, with slightly modified parameters: $C_{\text{UPS}} = 1.5$ (correspondingly $C_{\text{XPS}} = 0.15$) and $W_{\max} = 0.34$ eV.

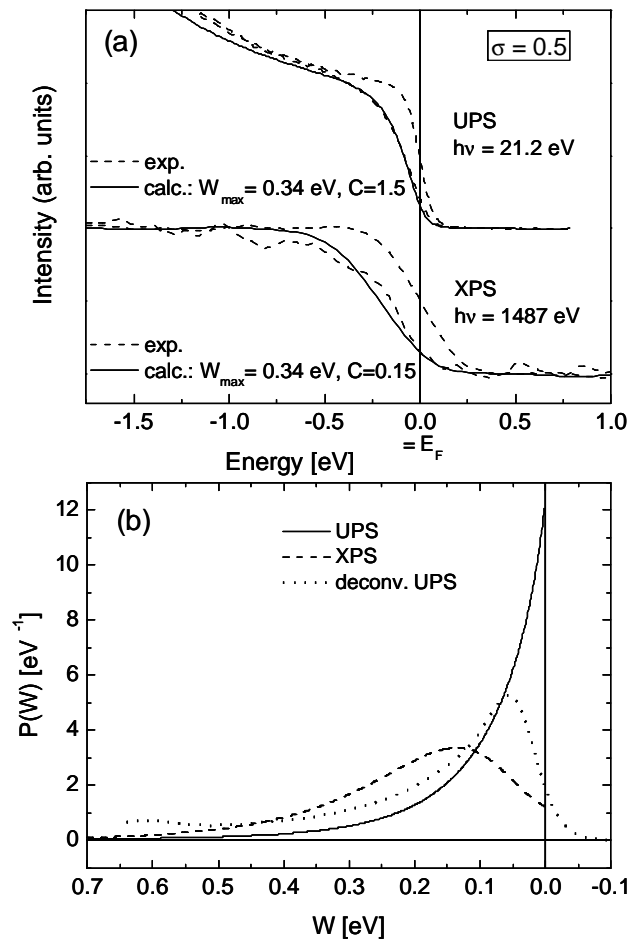


Fig. 57. (a) Experimental cluster and bulk photoelectron spectra (dashed lines, cf. Fig. 55) and fit of the cluster data by convoluting the bulk spectra with $P(W)$ (solid lines). A larger statistical broadening ($s = 0.5$) than in Fig. 56 is used resulting in improved fits. (b) $P(W)$ used for the fit of the UPS and XPS spectra in Fig. 57a. In addition the result of a direct deconvolution of the UPS data is shown (dotted line).

Due to the broad Fermi edges of the room temperature measurements the detailed shape of the underlying distribution $P(W)$ is not obvious. A more direct comparison would be

possible by extracting the experimental $P(W)$ from the spectra and comparing it directly with the model function as given in Eq. 34. The necessary operation is the inversion of Eq. 33, i.e., a deconvolution of the two Fermi edges (cluster and bulk, respectively). For this purpose we use a state-of-the-art deconvolution technique described in detail in Appendix 11.2, which is based on a Maximum Entropy Method (MEM) with additional consideration of intrinsic correlations. This “Adaptive Kernel Maximum Entropy Method” (AK-MEM) was first presented in Refs. [86,87] and is extended in this work in order to allow for negative functions and an automatic noise scaling procedure for unknown experimental errors. Different from the usual application, where the apparatus function is known and one is interested in the original intrinsic function, now two step functions are given and we search for $P(W)$ with the typical properties of an apparatus function (normalized to 1, $\lim_{P(W) \rightarrow \pm\infty} = 0$). For numerical reasons this problem is more difficult, mainly because the normalization of the experimental spectra is impossible (they do not approach zero for large negative energies). To overcome this problem we extrapolated the spectra by a constant value and correspondingly adapted the convolution matrices (cf. Eq. 55) in order to suppress boundary effects. A precondition for the meaningful application of the deconvolution of two step functions is a signal-to-noise ratio of at least ≈ 0.01 which requires more than 10^4 counts. The statistics of the XPS data is not sufficient, but the UPS data could be processed successfully. The maximum posterior (MAP) result $P_{\text{UPS}}(W)$ is included in Fig. 57b (dotted line). The broadening at $W = 0$ is partly given by numerical reasons, and the continuous decrease for larger W is closely related to the result of the dynamic final state effect with $\mathbf{s} = 0.5$ (solid line in Fig. 57b) without a point of inflection, in contrast to the $P_{\text{UPS}}(W)$ for $\mathbf{s} = 0.2$ (cf. Fig. 56b).

The broad distribution of cluster radii $\mathbf{s} = 0.5$ is not in contradiction with the measured cluster sizes indicating $\mathbf{s} = 0.2$, because the variation of cluster shapes and different cluster-substrate interactions for the individual clusters may lead to an additional statistical broadening. However, one should not overemphasize such rather subtle differences between experiment and calculation because of the simplifications included in the semi-classical basis of the model describing the dynamic final state effect.

But even if the parameters describing the dynamic final state effect can not be obtained quantitatively, this effect has to be taken into account for all systems of metal clusters weakly coupled to a substrate, at least if peak positions are analyzed. The induced shift is of the order of W_{max} and can easily reach values of several 100 meV for small clusters. In

Chapter 9 we will present an explicit example for the correction of the spectral changes induced mainly by the dynamic final state effect in order to extend the access to information about the electronic structure of large Au clusters.

9 Intercomparison of Spectroscopy Results

The use of the two complementary methods UPS and STS permits experimental access to both, the momentum dependent and the spatially dependent density of states. In this section the interconnection of the measurements will be discussed considering as example large gold clusters on HOPG. The focus is on the influence of the surface state confinement within the cluster facets (see Sec.6.1) on the experimental STS and UPS spectra. Especially the question how the discrete levels have to be translated into the rather broad UPS features with very weak dispersion is of interest.

A related system is the reconstructed Au(111) surface [88]. Here the quasi one dimensional $23 \times \sqrt{3}$ reconstruction leads to peaks in the STS spectra, dependent on the lateral position within the 2D unit cell [20,89,90]. These features correspond to band gaps of some meV width in the dispersion perpendicular to the reconstruction stripes under the influence of a periodic effective potential acting on the sp-electrons of the surface state. This potential can be modeled by an extended Kronig-Penney model which reproduces the measured STS curves quite well [20]. The effect of the surface reconstruction on the density of states, i.e., the formation of band gaps, should also be detectable in UPS. Reviewing the angle resolved UPS measurements of the bulk Au(111) surface (Fig. 34), such discontinuities are not observable. At significantly increased energetic and angular resolution, however, some influences of the reconstruction potential on the dispersion have been found [91]. The reconstruction induced features are strongly attenuated due to the averaging over three different domains, giving rise to additional contributions from the direction perpendicular to the reconstruction stripes, where the electrons retain their free particle properties. In the case of gold clusters on graphite the “gaps” between the discrete surface state levels are at least ten times larger than the gaps in the dispersion for the Au(111) reconstruction. In addition there is no contribution from other directions in contrast to the Au(111) surface. Hence the discrete electronic structure should be resolvable with our UPS apparatus. However, the cluster size distribution and the dynamic final state effect (see Chapter 8) result in an additional broadening of the features. In this section these contributions are analyzed in detail which allows a self-contained and complete view of the confined surface state on the top facets of large gold clusters on graphite.

9.1 Angle Resolved Photoemission Study

In order to investigate the effect of the surface state on the facets of large gold clusters we prepared a sample optimized for the low temperature photoemission experiment. The Au evaporation was done in a single step and the UPS measurement was subsequently carried out without STM investigations in between. Since the surface state is very sensitive to contamination, special care was taken to assure clean UHV conditions. The gold evaporation was performed at $T = 350^\circ\text{C}$ and the subsequent UPS measurements were done at $T = 50\text{ K}$. The temperature was not set below 50 K in order to avoid the increasing contamination rate of the sample surface at lower temperatures. The Au exposure for this new sample F was about $\Gamma_{\text{evap}} = 1.0\text{ ML}$ which is comparable to samples C and D. Consequently the UPS d-band structure in Fig. 58 is also very similar to that in Fig. 20b.

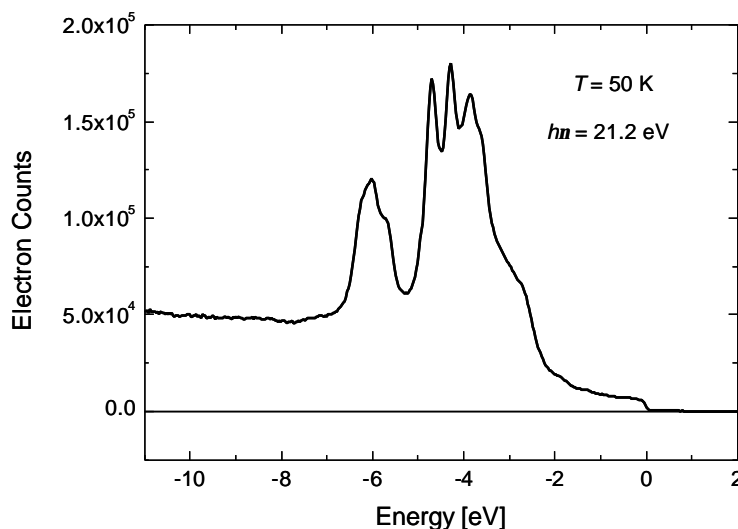


Fig. 58. Normal emission UPS data of the d-band range of sample F after subtraction of the HOPG background signal. In analogy to samples C (cf. Fig. 20b) and D (not shown) the typical structure of the Au(111) surface occurs.

Angle resolved photoelectron spectra with an angular resolution of about $\Delta\Theta \approx 1^\circ$ were taken for the energy region near the Fermi level. In Fig. 59a the raw data are plotted for different emission angles with respect to the surface normal vector. The angle between the helium lamp and the normal emission direction of the analyzer is 45° . The emission angles in Fig. 59a range from $\Theta = -7^\circ$ (towards the He lamp) to $\Theta = +5^\circ$ (in the opposite direction). The uncertainty of the absolute angular scale is about $\pm 1^\circ$ due to a possible

misalignment of the sample. The relative angles, i.e., the angular distances between two spectra is exact within $\pm 0.2^\circ$. The spectra exhibit two main features: First, at normal emission a peak arises at $E \approx -530$ meV similar to the spectra of Fig. 35. This peak shows an asymmetric broadening and an intensity decrease with varying emission angle, as well as some remnants of the surface state dispersion at higher k_{\parallel} . The second feature is the Fermi edge, which is distorted and shifted towards lower energies compared to the bulk Fermi edge. The shape change can be related to electron-hole interactions during the photoemission process. Within the dynamic final state effect (see Chapter 8) the spectra $d(E)$ result from a convolution of the intrinsic (potentially k_{\parallel} resolved) density of states $f(E)$ with a function $P(W)$ representing a probability distribution of energetic shifts. In addition broadening effects like the finite analyzer resolution have to be taken into account, which are combined in the instrument function $u(E)$. All entire broadening and shifting effects can be summarized by a blurring function $g(E)$:

$$d(E) = (P \otimes u) \otimes f \equiv g \otimes f = \int_{-\infty}^{+\infty} \left(\int_{-\infty}^{+\infty} P(W) u(E' - W) dW \right) f(E - E') dE', \quad (36)$$

where \otimes denotes the convolution. The convolution is applied on both, the background intensity with the Fermi edge induced by bulk Au sp-electrons, and the signal from the surface state on the cluster facets. Hence the functions $f(E)$ and $d(E)$ consist of contributions from the bulk (3D) and the surface (2D) electronic structure:

$$d(E) = d_{2D}(E) + d_{3D}(E) \quad \text{and} \quad f(E) = f_{2D}(E) + f_{3D}(E). \quad (37)$$

In order to extract the surface state contribution, which will be the focus of this section, we subtract from each spectrum the data at $\Theta = +5^\circ$, where no remaining surface state signal is detectable. The resulting surface state intensities $d_{2D}(E)$ are plotted in Fig. 59b, and they form the basis of the further discussion.

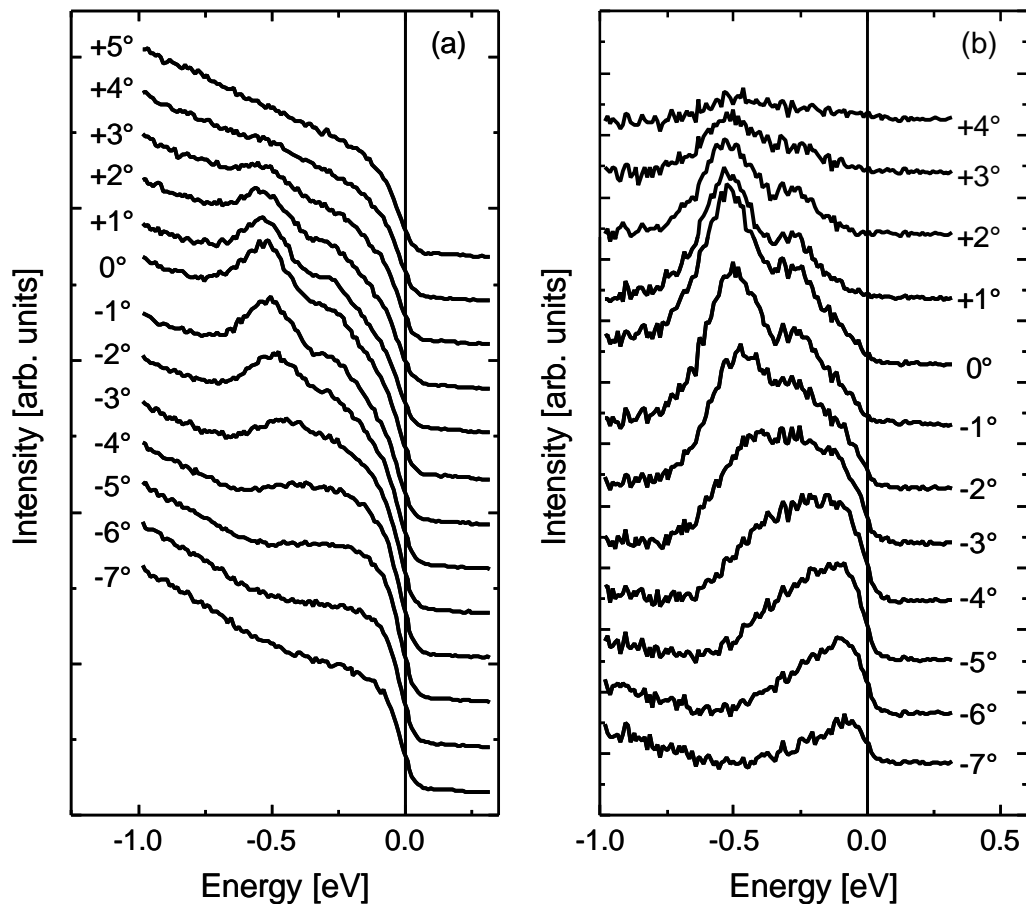


Fig. 59. Angle resolved UPS data of sample F ($T = 50$ K, $\hbar\omega = 21.2$ eV). The emission angles with respect to the surface normal are given next to the respective curves. The spectra are shifted vertically for clarity.
 (a) The raw data show the peak caused by the surface state (cf. Fig. 35).
 (b) Spectra after subtraction of the data at $\Theta = +5^\circ$.

In the background subtracted data the asymmetry mentioned already in Sec. 6.1.2 is even more striking: Whereas for positive angles (i.e., in the direction off the He lamp) the intensity essentially disappears quickly without a noticeable dispersion, in the other direction towards the lamp the main contribution to the overall intensity shifts to higher energies with slowly decreasing signal, vanishing at angles $\Theta < -7^\circ$. The only asymmetry of the experimental setup with respect to the emission angle is given by the incident angle of the photons: for negative values of Θ the incident angle approaches the surface normal direction. This points to an influence of either the photon wave vector parallel to the surface or the polarization of the light. Since the photon wave vector is only about 0.01 \AA^{-1} , the photon momentum appears to be negligible and the polarization effect should be taken into account. Similar effects have been observed in photoelectron spectra of the Cu(111) surface using p-polarized light [92], and they have been attributed to a varying momentum

matrix element depending on the incident angle. However, considering the small incident angle variation of $\approx 10^\circ$ here, the relative effect in our case is much larger than in Ref. [92] though we do not use polarized photons. The detailed origin of the asymmetry effect has to be investigated by varying the incident angle but this is not provided by our apparatus. Another possibility is to use a different photon energy (e.g. ArI radiation) which changes the momentum k_{\parallel} at the same emission angle. This could give hints about the origin of the effect and will be the topic of future experiments.

We now turn to the analysis of the surface state peak shapes in Fig. 59b. The key question is how the observed spectra fit to the expected DOS for the confined surface states of an ensemble of faceted Au clusters. The effects leading to a peak broadening are of special interest, which are the finite angular and energetic resolution of the analyzer, the dynamic final state effect and the inhomogeneous cluster ensemble, i.e. the influence of a distribution of cluster heights and facet areas. As already mentioned in Sec. 6.1.2 the finite angular resolution is negligible here because of the weak dispersion and the broad structures. We thus concentrate on the latter two effects.

Whereas the first peak, originating from the $n = 1$ mode in the hexagonal “particle-in-a-box” model (cf. Sec. 6.1.1), is clearly visible in normal emission, already the second peak can only be identified as a shoulder in the tail of the first one. A main contribution to the spectral broadening is induced by the function $g(E)$ in Eq. 36. The inversion of the convolution, i.e. the deconvolution of the data, should allow to extract the intrinsic electronic structure of the cluster sample. The only remaining effect would be the inhomogeneous broadening. The deconvolution is done with the method described in Appendix 11.2. Necessary inputs are the experimental spectrum $d(E)$, its error $\mathbf{s}_d(E)$, and the convolution function $g(E)$. The question now is: what is the correct $g(E)$ which describes the deviation of the data from the intrinsic electronic structure of the cluster ensemble? The idea is to extract $g(E)$ from data which are not influenced by the Shockley surface state and where the intrinsic structure is well known. In other words, the linear nature of the convolution allows to extract $g(E)$ from the 3D part of the spectra and then apply it on the 2D contribution by a deconvolution. For this purpose we choose the ARUPS spectrum at $\Theta = +5^\circ$, containing no noticeable contribution of the surface state, i.e., we assume $d_{2D}(E) = f_{2D}(E) = 0$ for this angle. The spectra shown in Fig. 59a still contain the graphite signal. This background was measured before the metal evaporation with identical analyzer and photon source parameters and is now subtracted because the

dynamic final state effect, which is included in $g(E)$, does not have an effect on the HOPG spectrum. In addition a small linear background is subtracted in order to set the intensity above the Fermi level (probably induced by satellites in the HeI radiation) to zero. The processed spectrum $d_{3D}(E)$ is shown in Fig. 60 (dotted curve).

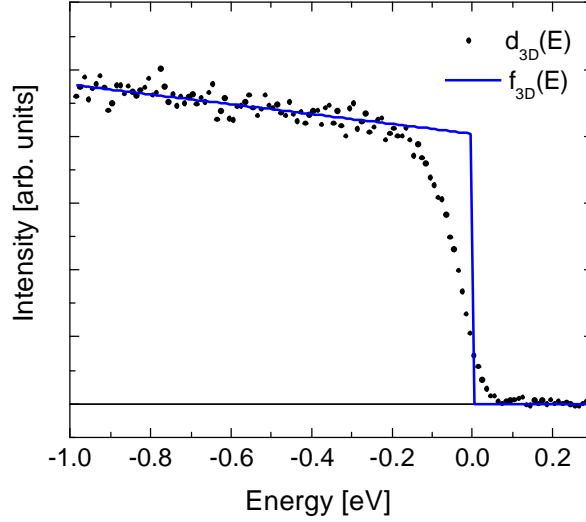


Fig. 60. Background corrected UPS spectrum at $\Theta = +5^\circ$ (dots) and the intrinsic model function (solid line) consisting of a straight line multiplied by a step function.

For large, faceted Au clusters the electronic structure is already close to the bulk limit (cf. Sec. 5.2). Hence, for the intrinsic function $f_{3D}(E)$ we assume a step function multiplied by a straight line. Since the sample temperature was $T \approx 50$ K, the thermal broadening of the Fermi function ($kT \approx 2.8$ meV) can be neglected compared to the smooth behavior of the measured curve (cf. Fig. 60). The straight line represents the first order fit to the density of states below the Fermi level and it fits the low energy part of the UPS result very well (see Fig. 60, solid line). The two curves of Fig. 60 are related via a convolution with the required $g(E)$:

$$d_{3D}(E) = g(E) \otimes f_{3D}(E). \quad (38)$$

By applying a deconvolution of the two step-like functions we are now able to extract $g(E)$. For this purpose a method different from the mentioned AK-MEM is applicable because of the simple form of the intrinsic function $f_{3D}(E)$. The ‘‘Edge Deconvolution’’ procedure is presented in detail in Appendix 11.3. The key idea is to transfer the deconvolution with a step function, which is essentially the derivative of the original data,

to the function $f_{3D}(E)$ which is extended by a straight line. Subsequent to the deconvolution the experimental spectrum is smoothed using the AK-MEM technique (see Appendix 11.2.5) in order to reduce the noise. The resulting blurring function $g(E)$ as shown in Fig. 61 exhibits a clear asymmetry with a tail towards negative energies. The effect on the UPS data besides the broadening is a shift to lower energies in the order of some 10 meV. Therefore the subsequent convolution is not only expected to enhance the peak intensities, but it also corrects the energetic positions. Above the Fermi edge a few wiggles are visible due to the low signal-to-noise ratio of the underlying data in this region and due to numerical reasons behind the sharp edge of the peak (“ringing” effects). But the amplitude of these oscillations is negligible compared to the main peak and the effect on the deconvoluted UPS spectra will be marginal.

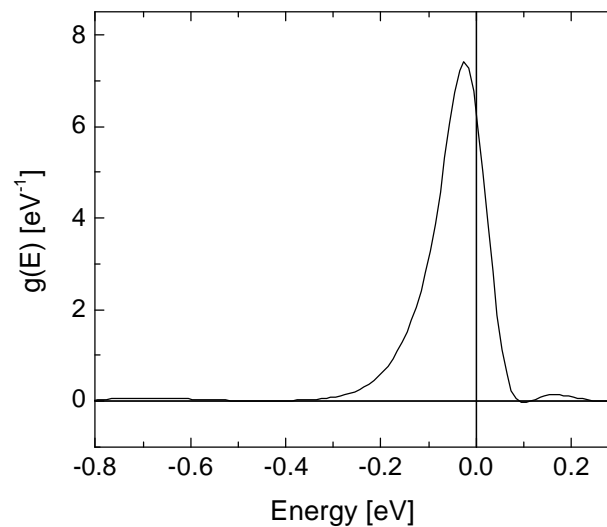


Fig. 61. Deconvolution result of the two functions of Fig. 60 using the “Edge Deconvolution” technique described in Appendix 11.3. The plot represents the smoothed result (see text).

The next step is to deconvolute the experimental data of Fig. 59b with $g(E)$, yielding $f_{2D}(E)$. The complete procedure is analogous to the determination of an apparatus function from experimental data (e.g. the elastic line in a scattering experiment) and then using it for the deconvolution of the spectra [87]. In Fig. 62 the maximum posterior (MAP) result for the normal emission spectrum ($\Theta = 0^\circ$) is shown (cf. Appendix 11.2.3). The displayed confidence region is the pointwise standard deviation of the posterior probability cloud in Gaussian approximation. It gives a rough estimate of the reliability of the

reconstruction $f_{2D}(E)$, but as pointed out in Appendix 11.2.3 it often overestimates the actual uncertainty.

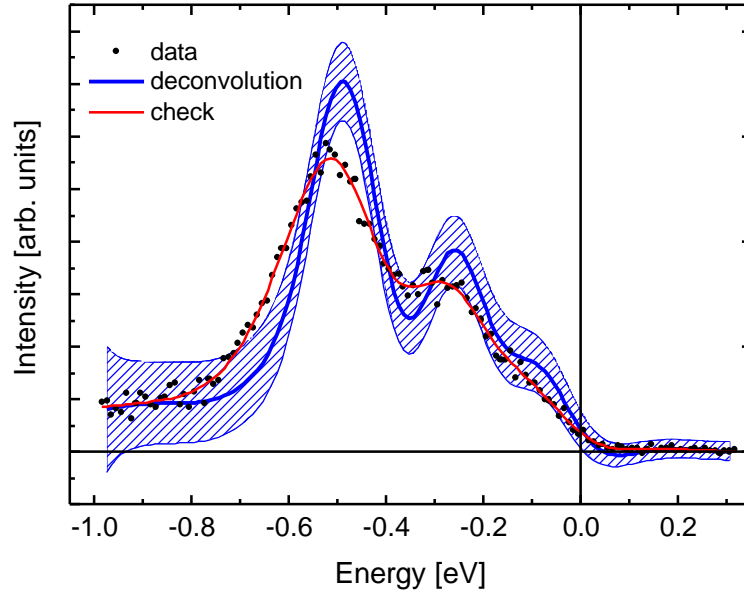


Fig. 62. Maximum posterior (MAP) result (thick line) of the AK-MEM deconvolution of the normal emission spectrum (dots, cf. Fig. 59b). The hatched area represents the confidence interval around the reconstruction $f_{2D}(E)$. The thin line through the data points is the deconvoluted MAP function, convoluted again with $g(E)$ (see Fig. 61). It should fit the data points and therefore serves as an additional check for the reliability of the MAP result.

Clearly observable is the energetic upward shift of the first peak by about 40 meV, located now at $E_1 \approx -490$ meV, and the emergence of a second peak at about $E_2 \approx -260$ meV. The little shoulder near the Fermi level is completely covered by the confidence interval and can not be taken seriously at this point. The asymmetry of the first peak is significantly reduced after the deconvolution which is most obvious at its low energy tail.

The deconvolution procedure can be applied on all angle resolved spectra using the same $g(E)$. The results for the angle range $-7^\circ \leq \Theta \leq 4^\circ$ are summarized in Fig. 63. Three peaks are distinguishable, reaching their maximum intensity at different emission angles.

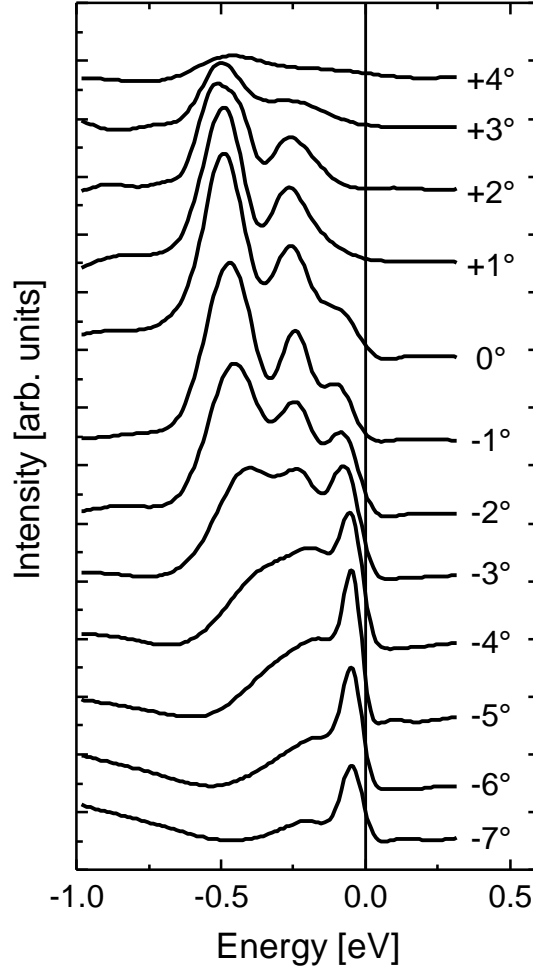


Fig. 63. MAP results $f_{2D}(E)$ for the deconvolution of all angle resolved UPS spectra of Fig. 59b. Note the completely different behavior of the angular dependence compared to the bulk Au(111) surface state (Fig. 34).

From the STS analysis of confined surface states on the cluster facets (see Sec. 6.1.1) we expect that the peaks in $f_{2D}(E)$ correspond to discrete modes within the hexagonal “particle-in-a-box” model. With regard to Eq. 8 the energetic distance between the first two peaks would roughly fit to facet areas around $\Omega \approx 20 \text{ nm}^2$, if we assign them to the $n=1$ and $n=2$ state, respectively. More detailed information about the cluster geometry is provided by STM measurements and is the topic of Sec. 9.2.

Comparing the deconvoluted spectra of Fig. 63 with the bulk Au(111) surface state dispersion in Fig. 34, it is striking that even at $\Theta = 0$ additional peaks for $n > 1$ are visible. Taking into account the parabolic dispersion relation, the respective peak energies E_n correspond to momenta k_{\parallel} which are not within the angular acceptance range of the

electron analyzer. Moreover, at $\Theta = -7^\circ$ there is still a considerable signal near the Fermi edge. In the case of the free surface state dispersion the corresponding energies are located far beyond the Fermi level (cf. Fig. 64), even if the vertical shift due to the finite cluster height is taken into account (see Eq. 9). Two different possible reasons for these effects are considered in the following. From the analysis of the normal vectors of the facet areas with respect to the substrate surface we can identify a facet tilt of some clusters. Although for a few clusters we measured misalignments with angles up to $\pm 3^\circ$, the average facet tilt is found to be well below $\pm 1^\circ$, which would not be enough to explain the occurrence of the second peak in the normal emission photoelectron spectrum. The misalignment could also be induced by the mosaic spread of the HOPG substrate. This spread is specified to be about 0.4° (half maximum height peak width of the Cu-K α rocking curve) for our samples and therefore should not give a significant contribution. An additional, more intrinsic explanation for the second peak at $\Theta = 0^\circ$ is the fact that the surface state electrons will lose their well defined momentum information when they are confined to a small area according to Heisenberg's uncertainty relation. The order of magnitude of this momentum uncertainty can be estimated considering a particle in a one dimensional potential well of infinite height and the length $L = \sqrt{\Omega}$:

$$\Delta x = \sqrt{\langle x^2 \rangle - \langle x \rangle^2} = \frac{L}{2\sqrt{6p}} \sqrt{2p^2 - \frac{3}{n^2}} \approx \frac{L}{\sqrt{12}}. \quad (39)$$

Applying the uncertainty relation with $\Delta p = \hbar \Delta k$ yields

$$\Delta k \geq \sqrt{\frac{3}{\Omega}}. \quad (40)$$

Inserting the typical facet area $\Omega = 20 \text{ nm}^2$ for sample F (cf. Sec. 9.2) we get $\Delta k \geq 0.039$, which corresponds to an emission angle uncertainty of at least $\Delta\Theta = \pm 1^\circ$. Certainly due to the simplifications introduced by the model this is not valid in a quantitative point of view. But the estimation provides a general limit for the achievable k_{\parallel} resolution given by fundamental quantum mechanical reasons in the case of confined electron states. Furthermore, this effect is at least of the same order of magnitude as other, more experimental reasons like those stated above. In Fig. 64 the different contributions to the angular broadening are summarized. By considering the combination of them, the remaining intensity at $\Theta = -7^\circ$ as well as the emergence of the second peak at $\Theta = 0^\circ$ appears to be plausible.

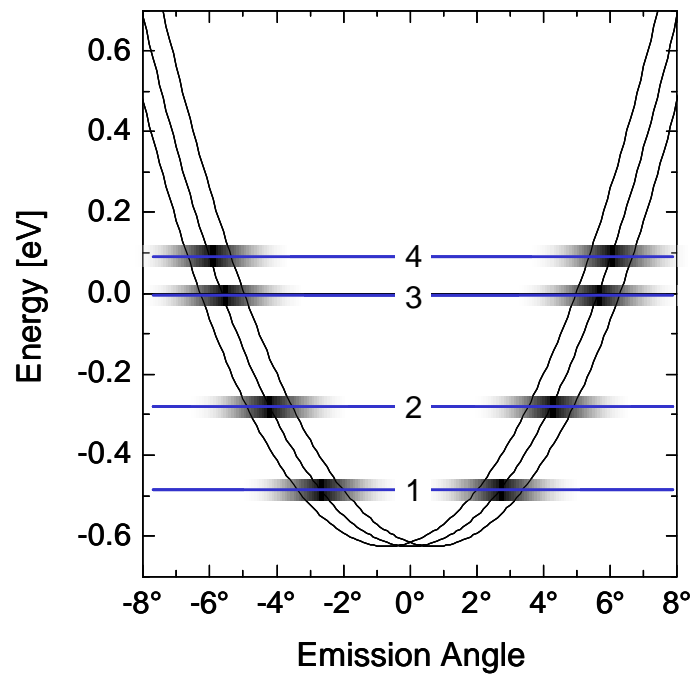


Fig. 64. Schematic representation of the momentum uncertainty of the discrete surface state levels. The eigenenergies (blue horizontal lines) were calculated for a cluster with $h = 2$ nm and $\Omega = 20$ nm², which is a typical cluster size of sample F (see Sec. 9.2). The middle parabola shows the dispersion of a free surface state, shifted 139 meV downward according to Eq. 9. A tilt of the facet surface with respect to the substrate would result in a lateral shift of dispersion, indicated by two additional parabolas. The intrinsic momentum uncertainty, e.g., due to Heisenberg's uncertainty relation is illustrated by gray areas, representing the corresponding angular broadening.

To get the DOS approximately from the spectra in Fig. 63, we can either sum up all angle resolved curves, or just select a single spectrum around $\Theta = -2^\circ$. The latter case is justified since the momentum uncertainty (or the angle distribution) is large enough to cover nearly the complete relevant angular region in one specific direction of the dispersion. Consequently, both procedures yield very similar curves as can be seen in Fig. 65.

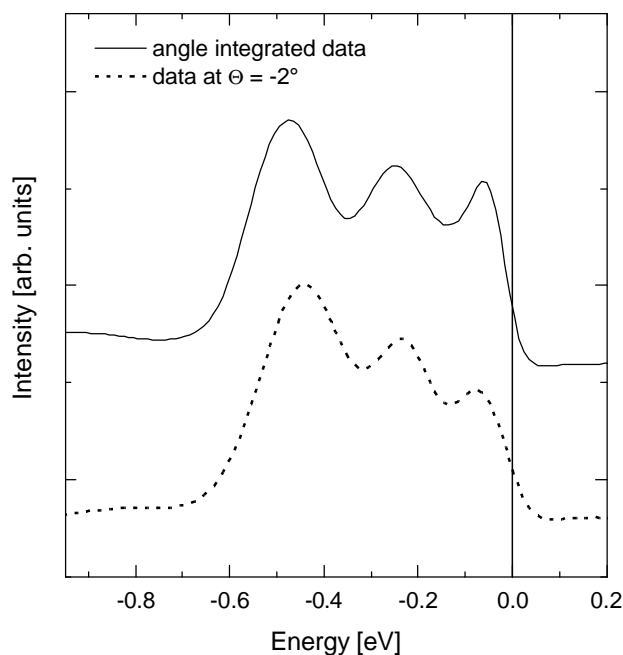


Fig. 65. Comparison of the ARUPS spectrum at $\Theta = -2^\circ$ (lower curve) with the average over all angle resolved spectra (upper curve). The residual peak shift is probably an artifact of the deconvolution since the peak amplitudes approach the size of the confidence interval for $\Theta = -2^\circ$.

In summary we have seen that the angle resolved photoelectron spectra are not only influenced by cluster size or facet angle distributions. Main contributions, i.e., a blurring and a shift of spectral features, originate from fundamental properties of the cluster-surface interaction and its effect on the photoemission process for small particles. However, the information about the quantization of the surface state is not lost. Utilizing deconvolution techniques, it was possible to resolve the discrete levels. In the following sections the DOS is derived using STM and STS information in order to compare the two different methods UPS and STS on a quantitative level.

9.2 Sample Characterization

After finishing the photoelectron spectroscopy, the sample has been transferred into the STM. The images (see Fig. 66a) again reveal flat, nearly hexagonal facets similar to samples C and D. A few single adsorbates on the cluster facets are visible, probably due to the prior UPS experiment. Some of the clusters are located at large pits with a depth of more than one monolayer which results in an inaccurate height determination. Since in this section the absolute height will play an important role for the comparison of STS and UPS

results, we do not include these clusters in the further discussion. Nevertheless, due to the similar effective capture radius (cf. Sec. 7.4) as for the clusters grown in small pits or step edges, the size is not expected to differ significantly. The measured heights and facet areas of 68 clusters are summarized in Fig. 66b.

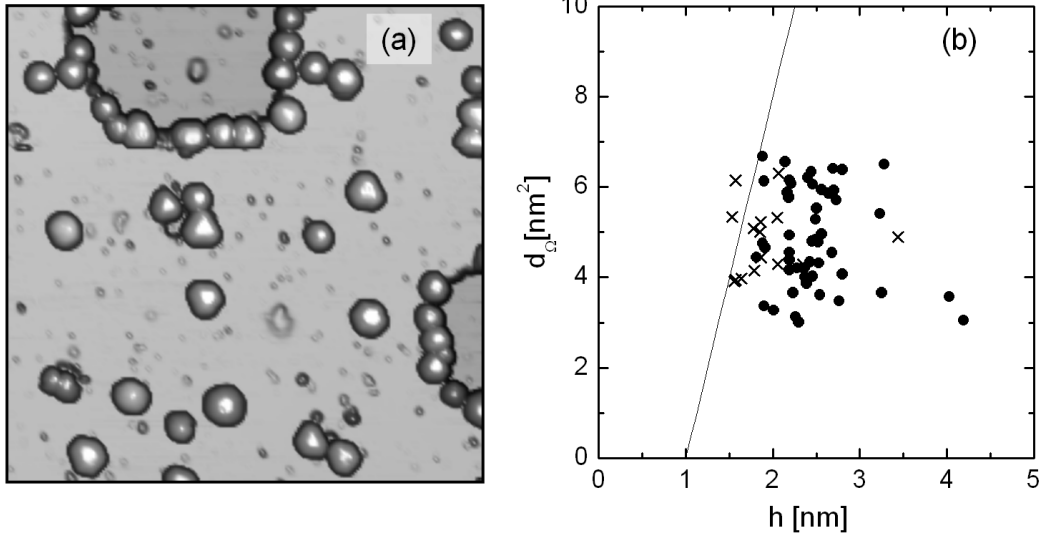


Fig. 66. (a) STM image ($150 \text{ nm} \times 150 \text{ nm}$) of sample F. The two large pits in the upper and in the right region are two monolayers deep. (b) Measured cluster heights and facet diameters for 68 Au clusters. The straight line is taken from Fig. 22 and gives a lower limit for the observed cluster heights in dependence on the facet diameter. The crosses indicate clusters grown in pits with a depth of more than 1 ML, therefore their height, measured with respect to the upper plane of the HOPG surface, is underestimated.

From the height distribution in Fig. 67 we deduce the mean cluster height $\langle h \rangle = 2.5 \text{ nm}$ with a standard deviation of $s_h = 0.5 \text{ nm}$. The black line represents a fit of a log-normal distribution

$$P(h) dh = \frac{1}{\sqrt{2\pi s_h^2}} \frac{1}{x} \exp\left(-\frac{1}{2s_h^2} \left(\ln \frac{h}{\langle h \rangle} + \frac{s_h^2}{2}\right)^2\right) dh, \quad (41)$$

which is used here instead of a Gaussian in order to avoid an unphysical step at $h = 0$ for broad distributions. The gap voltage for the height determination was set to $V \approx 2.5 \text{ V}$ for all topographic STM images which leads to a slightly underestimated height (cf. Sec. 2.1). Since for the determination of the parameters in Eq. 9 a similar voltage was used, this systematic error essentially cancels out.

The measured areas of the (111) top facets for the clusters of sample F are plotted in Fig. 67b.

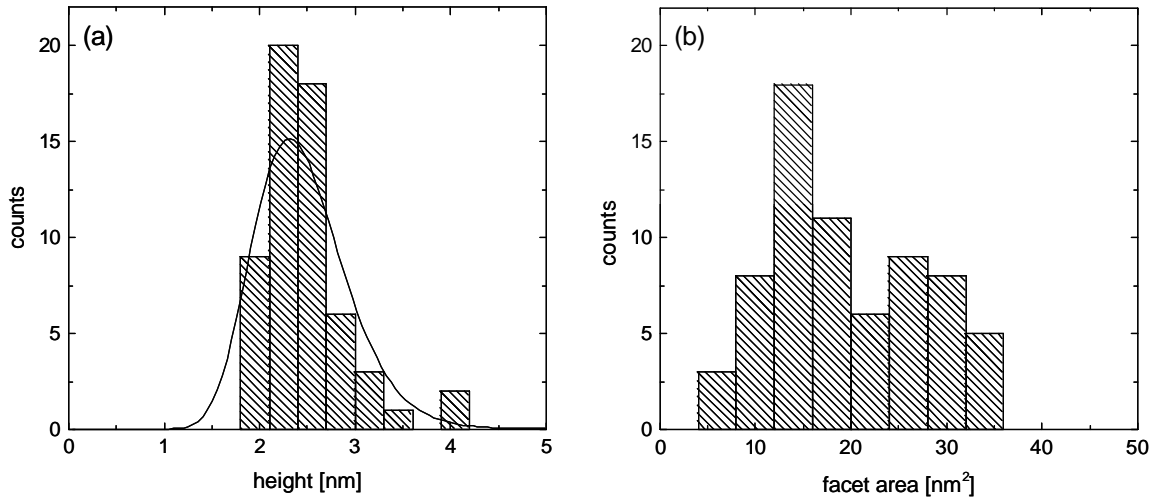


Fig. 67. (a) Cluster heights and (b) facet areas for sample F determined as described in Sec. 5.2. The black line in Fig. 67a represents a log-normal fit to the histogram with $\langle h \rangle = 2.5$ nm and $s_h = 0.5$ nm .

9.3 Simulation

Knowing the morphology of each cluster, it is now possible to calculate the electronic structure of the confined Shockley surface state on the top facets using Eq. 8 and Eq. 9. With this we get a level spectrum for each cluster, and by summing them up it should in principle be possible to simulate the expected angle integrated UPS spectrum. The calculated energy levels for sample F are shown in Fig. 68. Difficulties arise due to the low number of measured cluster heights and facet areas: calculating the density of states (e.g. by convolution with a Lorentzian), the statistical level bunching induces artificial features which are undistinguishable from true peaks arising by averaging over several 10^9 clusters like in the UPS experiment. For this reason we assume log-normal distributions for both, the height distribution as well as the facet areas. For the simulation the two quantities are treated independently since no significant correlation is identifiable in Fig. 66b. Hence the total probability density function $P(h, \Omega)$ may be written as a product of the distributions for h and Ω .

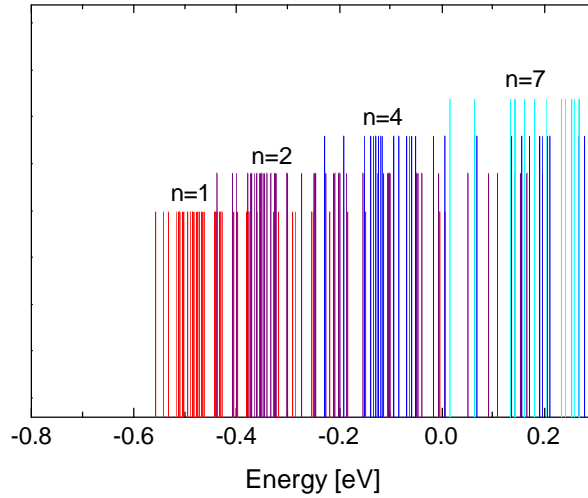


Fig. 68. Calculated energy levels with $n = 1, 2, 4, 7$ (red short lines to blue long lines) for the measured clusters in Fig. 66b. Note the statistically induced level bunching and vacancies for certain energy ranges.

From the measured cluster height distribution we use the parameters deduced from the log-normal fit in Fig. 67a. Though the number of counts is rather low, and therefore the deduced values are not very exact, we do not expect a significant influence on the calculated DOS. The different cluster heights result essentially in a constant broadening of the spectra via the onset energies E_0 , and the mean height determines an overall shift. In contrast the facet areas Ω sensitively affect the peak positions: a change of 5 nm^2 (compare Fig. 67) results in a shift of more than 100 meV for levels near the Fermi energy, which is already of the order of expected level distances. Therefore especially the width of the distribution decides whether discrete peaks are still observable in the simulated DOS. As a starting point we choose a log-normal distribution equivalent to Eq. 41 for Ω with an average value of $\langle \Omega \rangle = 19.5 \text{ nm}^2$ as determined from the measured facet areas, and treat the width \mathbf{s}_Ω as a free fit parameter. The log-normal distribution with the best fit value $\hat{\mathbf{S}}_\Omega$ can then be compared with the measured distribution in Fig. 67b.

The simulation is performed by generating a sample of m pairs of log-normal distributed random numbers, representing m different clusters with height h_i and facet area Ω_i . Typically $m = 10^5$ clusters are generated, which is enough to avoid visible statistical noise. For each cluster i the first five energy levels $E_{i,n}$ are determined using

Eq. 8 and Eq. 9. The line shape of an individual energy level $E_{i,n}$ is assumed to be Lorentzian, thus the DOS is calculated using

$$D(E) \propto \sum_{i=1}^m \sum_n a_{i,n} \Gamma_{i,n} \left((E - E_{i,n})^2 + \left(\frac{\Gamma_{i,n}}{2} \right)^2 \right)^{-1} ; \quad n = 1, 2, 4, 7, 10, \quad (42)$$

where $a_{i,n}$ is a weighting factor. In a first step only levels which could be observed by STS (i.e. high symmetry modes, cf. Sec. 6.1.1) are considered. Higher modes are neglected since their energetic positions are far beyond the Fermi level making them inaccessible for UPS. For the level width we use a constant value of $\Gamma_{i,n} = 20$ meV. It should be emphasized that this width does not necessarily correspond to the inverse lifetime. It is chosen in order to smooth the gaps between the Monte Carlo generated levels, and it roughly gives a lower limit to the minimum peak width in the STS curves. For hexagonal Ag adatom islands on Ag(111) an energy dependent width $\Gamma_{i,n} = 0.2 (E_{i,n} - E_{i,0})$ has been found in the dI/dV spectra [32]. From our STS results of faceted Au clusters on HOPG such a behavior is not evident (cf. Fig. 26 and Fig. 31). However, the final peak width of the simulated DOS will be essentially determined by \mathcal{S}_Ω , rather than by $\Gamma_{i,n}$. In addition, also the choice of the weighting factors is not crucial for the result. Here we assume that the photoemission probability from a specific cluster i is proportional to its facet area, i.e., $a_{i,n} \propto \Omega_i$. We do not include an additional dependence on the quantum number n . This is justified by the fact that for the levels below the Fermi energy the STS curves do not show a clear trend in the peak intensities (cf. Fig. 31). But also other models like $a_{i,n} = \text{const}$ hardly change the shape of the resulting spectrum.

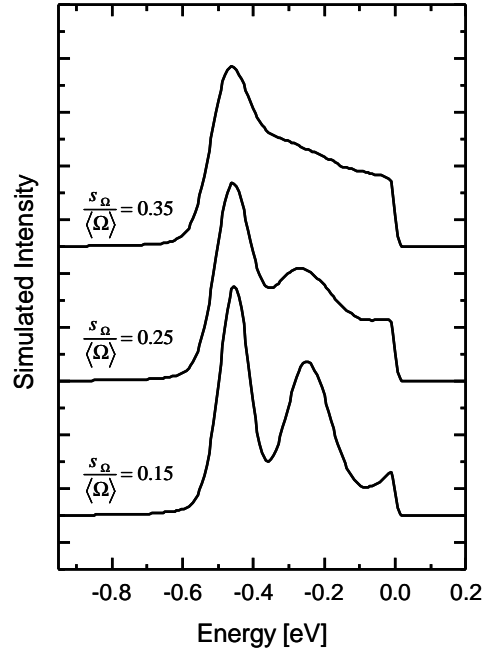


Fig. 69. Simulation results after multiplication with a Fermi function for three different distribution widths s_Ω . For sharp distributions prominent peaks occur, whereas for larger s_Ω the structures disappear. Energy levels taken into account: $n = 1, 2, 4, 7, 10$. The curves are shifted vertically for clarity.

Fig. 69 illustrates the strong influence of the width s_Ω for the facet area distribution on the calculated curves. In order to allow for a better comparison with the experiment, the DOS curves are multiplied by a Fermi-Dirac function for the sample temperature $T = 50$ K. The comparison with the deconvoluted and averaged UPS spectrum in Fig. 65 suggests $s_\Omega \approx 0.25 \cdot \langle \Omega \rangle$, if one focuses on the first two peaks. However, none of the curves in Fig. 69 reproduces the third peak near the Fermi edge. Only for $s_\Omega \leq 0.15 \cdot \langle \Omega \rangle$ a weak maximum becomes visible at the Fermi cutoff, but such a narrow distribution is in contradiction to the histogram in Fig. 67. The discrepancy can be resolved by additionally including the $n = 3$ state in the sum of Eq. 42, which is located near the Fermi level for typical cluster sizes (see Fig. 64). At first glance this state is not identifiable in the STS curves, but we will come to this topic below. Fig. 70 shows the direct comparison of the calculated spectrum using $s_\Omega = 0.25 \cdot \langle \Omega \rangle$ and the levels $n = 1, 2, 3, 4, 7$ with the angle integrated UPS spectrum and the angle resolved spectrum for $\Theta = -2^\circ$, respectively. We further on neglect the modes $n = 5, 6$ because even if they exist (although no structures at the corresponding voltages are observable in the dI/dV curves, cf. Fig. 31), the occurrence below the Fermi level is unlikely due to the exponential behavior in the tails of

the probability distributions for h and Ω . The $n = 7$ mode is included because of its clear signature in the STS spectra (cf. Fig. 26). Though this mode does not play any role for the simulated spectrum in this case, it is taken into account in the simulation program in order to be more flexible for other samples with larger facet areas.

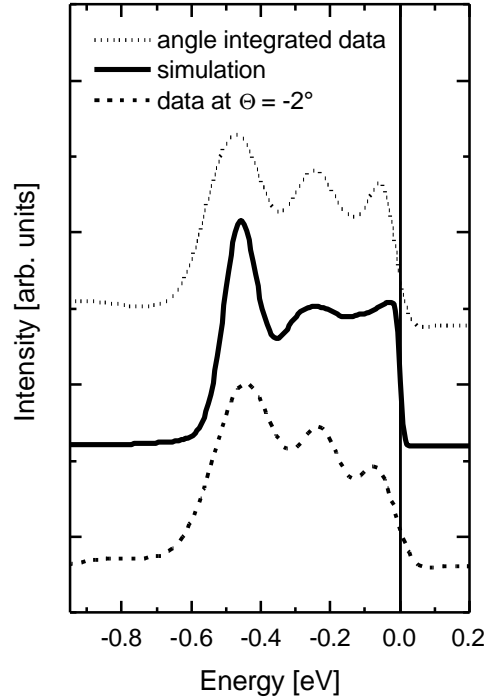


Fig. 70. Comparison of simulated spectra (middle) with angle integrated UPS data (top) and the angular resolved spectrum at $\Theta = -2^\circ$ (bottom), respectively. In contrast to Fig. 69 the confined surface state mode with $n = 3$ is included in the calculation. The width of the facet area distribution is chosen to $\mathbf{s}_\Omega = 0.25 \cdot \langle \Omega \rangle$. The curves are shifted vertically for clarity.

The experimentally observed spectral features and their energetic positions are well reproduced by the simulation. The peak shapes show some deviations, but there exist explanations from the theoretical, as well as from the experimental point of view. First of all the photoelectron count rate is too low to specify the exact shape. This can be seen by the confidence intervals of the deconvoluted spectra (cf. Fig. 62). At least one order of magnitude better statistics is needed for more detailed information. Secondly the model resulting into Eq. 42 is quite simple and experimental evidence which allow to specify the parameters affecting the peak shapes (like, e.g., $a_{i,n}$ and $\Gamma_{i,n}$) is missing so far. Even the facet area distribution is hard to determine experimentally due to the laborious quantification procedure of a large number of facet areas (see Sec. 5.2).

As pointed out above, the log-normal distribution of the facet areas used for the simulation with $\mathbf{s}_\Omega = 0.25 \cdot \langle \Omega \rangle$ can now be compared a posteriori with the experimental histogram, which is done in Fig. 71a. Though the measured areas seem to be spread over a broader range, we would like to stress that the overall width is essentially determined by the largest measured facets. Taking into account the \sqrt{N} uncertainty the applied width of $\mathbf{s}_\Omega = 0.25 \cdot \langle \Omega \rangle$ is not implausible within the statistical limits. In Fig. 71b a set of $m = 10^4$ randomly distributed heights and facet areas as generated by the simulation algorithm is shown in comparison with the measured values. Also in this plot the experimental points are covered by the Monte Carlo sample quite well which justifies the chosen value for \mathbf{s}_Ω a posteriori.

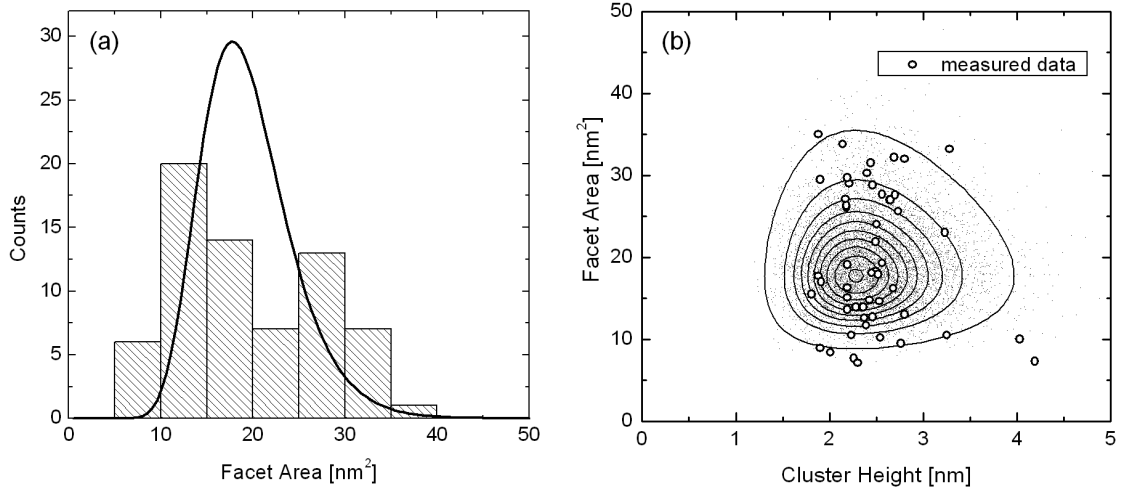


Fig. 71. (a) Probability density function used for the simulation (black line) together with the experimental histogram (cf. Fig. 67b). (b) Monte Carlo set (small dots) of randomly distributed cluster heights and facet areas. The closed curves represent lines of constant values of the corresponding probability density function. For comparison the values as measured by means of STM are added (circles).

As discussed above, the simulations and the comparison with the UPS curves hint to the existence of a contribution from the $n = 3$ mode within the model of a free particle in a hexagonal box. This state could not be identified in the STS maps (cf. Fig. 27) so far. A possible explanation would be that the $n = 3$ signal is suppressed by the intensity arising from the $n = 4$ peak because of the low energetic distance (cf. Table 4) and the low DOS of the $n = 3$ mode near the facet center (cf. inset in Fig. 72). To check this we eliminate

the dI/dV signal from the center region of the facet by subtracting a fraction of the center spectrum from the averaged spectrum (see Fig. 26):

$$(dI/dV)_{\text{outer}} \propto (dI/dV)_{\text{average}} - a \cdot (dI/dV)_{\text{center}}. \quad (43)$$

The weighting factor a is varied until the first peak completely vanishes, here $a = 0.35$. Since the $n = 4$ state also exhibits an intensity maximum in the center, this procedure should stress the outer regions. As shown in Fig. 72 the difference $(dI/dV)_{\text{outer}}$ is still nearly identical to the average curve, except for the first peak and the peak around $V \approx -0.2$ V. Whereas in the averaged spectrum the latter peak exhibits an asymmetry, it now has a symmetric shape and is shifted to a lower energy position, which roughly corresponds to the $n = 3$ state.

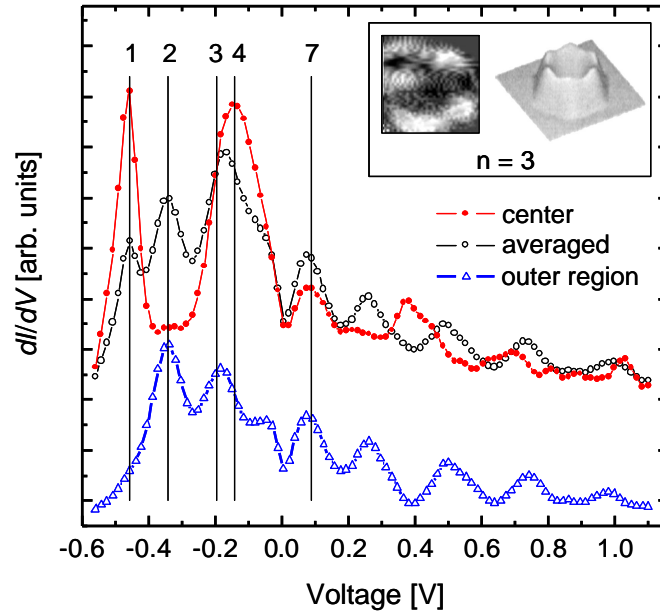


Fig. 72. dI/dV spectra for same cluster as in Fig. 26 ($h = 3.9$ nm, $\Omega = 37$ nm²) measured in the center (red dots) and averaged over the total facet area (black circles). The lower curve (blue triangles) is the weighted difference according to Eq. 43 and represents the LDOS in the outer region of the facet (see text). It is shifted vertically for clarity. The inset shows the weighted difference of the dI/dV maps at $V = -0.148$ V and $V = -0.199$ V (left) which enhances the $n = 3$ mode. On the right the calculated LDOS for the $n = 3$ state (from Ref. [36]) is shown for comparison.

The spatial symmetry of the mode can be checked by subtracting dI/dV maps at the voltages corresponding to the $n = 3, 4$ states from each other. Again a weighting factor is included in order to eliminate the intensity in the center. The result is added in the inset of

Fig. 72 together with the theoretically expected symmetry as presented in Ref. [36]. Consistently, in both cases an enhanced intensity is visible at the corners of the facet. In summary, this analysis allows to draw the conclusion that the $n = 3$ level of the confined surface state probably contributes to the experimental photoelectron spectra. Including this mode to the theoretical simulation we achieve a consistent description of both, the UPS and STS results of large, faceted Au clusters on graphite.

10 Summary and Outlook

Throughout the work the interplay between the morphology and the electronic structure of gold nanoclusters on graphite has been demonstrated. The knowledge of the morphology is a necessary ingredient for the understanding of the experimental spectra. Consequently, the STM and UPS measurements for a large range of cluster sizes have been analyzed thoroughly in Chapter 5. As shown in Sec. 5.2 large clusters consisting of several thousand atoms exhibit flat top facets parallel to the substrate surface. With the STM data a geometric model has been developed which allowed the parameterization of each cluster by its height h and its facet area Ω . Smaller clusters without a measurable facet have been described with a simpler model, taking into account a constant width-to-height ratio of $\langle d \rangle / \langle h \rangle \approx 1.4$ (cf. Sec. 5.1). The different morphology compared to large Au clusters indicates a transition from a three-dimensional towards a predominant two-dimensional growth with increasing cluster size. These investigations formed the basis of the subsequent analysis of the electronic structure and the growth process.

The combination of the two complementary spectroscopy methods STS and UPS is an efficient tool for studying the electronic properties of nanostructures on surfaces. As a first step the spatial dependent dI/dV spectra on top of the faceted Au clusters have been analyzed in Sec. 6.1. We have shown that the pronounced patterns of standing waves in the dI/dV maps are caused by a Shockley surface state confined to the facet area. By comparing the energetic positions of the modes for different clusters we were able to deduce a formula which allows to predict all energy levels of cluster with given height and facet area. The confined surface state is also evident in angle resolved photoelectron spectra which average over a large amount of clusters (Sec. 6.1.2).

For smaller, non-faceted clusters the shape is less well defined and the interpretation of the dI/dV spectra is complex. In Sec. 6.2 we have presented a data set for a large number of single clusters with different sizes. Though the features of the dI/dV curves are not analyzed on a quantitative level, we have shown the main effects involved in the tunneling spectra, i.e., a quantized electron structure, electronic shell effects, and single charge transport effects.

The knowledge of the growth mechanism is advantageous for the targeted preparation of clusters with well-defined morphology. In Chapter 7 the combination of STM and UPS has been used for the investigation of different aspects of the cluster growth. We have shown that the pits serve as condensation centers (cf. Sec. 7.1) and that the cluster centers

are located at the pit edges, leading to clusters partially grown on the upper and on the lower plane of the graphite step (cf. Sec. 7.2). The evolution of the electronic structure in the photoelectron spectra can be used for the investigation of the cluster growth process starting from small, non-faceted clusters up to large clusters with pronounced top facets (see Sec. 7.3). The confined Shockley surface state discussed in Sec. 6.1 emerges in coincidence with the detailed d-band structure of the (111) facets, additionally pointing to the mentioned morphology change. The quantitative treatment of the photoelectron signal of the d-bands is not straightforward. However, a careful analysis gives evidence for an increasing condensation coefficient during the growth. Furthermore, the integrated intensity is in excellent agreement with the projected area calculated using a simple geometric model based on STM data, particularly in the limit of large clusters, where the finite electron escape depth becomes less important. The comparison of the UPS and STM results with a simple kinetic growth model in Sec. 7.4 confirms the assumed growth mechanism and the obtained condensation coefficients.

The analysis of photoelectron spectra of clusters coupled weakly to the substrate requires the consideration of the dynamic final state effect (see Chapter 8). It is related to the dynamics of the Coulomb interaction between the photoelectron and the charged cluster and leads to an asymmetric broadening of spectral features. This effect has been previously demonstrated for UPS measurements of low temperature Fermi edges but here its influence could also be extracted for room temperature UPS data using sophisticated deconvolution techniques. The explicit dependence on the photoelectron velocity has been checked by combined UPS and XPS experiments utilizing the large difference of the respective photon energies.

Finally, all previous investigations and results have been combined in Chapter 9. For the new sample we have chosen optimized preparation parameters using the results of the former samples. We could observe the discrete surface state levels also in the angle resolved photoelectron spectra and the asymmetric broadening due to the dynamic final state effect has been corrected by deconvolution based completely on experimental data. The cluster morphology has been determined by STM measurements of the same sample. With this information it was possible to calculate the average energetic positions of the quantized surface-state levels for the total sample. The consideration of additional eigenstates which could not be resolved before in the STS data revealed an excellent agreement with angle-integrated photoelectron spectra.

In summary we achieved a framework of STM, STS, and UPS results, which allows a complete and self-contained view of the electronic structure of Au clusters on graphite near the Fermi level. Only for small, non-faceted clusters the direct comparison of tunneling spectroscopy on individual clusters and photoemission results has not been successful because the UPS data consist of an average over several 10^9 different clusters. With an electronic structure which shows a very strong change with varying cluster size this smears out all sharp spectral features.

Two different methods are feasible to overcome this problem. The first one is the photoelectron spectroscopy on individual clusters with a Photoemission Electron Microscope (PEEM). Unfortunately it is extremely demanding to combine high lateral resolution with high energy resolution. In addition the signal intensity is very low which requires large signal accumulation times and thus increases contaminations. The second possibility is the mass-selected deposition of free clusters produced in a gas aggregation source. Currently, a magnetron sputter source is being built in cooperation with the University of Freiburg (C. Yin, B. v. Issendorff) which allows to extract clusters with a narrow mass range and deposit them onto nearly arbitrary surfaces under soft landing conditions. The deposition of clusters with different well-defined sizes allows the systematic investigation of finite-size effects for metal clusters on surfaces even for averaging spectroscopic techniques like UPS.

11 Appendix

11.1 UPS Line Shapes for a Finite Angular Resolution

In Sec. 6.1.2 the Shockley surface state of a bulk Au(111) surface has been investigated by UPS. In particular the values for the surface state onset E_0 and the effective mass m^* are needed for the modeling of the confined surface state on the (111) facets of large Au clusters. In a simple analysis one would determine the lowest peak position of the ARUPS spectra, which results in $E_0 = -432$ meV for the spectra of Fig. 34. The inaccuracy of the manipulator angle with respect to the analyzer direction is less than 0.5° and may thus result in a shift of < 5 meV towards higher peak positions. This systematic error can be avoided by a careful adjustment of the surface normal of the sample. Additionally, however, the finite angular resolution of the analyzer affects the peak shape and therefore the position of the peak maximum [93,94]: the limited k_{\parallel} selectivity induces an energetic broadening, particularly for highly dispersive states, such as the Shockley surface state with its low effective mass of $m^* = 0.26 m_e$. In this section we deduce an analytical mathematical expression for the expected line shape. Together with the consideration of the finite lifetime, the Fermi cutoff, and the energetic analyzer resolution it allows to determine E_0 and m^* much more accurately by fitting the theoretical curves to the photoelectron spectra.

The energy dispersion of the surface state can be written as (cf. Chapter 3)

$$E = E_0 + \hbar^2 k_{\parallel}^2 / 2m^* . \quad (44)$$

The wave-vector parallel to the surface is $k_{\parallel} = \sqrt{2mE_{\text{kin}} / \hbar^2} \sin \mathbf{q}$, E_{kin} is the kinetic energy of the photoelectrons after leaving the surface, m is the free electron mass, and \mathbf{q} is the angle of electron emission. In UPS only the parallel part of the k vector can be measured directly (see Sec. 2.3). The finite angular resolution of the electron analyzer applies not only for the angle \mathbf{a} , which we are able to change by rotating the manipulator, but also for the angle \mathbf{b} corresponding to the direction perpendicular to the manipulator axis, which is in our experiment adjusted at zero. We suppose that the distribution of the angles is Gaussian, because the aperture of the analyzer is small. A two-dimensional Gaussian function gives the distribution around the adjusted angles \mathbf{a}_0 and \mathbf{b}_0 :

$$P(\mathbf{a}, \mathbf{b}) = \frac{1}{2p\mathbf{s}_a^2} \exp\left[-\frac{(\mathbf{a} - \mathbf{a}_0)^2 + (\mathbf{b} - \mathbf{b}_0)^2}{2\mathbf{s}_a^2}\right]. \quad (45)$$

In this formula \mathbf{s}_a is the angular resolution of the analyzer, which is in the following assumed to be isotropic ($\mathbf{s}_a = \mathbf{s}_b$). For a realistic comparison between theory and experiment all angles have to be considered. The probability distribution of Eq. 45 can be transformed into an energetic one:

$$P(\mathbf{a}, \mathbf{b}) d\mathbf{a} d\mathbf{b} = P(E) dE. \quad (46)$$

Because for the surface state both angles \mathbf{a}_0 and \mathbf{b}_0 are small and $\mathbf{s}_a \ll 1$, it is $\mathbf{q}^2 = \mathbf{a}^2 + \mathbf{b}^2 \ll 1$ and the energy (Eq. 44) can be approximated as

$$E \approx E_0 + c\mathbf{q}^2 \quad \text{with} \quad c = E_{\text{kin}} \cdot m / m^*. \quad (47)$$

The use of cylinder coordinates ($\mathbf{a} = \mathbf{q} \cos \mathbf{j}$ and $\mathbf{b} = \mathbf{q} \sin \mathbf{j}$) gives:

$$P(E)dE = d\mathbf{q} \cdot \mathbf{q} \int_0^{2p} d\mathbf{j} P(\mathbf{q}, \mathbf{j}) \quad (48)$$

with

$$P(\mathbf{q}, \mathbf{j}) = \frac{1}{2p\mathbf{s}_a^2} \exp\left[-\frac{(\mathbf{q} \cos \mathbf{j} - \mathbf{a}_0)^2 + (\mathbf{q} \sin \mathbf{j} - \mathbf{b}_0)^2}{2\mathbf{s}_a^2}\right]. \quad (49)$$

Now we get for $P(E)dE$,

$$P(E)dE = d\mathbf{q} \cdot \mathbf{q} \frac{1}{2p\mathbf{s}_a^2} \exp\left(-\frac{\mathbf{q}^2 + \mathbf{a}_0^2 + \mathbf{b}_0^2}{2\mathbf{s}_a^2}\right) \times \int_0^{2p} \exp\left(\frac{2\mathbf{q}\mathbf{a}_0 \cos \mathbf{j} + 2\mathbf{q}\mathbf{b}_0 \sin \mathbf{j}}{2\mathbf{s}_a^2}\right) d\mathbf{j}. \quad (50)$$

Solving the integral in Eq. 50 leads to [95]

$$P(E)dE = d\mathbf{q} \cdot \mathbf{q} \cdot \frac{1}{\mathbf{s}_a^2} \exp\left(-\frac{\mathbf{q}^2 + \mathbf{a}_0^2 + \mathbf{b}_0^2}{2\mathbf{s}_a^2}\right) \cdot I_0\left(\frac{\mathbf{q}}{\mathbf{s}_a} \sqrt{\mathbf{a}_0^2 + \mathbf{b}_0^2}\right). \quad (51)$$

In this formula I_0 is the regular modified cylindrical Bessel function of the order zero.

After the substitution of $\mathbf{q} = \sqrt{(E - E_0)/c}$ from Eq. 47 and $E_{\text{kin}}(E) = E + \hbar n - \Phi$, where Φ is the work function, the probability distribution finally transforms to

$$P(E) = \frac{1}{2c\mathbf{s}_a^2} \frac{E_{\text{kin}}(E_0)}{E_{\text{kin}}(E)} \exp\left[-\left(\frac{|E-E_0|}{c} + \mathbf{a}_0^2 + \mathbf{b}_0^2\right) / 2\mathbf{s}_a^2\right] \times I_0\left(\sqrt{\frac{E-E_0}{c}} \cdot \frac{\sqrt{\mathbf{a}_0^2 + \mathbf{b}_0^2}}{\mathbf{s}_a}\right). \quad (52)$$

This function is plotted in Fig. 73 for the two angles $\mathbf{a}_0 = 0^\circ$ and $\mathbf{a}_0 = 3^\circ$, respectively, using the parameters $E_0 = -445$ meV, $m^* = 0.25 m_e$, $\mathbf{b}_0 = 0^\circ$, and $\mathbf{s}_a = 1.5^\circ$ (solid curves). In order to take into account the finite lifetime of the surface state, Eq. 52 has to be convoluted numerically with a Lorentzian. Since only occupied states contribute to the spectra, the result is then multiplied with a Fermi function corresponding to the sample temperature T . Finally a convolution with a Gaussian is performed due to the finite energy resolution of the analyzer. The corresponding curves are additionally shown in Fig. 73 (dashed curves). Note that due to the asymmetric shape of $P(E)$ the peak maximum of the dashed curve for normal emission, i.e. $\mathbf{a}_0 = 0^\circ$, is located about 30 meV above the surface state onset E_0 .

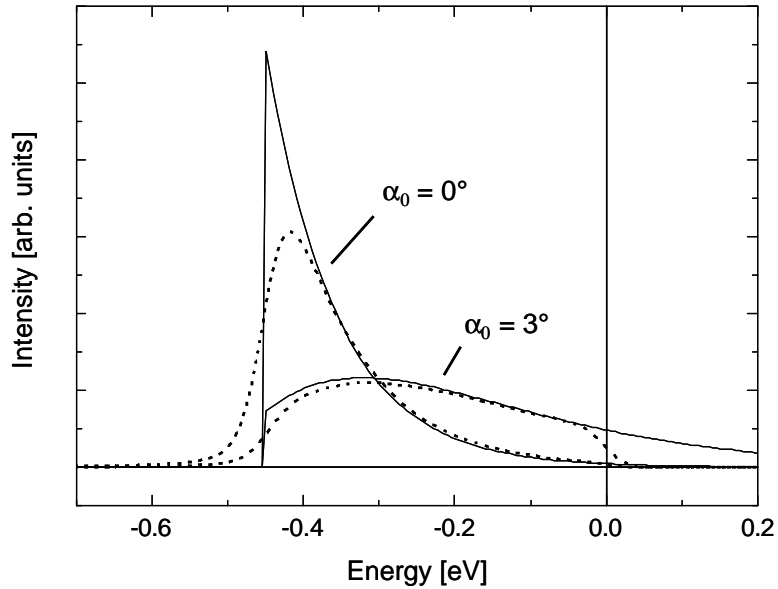


Fig. 73. Solid Lines: $P(E)$ according to Eq. 52 for $\mathbf{a}_0 = 0^\circ$ and $\mathbf{a}_0 = 3^\circ$, respectively. The other parameters are given in the text. Dashed Lines: the same $P(E)$ after the convolution with a Lorentzian ($\Gamma = 20$ meV), multiplication with a Fermi function ($E_F = 0$, $T = 45$ K), and a second convolution with a Gaussian ($\mathbf{s}_{\text{Gauss}} = 20$ meV).

To fit the calculated set of spectra to the experiments we varied the following parameters: the energetic position E_0 , the effective electron mass m^* of the surface state, the start angle $\mathbf{a}_{\text{start}}$, from where the others follow in the same distance (here 1°), the angular resolution \mathbf{s}_a , the width of the Lorentzian Γ , and the energy resolution $\mathbf{s}_{\text{Gauss}}$.

To compare the measured data of the surface state to the calculated, we first have to subtract a background intensity. The background can be induced for example by satellites from the photon source or by signal from defects and it is approximated by a linear function. The structure of the background is assumed to be angle independent for small angles. So we use the zero degree angle to fit a Fermi function multiplied with a linear function in a region without signal from the surface state. In addition a second linear function is subtracted to account for the signal above the Fermi level. This is shown for one example in Fig. 74. With this fit we get the position of the Fermi energy E_F very accurately as well, which is needed to calculate the absolute energetic position of the surface state.

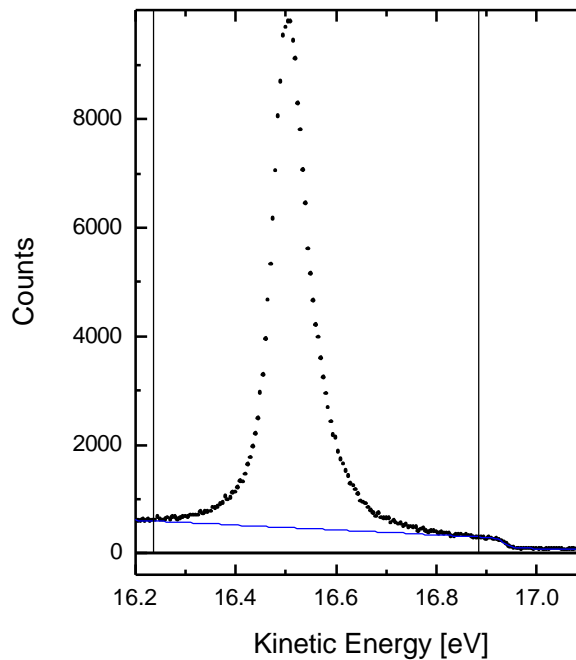


Fig. 74. The dots are the measured photoemission data for the angle nearest to zero (spectrum marked with a thick line in Fig. 34). The blue solid line represents the background fit as described in the text. The region between the vertical lines was excluded for the fit.

For the angle resolved UPS spectra of the Au(111) surface shown in Fig. 34 just one set of parameters as described above is used to fit all spectra for different angles simultaneously. Only a constant factor is adjusted automatically for each curve to match the peak amplitudes. The theoretical model is implemented as a macro within the program “Origin”, where the complete set of calculated spectra is displayed simultaneously together with the experimental data. In this way the optimum set of parameters can be adjusted manually in a few steps. The agreement between the manually fitted theoretical curves and the experiment is almost perfect. The resulting parameters $E_0 = (-445 \pm 5) \text{ meV}$ and $m^* / m_e \approx 0.25 \pm 0.01$ were already given in Sec. 6.1.2. The errors result from the range of fitting parameters which still give a reasonable agreement with the ARUPS curves.

With the fitting routine we are much more sensitive for calculating the energetic position and the effective electron mass for the dispersion relation of the surface state than by simply measuring peak positions. The deduced E_0 is more than 10 meV lower than the value $E_0 = -432 \text{ meV}$ obtained by simply measuring the peak positions (see above). We note that the angular resolution for the spectra of Fig. 34 is $\mathcal{S}_a \approx 0.7^\circ$ (value for best fit), which is the limit of our analyzer. For other, more complicated systems like rare gas layers on Au(111) the angular acceptance is increased in order to obtain higher count rates [20]. For these systems the consideration of the finite angular resolution results in an even larger correction of the onset energy by up to 30 meV.

11.2 Maximum Entropy Deconvolution Techniques

The analysis of measured data $d(x)$ is often made difficult by the influence of the experimental setup. In many cases this influence can be described mathematically by a convolution of the “intrinsic” spectrum $f(x)$ with the apparatus function $a(x)$:

$$d(x) = f(x) \otimes a(x) = \int_{-\infty}^{+\infty} f(y) a(x-y) dy. \quad (53)$$

The quantity of interest is $f(x)$, reflecting the intrinsic physical properties of the system. Commonly, $f(x)$ is determined by convoluting a parameterized model with a measured or assumed apparatus function $a(x)$ and selecting those parameters which result in the best fit to the experimental data. The more interesting way, however, is the direct inversion of Eq. 53, i.e., a deconvolution of the measured spectrum with the (ideally also measured) apparatus function. As shown by example in Sec. 8.2.2 and Sec. 9.1 this procedure can provide an extended insight into the physical properties of various systems. In general the deconvolution requires sophisticated methods due to the unavoidable experimental noise. In particular techniques based on the Maximum Entropy principle have turned out to be extremely successful in the fields of spectroscopy [86,96-98], crystallography [99], astrophysics [100-102], medical physics [96,103,104] and other, partly non-physical applications.

11.2.1 Motivation

A simple ansatz of solving Eq. 53 becomes obvious if the problem is discretized into N data points, resulting in a matrix representation:

$$d_i = \sum_{j=1}^N a_{i-j} f_j. \quad (54)$$

Thus the convolution is equivalent to the matrix multiplication

$$\vec{d} = A \vec{f} \quad \text{with} \quad A_{ij} = a_{i-j}. \quad (55)$$

This rewriting suggests a simple matrix inversion to obtain the intrinsic function \vec{f} :

$$\vec{f} = A^{-1} \vec{d}. \quad (56)$$

Even if the experimental spectrum consists of several hundred data points, the duration of the matrix inversion is below 1s on a standard desktop computer. Furthermore, the solution of Eq. 56 is equivalent to a division in Fourier space, which additionally allows to improve the computation speed significantly using the Fast Fourier Transform (FFT) algorithm [105]. However, the problem arising with this ansatz is the fatal sensibility to experimental noise. This is impressively documented in Ref. [106], starting from an ideal spectrum without any noise (see Fig. 75a). An artificial spectrum (solid line) is generated by convolution of a test (“mock”) function (dotted line) with a Gaussian apparatus function. In Fig. 75b the Fourier deconvolution is applied on the same spectrum, except for the change of the right-hand peak by one count. This “noise” of a relative amplitude of 10^{-6} results in a wildly oscillating curve with much larger amplitudes than the actual signal. In contrast, the Fourier-deconvolution result of the first, unchanged peak matches exactly the mock function.

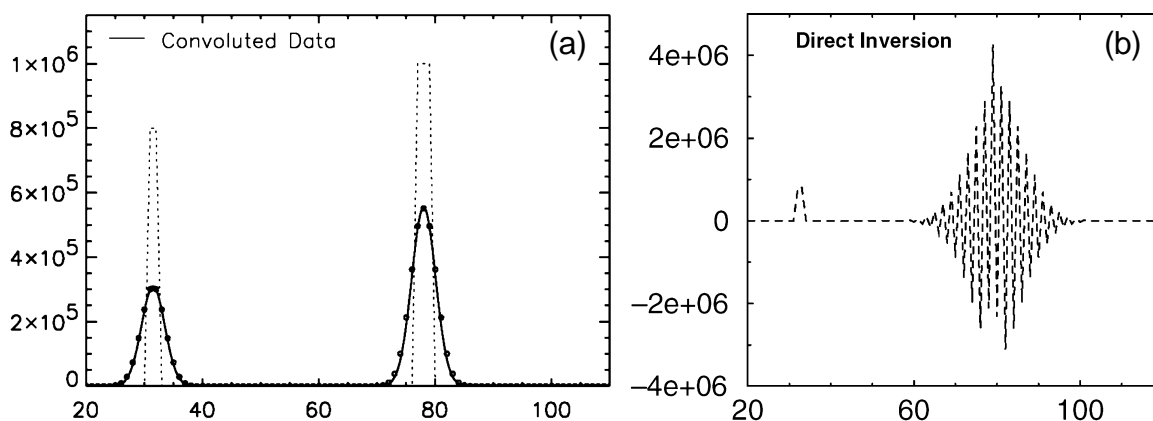


Fig. 75. (a) The initial function (mock spectrum, dashed line) is convoluted with a Gaussian to yield the solid curve.
 (b) Direct inversion result according to Eq. 56 after the removal of one count from the right-hand peak. From Ref. [106].

Some extensions have been made to the simple Fourier method in order to suppress the oscillating behavior. A common procedure is to apply low pass filters, which is particularly convenient in Fourier-space. As a consequence, however, the bandwidth of deconvoluted spectra is accordingly limited, giving rise to a blurred output. Thus the original intention, the “deblurring” of the experimental data is partly destroyed. In practice the appropriate choice of the filter function and the cutoff frequencies is difficult and often spectral

artifacts occur or a resolution enhancement is hardly obtained. Moreover, the result is dependent on these free parameters, reducing the objectivity of the solution.

Ironically, the origin of the strange behavior of the Fourier deconvolution technique is the exact mathematical form of Eq. 56: the Fourier method tries to reproduce the data exactly, *even the statistical noise*, which is obviously unphysical. The phenomenon of noise results in an effective loss of information, turning the deconvolution problem into an ill-conditioned one. Instead of Eq. 55 we have to add the noise \vec{n} :

$$\vec{d} = A\vec{f} + \vec{n}. \quad (57)$$

A correct treatment of the deconvolution problem must include “incorrect” solutions in the sense that it has to allow for results which do not fit the data exactly when being convoluted with the apparatus function. In other words, the statistical nature of the experimental data demands a mathematical description based on statistical principles.

11.2.2 Bayesian Probability Theory

A useful tool for the mathematical description of statistical models is the Bayesian Probability Theory. An extensive and practical introduction can be found in Ref. [107]. Here we summarize the main ingredients for the solution of the deconvolution problem.

The key quantity of this framework is the conditional probability $P(x|y)$ (spoken: “probability of x given y ”). It is the (positive) probability that x is true if we know that y is true. With this definition it is possible to evaluate the joint probability for two variables f and d , i.e., the probability that both of them are true:

$$P(f, d) = P(f | d) P(d). \quad (58)$$

All non-conditional probabilities satisfy the normalization constraint

$$\int_x P(x) dx = 1. \quad (59)$$

The entire probability for d , independent of f , is the sum over the joint probabilities for all possible values of f :

$$P(d) = \int_f P(f, d) df. \quad (60)$$

Another way to write the joint probability (cf. Eq. 58) is

$$P(f, d) = P(d | f) P(f). \quad (61)$$

The combination of Eq. 58 and Eq. 61 yields the relation

$$P(f | d) = \frac{P(d | f) P(f)}{P(d)}, \quad (62)$$

which is often referred to as ‘‘Bayes’ theorem’’. It offers a formal solution of inverse problems, such as the deconvolution of noisy data: if the variables f and d are assigned to an assumed intrinsic function and the measured spectrum, respectively, the probability of f being correct on the assumption that the data are true can be calculated using Eq. 62. A simple procedure would be to search for that f which maximizes $P(f | d)$. The solution of the deconvolution would then be the most probable intrinsic function under the constraint of the given data d . The left part of Eq. 62 is called the ‘‘posterior probability’’, thus the output of the described procedure corresponds to the maximum posterior (MAP) result. Other interpretations are mentioned in Appendix 11.2.3. The remaining task is to assign and calculate the right part of Eq. 62, i.e., the ‘‘likelihood’’ $P(d | f)$, the ‘‘prior probability’’ $P(f)$, and the ‘‘evidence’’ $P(d)$.

11.2.3 Classic Maximum Entropy Method

Starting from Bayes’ theorem (Eq. 62) we are searching for the probability distribution $P(\vec{f} | \vec{d})$, where \vec{f} is a possible discrete intrinsic function and \vec{d} is the measured data set. First we assume that the experimental data are normally distributed around the ideal convolution result $A\vec{f}$ (cf. Eq. 55). For Gaussian noise the probability to observe the entire data set \vec{d} (consisting of N points) for a given \vec{f} is

$$P(\vec{d} | \vec{f}) = \prod_{i=1}^N P(d_i | \vec{f}) = \frac{\exp(-\mathbf{c}^2/2)}{Z_L} \quad (63)$$

$$\text{with } \mathbf{c}^2 = \sum_{i=1}^N \frac{1}{\mathbf{s}_i^2} \left(d_i - \sum_{j=1}^N A_{ij} f_j \right)^2 \quad \text{and} \quad Z_L = (2\mathbf{p})^{N/2} \prod_{i=1}^N \mathbf{s}_i.$$

In a counting experiment the error \mathbf{s}_i is given by $\mathbf{s}_i = \sqrt{d_i}$. In the literature the abbreviation $L = \mathbf{c}^2/2$ is often used for the negative logarithm of the likelihood $P(\vec{d} | \vec{f})$, ignoring the offset due to Z_L .

The evidence $P(\vec{d})$ represents a normalization constant, which can be obtained by a N dimensional integration over the joint probability cloud (cf. Eq. 60):

$$P(\vec{d}) = \int_{f_1, f_2, \dots, f_N} P(\vec{d}, \vec{f}) d^N f. \quad (64)$$

The prior probability $P(\vec{f})$ is the probability of getting \vec{f} without any data information. The derivation of $P(\vec{f})$ follows the “monkey argument” argument (see Ref. [108] and references therein): let a team of monkeys throw balls at N different cells ($i = 1, 2, \dots, N$) independently and at random with Poisson expectations \mathbf{m} . The probability to get exactly the combination \vec{n} of occupation numbers n_i is known (from symmetry and straightforward counting of possible outcomes [108]) to be

$$P(\vec{n} | \vec{m}) = \prod_{i=1}^N \frac{\mathbf{m}_i^{n_i} \exp(-\mathbf{m}_i)}{n_i!}. \quad (65)$$

In order to allow for continuous functions we define $f_i = n_i / \mathbf{a}$ and $m_i = \mathbf{m}_i / \mathbf{a}$, where \mathbf{a} is a positive, constant scaling factor. Together with Stirling’s formula (large n_i) Eq. 65 becomes

$$P(\vec{f} | \vec{m}, \mathbf{a}) = \prod_{i=1}^N f_i^{-1/2} \cdot \frac{\exp(\mathbf{a} S)}{Z_S(\mathbf{a})} \quad (66)$$

$$\text{with } Z_S(\mathbf{a}) = \left(\frac{2\mathbf{p}}{\mathbf{a}} \right)^{N/2} \quad \text{and} \quad S = \sum_{i=1}^N f_i - m_i - f_i \ln \frac{f_i}{m_i}.$$

The quantity S is called “entropy” in analogy to the similar definition in the fields of thermodynamics and information theory. Due to the entropic prior the entire technique described here is called “Maximum Entropy Method” (MEM).

The expectation values \vec{m} can be in principle chosen arbitrarily, thus \vec{m} is called the “model” for the result. Usually there is no reason to favor certain data points, hence we choose $m_i = m$. Moreover, in the case of a convolution with a normalized apparatus function the total intensity is conserved, therefore we use for the model the average value of the spectrum:

$$m_i = m = \frac{1}{N} \sum_{i=1}^N d_i. \quad (67)$$

We henceforth keep \vec{m} fixed and do not consider anymore the dependency in $P(\vec{f} | \vec{m}, \mathbf{a})$ explicitly. In practice the choice of \vec{m} is not crucial for the result, in particular if the adaptive kernel method is applied (cf. Appendix 11.2.4), due to its large number of internal degrees of freedom.

The entropy S is positive, convex with respect to \vec{f} , and has a single maximum at $\vec{f} = \vec{m}$. It does not involve any correlations between the different f_i since arbitrary permutations do not change its value. These properties facilitate the application of effective algorithms and are thus important for the implementation of the Maximum Entropy Method.

It should be mentioned that Eq. 66 can also be derived from more fundamental considerations [107]. The product

$$M(\vec{f}) = \prod_{i=1}^N f_i^{-1/2} \quad (68)$$

in the left hand part of Eq. 66 has been interpreted in terms of the entropy metric, rather than assigning it to the entropy, because $\ln(f_i)$ is not an additive quantity [108]. It is possible to ignore this “measure” $M(\vec{f})$ if it is taken into account again as a volume element in integrals (or sums) over the \vec{f} space [109]. Then the insertion of Eq. 63 and Eq. 66 into Bayes’ theorem (Eq. 62) yields

$$P(\vec{f} | \vec{d}, \mathbf{a}) \propto \exp(\mathbf{a}S - L). \quad (69)$$

The most probable solution \vec{f}_{\max} can be obtained by maximizing $\mathbf{a}S - L$ over all f_i . Due to the special properties of S and L (see above) this N dimensional optimization is feasible in an acceptable short time.

The remaining scaling parameter \mathbf{a} acts as a regularization parameter between the pure maximum entropy solution $\vec{f}_{\max} = \vec{m}$ (for $\mathbf{a} \rightarrow \infty$) and the maximum likelihood result of Eq. 56 (for $\mathbf{a} \rightarrow 0$). Unfortunately the solution is strongly dependent on \mathbf{a} . A simple way to determine a reasonable value for the regularization parameter is the “Historic Maximum Entropy” approach: starting from the fact that the difference between the actual data points and the ideal (noiseless) convolution (Eq. 55) is of the order of \mathbf{s}_i , it suggests to maximize S under the constraint $\mathbf{c}^2 = N$, i.e., to select that \mathbf{a} resulting in a \vec{f}_{\max} which satisfy this constraint [109]. Although this method has been successfully used in different applications,

Historic Maximum Entropy is not Bayesian and hence imperfect. It systematically tends to overestimate the regularization parameter \mathbf{a} which leads to a larger entropy weighting in Eq. 69. The result is a smoother output, biased artificially towards the original data \vec{d} (see Ref. [109] for a discussion).

A decisive advantage of the Bayesian formulation is the capability of parameter estimation. If the problem contains free parameters, the posterior probability cloud can be used to determine e.g. the most probable values for the parameters. This also holds for the regularization parameter \mathbf{a} . The dependence on \mathbf{a} in $P(\vec{f} | \vec{d}, \vec{m}, \mathbf{a})$ can be eliminated by integrating the joint probability in analogy to Eq. 64:

$$P(\vec{f} | \vec{d}) = \int_0^\infty P(\vec{f}, \mathbf{a} | \vec{d}) d\mathbf{a} = \int_0^\infty P(\vec{f} | \mathbf{a}, \vec{d}) P(\mathbf{a} | \vec{d}) d\mathbf{a}. \quad (70)$$

Applying Bayes' theorem on $P(\mathbf{a} | \vec{d})$ yields

$$P(\vec{f} | \vec{d}) \propto \int_0^\infty P(\vec{f} | \mathbf{a}, \vec{d}) P(\vec{d} | \mathbf{a}) P(\mathbf{a}) d\mathbf{a}. \quad (71)$$

In practice, for realistically large datasets the evidence $P(\vec{d} | \mathbf{a})$ is strongly peaked around its maximum value $\hat{\mathbf{a}}$, hence the integration in Eq. 71 may be replaced by the contribution at $\mathbf{a} = \hat{\mathbf{a}}$ [109]. Furthermore, we do not need to assign the prior probability $P(\mathbf{a})$ explicitly since any plausible prior is overwhelmed by $P(\vec{d} | \mathbf{a})$. With this ‘‘evidence approximation’’ Eq. 71 becomes

$$P(\vec{f} | \vec{d}) \propto P(\vec{f} | \hat{\mathbf{a}}, \vec{d}), \quad (72)$$

and the remaining task is to find the most probable regularization value $\hat{\mathbf{a}}$, i.e., to determine the maximum of the evidence $P(\vec{d} | \mathbf{a})$. The combination of Eqs. 61, 63, 64 and 66 results in

$$\begin{aligned} P(\vec{d} | \mathbf{a}) &= \int_{f_1, f_2, \dots, f_N} M(\vec{f}) P(\vec{d}, \vec{f} | \mathbf{a}) d^N f \\ &= \int_{f_1, f_2, \dots, f_N} \frac{M(\vec{f})}{Z_S(\mathbf{a}) Z_L} \exp(\mathbf{a} S(\vec{f}) - L(\vec{f})) d^N f. \end{aligned} \quad (73)$$

The numerical solution of the multidimensional integral is not possible on appropriate time scales for large data sets. Therefore the joint probability $P(\vec{d}, \vec{f} | \mathbf{a})$ is usually

approximated by a Gaussian about its maximum $\vec{f} = \vec{f}_{\max}$ and the integral in Eq. 73 is calculated analytically by extending the lower integration limit to $-\infty$ [108]. The errors implied by this approximations are rather low for typical deconvolution applications and can be even accounted for by the introduction of a correction factor [110] or by more sophisticated integration methods [111].

The basic algorithm for this ‘‘Classic Maximum Entropy Method’’ can be summarized as follows:

1. input data are the spectrum \vec{d} , its errors \vec{s} , and the apparatus function \vec{a} . Start with $\vec{f} = \vec{f}_0$, e.g. $\vec{f}_0 = \vec{d}$, and $\mathbf{a} = \mathbf{a}_0$.
2. maximize $\mathbf{a}S - L$ with respect to \vec{f} .
3. use \vec{f}_{\max} from step 2 to compute the evidence $P(\vec{d} | \mathbf{a})$ in Gaussian approximation.
4. change \mathbf{a} and go back to step 2; iterate \mathbf{a} towards the maximum of $P(\vec{d} | \mathbf{a})$, yielding $\hat{\mathbf{a}}$.

With $\hat{\mathbf{a}}$ the posterior probability is given by

$$P(\vec{f} | \vec{d}) = \frac{\exp(\hat{\mathbf{a}}S(\vec{f}) - L(\vec{f}))}{Z_S(\hat{\mathbf{a}})Z_L P(\vec{d} | \hat{\mathbf{a}})}, \quad (74)$$

and its maximum within the Gaussian approximation is located at $\vec{f} = \vec{f}_{\max}$.

It should be emphasized that the solution of the MEM is the entire N dimensional posterior probability cloud $P(\vec{f} | \vec{d})$. The maximum posterior (MAP) \vec{f}_{\max} is only one particular representation for $P(\vec{f} | \vec{d})$. Another interpretation is given by the pointwise expectation

$$\langle f_i \rangle = \int_{f_1, f_2, \dots, f_N} f_i \cdot P(\vec{f} | \vec{d}) d^N f, \quad (75)$$

which results in generally smoother functions [86]. Accordingly, the variance $\langle f_i^2 \rangle - \langle f_i \rangle^2$ provides an estimate of the accuracy of the solution. Unfortunately, the N dimensional integrals require sophisticated numerical integration techniques, such as the Markov Chain Monte Carlo method (MCMC). However, a rough estimation of the statistical error can be

obtained from the Gaussian approximation of $P(\vec{d}, \vec{f} | \mathbf{a})$ (see above) through the widths \mathbf{s}_i^G of the N dimensional Gaussian in the i^{th} direction. Each width \mathbf{s}_i^G is inversely proportional to the corresponding diagonal element of the Hessian

$$H_{ij} = \frac{\partial^2}{\partial f_i \partial f_j} \ln[P(\vec{d}, \vec{f} | \mathbf{a})], \quad (76)$$

which is anyway computed in every iteration for the Gaussian approximation (step 3 in the algorithm above). The evidence approximation and the extension of the lower integration limit usually result in an overestimated width of the posterior probability distribution [110]. Hence, the confidence interval calculated from Eq. 76 represents an upper limit of the actual uncertainty.

11.2.4 Adaptive Kernels

The Classic Maximum Entropy Method as described in the previous section has been successfully used for various applications. Compared to Fourier methods the amplitude of the residual oscillations are significantly reduced. However, for noisy data and near sharp features the remaining ringing phenomenon may still be of the same order of magnitude as the signal itself (cf. Fig. 76 below). Probably it is this unreliability which resulted in a widespread skepticism towards Maximum Entropy based deconvolution techniques among experimentalists. The ‘‘Adaptive Kernel’’ MEM [86,87] essentially overcomes these problems and is summarized in this subsection.

At first glance a decisive property of the Classic MEM is the absence of any free parameters. In contrast to Fourier based methods or so-called Maximum Likelihood techniques the result cannot be tuned by adjusting parameters and it thus seems to be objective. But at closer inspection artifacts like the ringing phenomenon are dependent on the data point distance, rather than on details of the experimental output like the noise contribution. Changing the data point density affects the MEM result. Therefore, from theoretical point of view, the detailed experimental settings during the data acquisition serve as hidden free parameters. The reason is the number of degrees of freedom (DOF) of the problem: the algorithm as described above optimizes all N values of the posterior function \vec{f} , but the effective number of degrees of freedom (EDOF) of the problem is usually lower due to correlations of neighboring data points [87]. The entropy (cf. Eq. 66) neglects such intrinsic correlations, leading in practice to an underestimation of the

information content. A common way to introduce correlations within the MEM is the concept of a “hidden function” \bar{h} [109]. The MEM analysis is performed on \bar{h} and the posterior function is replaced by

$$\bar{f} = B\bar{h}. \quad (77)$$

The correlation matrix B typically represents a convolution of the hidden function with a Gaussian of the width b (the so-called intrinsic correlation function, ICF) in analogy to the definition in Eq. 55. The entropy is evaluated from the uncorrelated \bar{h} , while the likelihood contains the deviations from the ideal data set

$$\bar{d} = A\bar{f} = AB\bar{h}. \quad (78)$$

The entire algorithm is still valid if the matrix A is replaced by AB . The remaining parameter b which determines the degree of intrinsic correlations can be calculated in complete analogy to the regularization parameter \mathbf{a} (see Appendix 11.2.3). The computational cost increases essentially due to the two-dimensional optimization (\mathbf{a} and b) instead of the one-dimensional case for the Classic MEM.

A major disadvantage of the hidden-function concept is a similar one as for constrained Fourier methods: the intrinsic correlation function restricts the frequency space of the posterior function, thus the reconstruction of sharp spectral features (compared to the width of the ICF) is impossible.

Besides a few sharp features a typical spectrum contains smooth regions with high intrinsic correlations. In the “Adaptive Kernel” (AK) approach the width of the ICF is permitted to vary with i , i.e., the ICF is adapted to the local characteristics of the data. The introduction of a convolution with a varying Gaussian kernel changes the ICF matrix to

$$B_{ij} = \frac{1}{\sqrt{2\pi}b_i} \exp\left[-\frac{1}{2}\left(\frac{i-j}{b_i}\right)^2\right] \quad ; \quad b_i > 0. \quad (79)$$

This definition does only make sense if b varies smoothly compared to the data point distance. Such a “constraint” can be included via the prior probability for a set \bar{b} of kernel widths. We choose the Gaussian prior for the distances between two neighboring kernel widths [86]:

$$P(\bar{b}) \propto \exp\left[-\frac{1}{2}\sum_i (b_i - b_{i-1})^2\right] \quad ; \quad b_i > 0. \quad (80)$$

The Adaptive Kernel method allows to reconstruct sharp peaks as well as smooth regions in the same spectrum (see Fig. 76b). Only at extremely sharp edges a residual ringing phenomenon is observable. The disadvantage compared to the Classic MEM is the computational cost: we now have to optimize $N+1$ parameters (\mathbf{a} and b_i) simultaneously. Sophisticated techniques have to be applied to achieve a stable solution in an acceptable time. For the examples in this work we used a modified conjugate gradient method. The time needed for the deconvolution of a 100-point data set is about 20 min on a standard desktop computer (1.4 GHz Athlon). Due to determinant calculations and matrix inversions the computational cost increases according to $N^{3..4}$. Therefore, large data sets with $N > 200$ should be split before deconvolution. However, in contrast to other methods where multiple deconvolutions are necessary in order to optimize free parameters, it is sufficient to apply the AK-MEM only once since free parameters do not exist.

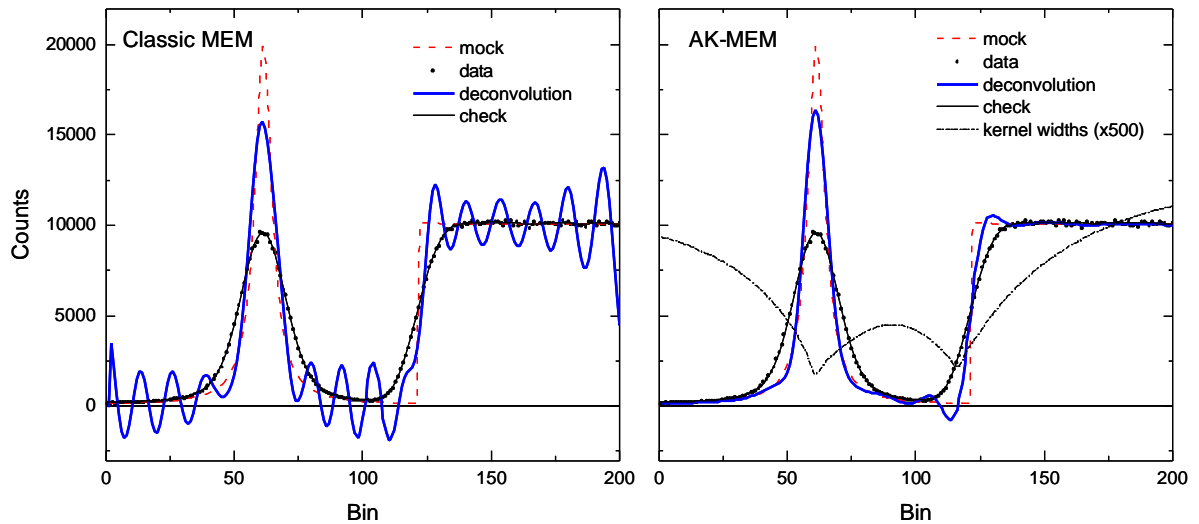


Fig. 76. Comparison of the deconvolution by the Classic MEM (left) and the AK-MEM (right), respectively. The intrinsic model function (“mock”, red dashed line) consists of a Lorentzian and a step function. The “experimental” spectrum \vec{d} (dots) was obtained by convolution of the intrinsic function with a Gaussian apparatus function \vec{a} ($s = 7$ data points) and subsequently adding Gaussian distributed random noise. The result \vec{f} of the deconvolution of \vec{d} and \vec{a} is indicated by a blue thick line and should ideally match the mock function. The convolution of \vec{f} and \vec{a} (“check”, thin solid line) can be used for a reliability check since it should match the data \vec{d} apart from the noise. The local kernel widths \vec{b} (dash-dotted line) in the AK-MEM plot exhibit two distinct minima at the positions of the Lorentzian and the edge, respectively.

The AK-MEM is completely Bayesian and in general all extensions made originally for the Classic MEM are applicable. The algorithm implemented in this work includes as additional features automatic noise scaling [109] and the consideration of positive and negative functions [112]. The first one allows to determine automatically an overall error scaling factor which is important if the absolute number of counts and therefore the errors s_i are not available or if the counter output does not reflect the correct statistics (e.g. multiple pulses per count). Though it appears to be unphysical to take into account negative probability functions, there are at least two reasons: first, in many practical cases a background signal is subtracted from the raw spectra which often results in negative data points due to noise. Secondly, even if all data are expected to be positive it may make sense to allow for negative values in order to check the reliability of the outcome. A further advantage is the numerical stability. Since $\lim_{f_i \rightarrow 0} (\ln f_i) = -\infty$, the evaluation of quantities containing the entropy (or one of its derivatives) causes problems for small f_i , whereas the redefinition of the entropy allowing for negative distributions according to [112]

$$S = \sum_{i=1}^N \tilde{f}_i - 2m_i - f_i \ln \frac{\tilde{f}_i + f_i}{2m_i} \quad ; \quad \tilde{f}_i = \sqrt{f_i^2 + 4m_i^2} \quad (81)$$

does not show the critical behavior.

11.2.5 Smoothing

A slightly surprising application for the AK-MEM is the data smoothing in the absence of any free parameters. In the context of the Bayesian probability theory smoothing means to find the best estimator for the corresponding noiseless data. Instead of “smoothing” a more appropriate description would be “removing noise”. The entropic prior and the adaptive kernel naturally impose smoothness on the posterior function. By setting the convolution matrix to unity ($A = E$) the inverting aspect is suppressed and the AK-MEM acts as a powerful smoothing tool [87]. Again the decisive advantages are the objectivity (no free parameters) and the ability to account for sharp features and smooth regions simultaneously. The high computational effort however restricts the application to selected problems where the correct consideration of the statistical properties is crucial.

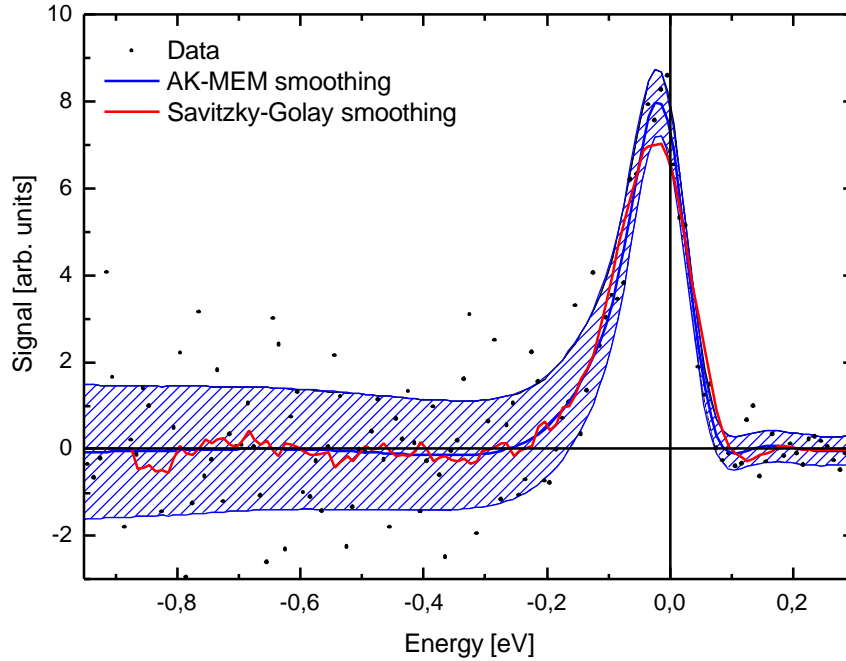


Fig. 77. Example data set (dots) for the AK-MEM smoothing technique. The AK-MEM result (MAP) is indicated by a blue solid line together with the confidence interval (hatched area). For comparison an optimized Savitzky-Golay smoothing result is shown (red dashed line).

In Fig. 77 an example data set is shown (dots) which was generated by the deconvolution of two step-like functions using the “Edge Deconvolution” technique (see Appendix 11.3). The noisy data can effectively be smoothed by the AK-MEM (thick solid line) without suppressing the main peak. This example indicates the afore mentioned overestimation of the confidence interval (hatched area) deduced from the Hessian of the posterior probability distribution (see Appendix 11.2.3), since the true noiseless curve as determined “by the eye” remains clearly inside the hatched area. One of the most powerful and widely used conventional smoothing techniques is the Savitzki-Golay algorithm [113] which is based on a fit of local polynomials. It requires two parameters, the degree of the polynomial and the local fitting interval. The result of this algorithm with optimized parameters (second order polynomial; 21 points interval) is added in Fig. 77 (dashed line). It is clearly visible that the peak is significantly damped, whereas in the smooth region a considerable noise amplitude remains.

An attractive application of the AK-MEM smoothing technique is the determination of the apparatus function \vec{a} [87]. Usually measured apparatus functions are not suited for a direct deconvolution because in contrast to the noise in the spectrum \vec{d} the uncertainty of

the a_i values is not taken into account. The AK-MEM smoothing removes the noise of the measured apparatus function and the result is appropriate for a subsequent AK-MEM deconvolution. This procedure is completely based on the Bayesian probability theory and is thus self-consistent. It has been suggested to include the error of the apparatus function explicitly [114] but this extension is not implemented in the present algorithm.

11.3 “Edge Deconvolution” Technique

For the experimental determination of the distribution of energy shifts $P(W)$ within the dynamic final state effect (cf. Chapter 8) or of the apparatus function $g(E)$ (cf. Sec. 9.1) one can use the measured UPS Fermi edges. At low temperatures the intrinsic thermal broadening is negligible compared to the experimental resolution and $g(E)$ is the result of a deconvolution of two step-like functions. For extremely sharp steps the AK-MEM (cf. Appendix 11.2.4) induces ringing artifacts around the edge, hence the result $g(E)$ is hardly useful for a subsequent utilization. If the density of states was constant near the Fermi level, the low temperature limit of the Fermi edge would be the step function

$$f(E) = b \Theta(E_F - E), \quad (82)$$

where b is the density of states at the Fermi energy E_F . The convolution of $f(E)$ with the apparatus function $g(E)$ is then the simple integral

$$d(E) = f(E) \otimes g(E) = b \int_{-\infty}^{E_F} g(E - \tilde{E}) d\tilde{E}, \quad (83)$$

thus the apparatus function can be directly obtained from the derivative of the measured data $d(E)$. Unfortunately in most UPS measurements the signal amplitude is not constant within the width of the Fermi edge. But often the linear approximation

$$f(E) = (aE + b) \Theta(E_F - E) \quad (84)$$

is able to describe the data sufficiently (see e.g. Fig. 60). The insertion of Eq. 84 into the convolution yields

$$d(E) = \int_{-\infty}^{\infty} (aE - a\tilde{E} + b) \Theta(E_F - E + \tilde{E}) g(\tilde{E}) d\tilde{E}. \quad (85)$$

By differentiating with respect to E we obtain

$$d'(E) = a \int_{E-E_F}^{\infty} g(\tilde{E}) d\tilde{E} - (aE_F + b) g(E - E_F). \quad (86)$$

This integral equation can easily be solved with an iterative procedure in order to extract $g(E)$. An explicit application is presented in Sec. 9.1. Since the numerical derivatives increase the relative noise, usually either the experimental spectrum $d(E)$ or the result

$g(E)$ has to be smoothed. If the AK-MEM (cf. Appendix 11.2.5) is applied for this purpose, in practice it turns out to be more efficient to smooth $g(E)$ subsequent to the deconvolution because this function is normally rather symmetric in contrast to the Fermi edge $d(E)$ (cf. discussion in Appendix 11.2.4). A decisive advantage of the “Edge Deconvolution” method is the low computational effort.

12 References

- [1] N. E. Christensen and B. O. Seraphin, *Phys. Rev. B* **4**, 3321 (1971); P. Pyykkö, *Chem. Rev.* **88**, 563 (1988).
- [2] W. D. Knight, K. Clemenger, W. A. de Heer, W. A. Saunders, M. Y. Chou, and M. L. Cohen, *Phys. Rev. Lett.* **52**, 2141 (1984); M. M. Kappes, R. W. Kunz, and E. Schumacher, *Chem. Phys. Lett.* **91**, 413 (1982).
- [3] O. Echt, K. Sattler, and E. Recknagel, *Phys. Rev. Lett.* **47**, 1121 (1981).
- [4] U. Heiz and W.-D. Schneider, in *Metal Clusters at Surfaces* ed. K.-H. Meiwes-Broer (Springer, Berlin Heidelberg, 2000).
- [5] J. A. Barker, *J. Phys.* **38**, C2-37 (1977).
- [6] G. Binnig, H. Rohrer, Ch. Gerber, and E. Weibel, *Phys. Rev. Lett.* **49**, 57 (1982).
- [7] G. Binnig and H. Rohrer, *Hel. Phys. Acta* **55**, 726 (1982).
- [8] H.-J. Güntherodt, R. Wiesendanger, *Scanning Tunneling Microscopy I* (Springer Berlin Heidelberg New York, 1994).
- [9] M. Henzler and W. Göpel, *Oberflächenphysik des Festkörpers* (B. G. Teubner, Stuttgart, 1991).
- [10] J. Tersoff and D. R. Hamann, *Phys. Rev. Lett.* **50**, 1998 (1983).
- [11] J. Tersoff and D. R. Hamann, *Phys. Rev. B* **31**, 805 (1985).
- [12] R. S. Becker, J. A. Golovchenko, D. R. Hamann, and B. S. Swartzentruber, *Phys. Rev. Lett.* **55**, 2032 (1985).
- [13] J. Lehmann, M. Mersdorf, A. Thon, S. Voll, and W. Pfeiffer, *Phys. Rev. B* **60**, 17037 (1999).
- [14] B. Grimm, Ph.D. thesis, University of Dortmund (2000).
- [15] S. Hüfner, *Photoelectron spectroscopy* (Springer, Berlin Heidelberg New York, 1995).
- [16] W. Shockley, *Phys. Rev.* **56**, 317 (1939).
- [17] A. Zangwill, *Physics at Surfaces* (Cambridge University Press, Cambridge, 1996).
- [18] N. V. Smith, *Phys. Rev. B* **32**, 3549 (1985).
- [19] W. Berthold, F. Rebenrost, P. Feulner, and U. Höfer, *Appl. Phys. A* **78**, 131 (2004).
- [20] T. Andreev, I. Barke, and H. Hövel, *Phys. Rev. B* **70**, 205426 (2004).

- [21] H. Hövel, Th. Becker, A. Bettac, B. Reihl, M. Tschudy, and E.J. Williams, *J. Appl. Phys.* **81**, 154 (1997).
- [22] H. Hövel, *Appl. Phys. A* **72**, 295 (2001).
- [23] H. Chang and A. J. Bard, *J. Am. Chem. Soc.* **113**, 5588 (1991).
- [24] T. Irawan, diploma thesis, University of Dortmund (2003).
- [25] T. Irawan, I. Barke, H. Hövel, in press.
- [26] H. Hövel, T. Becker, D. Funnemann, B. Grimm, C. Quitmann, and B. Reihl, *J. Electr. Spectr. Rel. Phen.* **88-91**, 1015 (1998).
- [27] H. Hövel, B. Grimm, M. Pollmann, and B. Reihl, *Phys. Rev. Lett.* **81**, 4608 (1998).
- [28] H. Hövel, B. Grimm, M. Pollmann, and B. Reihl, *Eur. Phys. J. D* **9**, 595 (1999).
- [29] H. Hövel, B. Grimm, M. Bödecker, K. Fieger, and B. Reihl, *Surf. Sci.* **463**, L603 (2000).
- [30] J. C. Heyraud and J. J. Metois, *Acta Metall.* **28**, 1789 (1980).
- [31] H. Hövel, Th. Becker, A. Bettac, B. Reihl, M. Tschudy, and E.J. Williams, *Appl. Surf. Sci.* **115**, 124 (1997).
- [32] J. Li, W.-D. Schneider, R. Berndt, S. Crampin, *Phys. Rev. Lett.* **80**, 3332 (1998).
- [33] K. H. Hansen, T. Worren, S. Stempel, E. Lægsgaard, M. Bäumer, H.-J. Freund, F. Besenbacher, and I. Stensgaard, *Phys. Rev. Lett.* **83**, 4120 (1999).
- [34] I. Barke and H. Hövel, *Phys. Rev. Lett.* **90**, 166801 (2003).
- [35] H. Hövel and I. Barke, *New J. Phys.* **5**, 31 (2003).
- [36] J. Li, W.-D. Schneider, S. Crampin, and R. Berndt, *Surf. Sci.* **422**, 95 (1999).
- [37] F. Reinert, G. Nicolay, S. Schmidt, D. Ehm, and S. Hüfner, *Phys. Rev. B* **63**, 115415 (2001).
- [38] T. C. Hsieh, T. Miller, and T.-C. Chiang, *Phys. Rev. Lett.* **55**, 2483 (1985).
- [39] Y. Hasegawa and Ph. Avouris, *Phys. Rev. Lett.* **71**, 1071 (1993).
- [40] M. F. Crommie, C. P. Lutz, and D. M. Eigler, *Nature* **363**, 524 (1993).
- [41] S. Pons, P. Mallet, and J.-Y. Veullen, *Phys. Rev. B* **64**, 193408 (2001).
- [42] M. F. Crommie, C. P. Lutz, and D. M. Eigler, *Science* **262**, 218 (1993).
- [43] F. Patthey and W.-D. Schneider, *Surf. Sci.* **334**, L715 (1995).
- [44] G. Neuhold and K. Horn, *Phys. Rev. Lett.* **78**, 1327 (1997).
- [45] L. Limot, T. Maroutian, P. Johansson, and R. Berndt, *Phys. Rev. Lett.* **91**, 196801 (2003).
- [46] J. Kröger, L. Limot, H. Jensen, and R. Berndt, *Phys. Rev. B* **70**, 033401 (2004).

- [47] F. Forster, S. Hüfner, and F. Reinert, *J. Phys. Chem. B* **108**, 14692 (2004).
- [48] K. Morgenstern, K. F. Braun, and K. H. Rieder, *Phys. Rev. Lett.* **89**, 226801 (2002).
- [49] A. Mugarza, A. Mascaraque, V. Repain, S. Rousset, K. N. Altmann, F. J. Himpsel, Yu. M. Koroteev, E. V. Chulkov, F. J. Garcia de Abajo, and J. E. Ortega, *Phys. Rev. B* **66**, 245419 (2002).
- [50] R. W. Baselow and T. D. Cocks, *J. Phys. E: Sci. Instrum.* **13**, 840 (1980).
- [51] U. Lammers and G. Borstel, *Phys. Rev. B* **49**, 17360 (1994).
- [52] G. Wrigge, M. Astruc Hoffmann, and B. v. Issendorff, *Phys. Rev. A* **65**, 063201 (2002).
- [53] M. Brack, *Rev. Mod. Phys.* **65**, 677 (1993).
- [54] J. Pedersen, S. Bjørnholm, J. Borggreen, K. Hansen, T. P. Martin, and H. D. Rasmussen, *Nature* **353**, 733 (1991).
- [55] M. C. Gutzwiller, *J. Math. Phys.* **12**, 343 (1971).
- [56] R. Balian and C. Bloch, *Ann. Phys.* **69**, 76 (1972).
- [57] H. Häkkinen, M. Moseler, O. Kostko, N. Morgner, M. A. Hoffmann, and B. v. Issendorff, *Phys. Rev. Lett.* **93**, 093401 (2004).
- [58] N. Pavloff and S. C. Creagh, *Phys. Rev. B* **48**, 18164 (1993).
- [59] R. Wilkins, E. Ben-Jacob, and R. C. Jaklevic, *Phys. Rev. Lett.* **63**, 801 (1989).
- [60] A. E. Hanna and M. Tinkham, *Phys. Rev. B* **44**, 5919 (1991).
- [61] H.-P. Cheng and U. Landman, *Science* **260**, 1304 (1993).
- [62] K. Bromann, C. Félix, H. Brune, W. Harbich, R. Monot, J. Buttet, and K. Kern, *Science* **274**, 956 (1996).
- [63] R. Anton and I. Schneidereit, *Phys. Rev. B* **58**, 13874 (1998).
- [64] R. Anton and P. Kreutzer, *Phys. Rev. B* **61**, 16077 (2000).
- [65] Z. Wang and P. Wynblatt, *Surf. Sci* **398**, 259 (1998).
- [66] F. A. Nichols and W. W. Mullins, *Trans. Met. Soc. AIME* **233**, 1840 (1965).
- [67] Landolt-Börnstein, New Series, Group III: Condensed Matter, Volume 42, Subvolume A2, Chapter 4.4.7 (Springer, Heidelberg, 2002).
- [68] I. Beszeda, I. A. Szabo, and E. G. Gontier-Moya, *Appl. Phys. A* **78**, 1079 (2004).
- [69] R. L. Schwoebel, *J. Appl. Phys.* **40**, 614 (1969).
- [70] S. C. Wang and G. Ehrlich, *Phys. Rev. Lett* **67**, 2509 (1991).
- [71] R. Ferrando and G. Tréglia, *Phys. Rev. Lett.* **76**, 2109 (1996).
- [72] M. P. Seah and W. A. Dench, *Surf. Int. Anal.* **1**, 2 (1979).

- [73] S.-T. Lee, G. Apai, M. G. Mason, R. Benbow, and Z. Hurych, *Phys. Rev. B* **23**, 505 (1981).
- [74] J. R. Arthur and A. Y. Cho, *Surf. Sci.* **36**, 641 (1973).
- [75] R. B. Barker and H. W. Berry, *Phys. Rev.* **151**, 14 (1966).
- [76] V. Schmidt, *Rep. Prog. Phys.* **55**, 1483 (1992).
- [77] H. Kjeldsen, T. D. Thomas, P. Lablanquie, M. Lavollée, F. Penent, M. Hochlaf, and R. I. Hall, *J. Phys. B* **29**, 1689 (1996).
- [78] B. Kassühlke, R. Romberg, P. Averkamp, and P. Feulner, *Phys. Rev. Lett* **81**, 2771 (1998).
- [79] O. Björneholm, A. Nilsson, A. Sandell, B. Hernnäs, and N. Mårtensson, *Phys. Rev. Lett.* **68**, 1892 (1992).
- [80] M. Astruc Hoffmann, G. Wrigge, and B. v. Issendorff, *Phys. Rev. B* **66**, 041404 (2002).
- [81] M. Seidl, J. P. Perdew, M. Brajczewska, and C. Fiolhais, *J. Chem. Phys.* **108**, 8182 (1998).
- [82] K. Wong, S. Vongehr, and V. V. Kresin, *Phys. Rev. B* **67**, 035406 (2003).
- [83] M. Seidl, K.-H. Meiwes-Broer, and M. Brack, *J. Chem. Phys.* **95**, 1295 (1991).
- [84] H. Hövel, I. Barke, H.-G. Boyen, P. Ziemann, M.G. Garnier, and P. Oelhafen, *Phys. Rev. B* **70**, 045424 (2004).
- [85] Landolt-Börnstein, New Series, Group III: Condensed Matter, Volume 23, Subvolume C1, Chapter 2.9.3 (Springer, Heidelberg, 2003).
- [86] R. Fischer, M. Mayer, W. von der Linden, and V. Dose, *Phys. Rev. E* **55**, 6667 (1997).
- [87] R. Fischer, W. von der Linden, and V. Dose, *Proceedings of the Maximum Entropy Conference 1996*, page 21 (NMB Printers, Port Elizabeth, South Africa, 1997).
- [88] G. Nihoul, K. Abdelmoula, and J. J. Metois, *Ultramicroscopy* **12**, 353 (1984).
- [89] W. Chen, V. Madhavan, T. Jamneala, and M. F. Crommie, *Phys. Rev. Lett.* **80**, 1469 (1998).
- [90] L. Bürgi, H. Brune, and K. Kern, *Phys. Rev. Lett.* **89**, 17 (2002).
- [91] F. Reinert, G. Nicolay, *Appl. Phys. A* **78**, 817 (2004).
- [92] A. Gerlach, R. Matzdorf, and A. Goldmann, *Phys. Rev. B* **58**, 10969 (1998).
- [93] R. Paniago, R. Matzdorf, G. Meister, and A. Goldmann, *Surf. Sci.* **331**, 1233 (1995).

- [94] R. Matzdorf, *Surf. Sci. Rep.* **30**, 153 (1998).
- [95] I. S. Gradshteyn and I. M. Ryzhik, *Tables of Integrals, Series and Products* (Academic Press, Orlando, 1980).
- [96] W. von der Linden, *Appl. Phys. A* **60**, 155 (1995).
- [97] A. Mohammad-Djafari, J. F. Giovannelli, G. Demoment, and J. Idier, *Int. J. Mass Spectrom.* **215**, 175 (2002).
- [98] S. Sibisi, J. Skilling, R. G. Brereton, E. D. Laue, and J. Stauton, *Nature* **311**, 446 (1984).
- [99] C. L. Gilmore, *Acta Cryst.* **A52**, 561 (1996).
- [100] S. F. Gull and G. J. Daniell, *Nature* **272**, 686 (1978).
- [101] E. Pantin and J.-L. Starck, *Astron. Astrophys. Suppl. Ser.* **118**, 575 (1996).
- [102] R. Molina, J. Núñez, F. J. Cortijo, and J. Mateos, *IEEE Sign. Proc. Mag.* **18**, 11 (2001).
- [103] S. F. Gull and T. J. Newton, *Appl. Optics* **25**, 156 (1986).
- [104] A. Jannetta, J. C. Jackson, C. J. Kotre, I. P. Birch, K. J. Robson, and R. Padgett, *Phys. Med. Biol.* **49**, 4997 (2004).
- [105] W. H. Press, S.A. Teukolsky, W. T. Vetterling, and B. P. Flannery, *Numerical Recipes in C*, online version, <http://www.library.cornell.edu/nr/bookcpdf.html> (Cambridge University Press, Cambridge, 1992).
- [106] V. Dose, *Rep. Prog. Phys.* **66**, 1421 (2003).
- [107] E. T. Jaynes, *Probability Theory: The Logic of Science* (Cambridge University Press, 2003).
- [108] J. Skilling, in *Maximum Entropy and Bayesian Methods* ed. P. F. Fougere (Kluwer Academic, Dordrecht, 1990), pp. 341-350.
- [109] S. F. Gull and J. Skilling, *Quantified Maximum Entropy*, “MemSys5” Users’ Manual (Maximum Entropy Data Consultants Ltd., 1999).
- [110] W. von der Linden, R. Fischer, and V. Dose, in *Maximum Entropy and Bayesian Methods* ed. R. N. Silver and K. M. Hanson (Kluwer Academic, Dordrecht, 1996), p. 443.
- [111] W. von der Linden, R. Preuss, and V. Dose., in *Maximum Entropy and Bayesian Methods* ed. W. von der Linden, V. Dose, R. Fischer, and R. Preuss (Kluwer Academic, Dordrecht, 1999).
- [112] M. P. Hobson and A. N. Lasenby, *Mon. Not. R. Astron. Soc.* **298**, 905 (1998).
- [113] A. Savitzky and M. J. E. Golay, *Anal. Chem.* **36**, 1627 (1964).

- [114] V. Dose, R. Fischer, and W. von der Linden, in *Maximum Entropy and Bayesian Methods* ed. G. Erickson (Kluwer Academic, Dordrecht, 1998), p. 147.

Published Papers

- I. Barke, H. Hövel, *Confined Shockley Surface States on the (111) Facets of Gold Clusters*, Phys. Rev. Lett. **90**, 166801 (2003); Ref. [34].
- H. Hövel, I. Barke, *Large noble metal clusters: electron confinement and band structure effects*, New J. Phys. **5**, 31 (2003); Ref. [35].
- H. Hövel, I. Barke, H.-G. Boyen, P. Ziemann, M.G. Garnier, and P. Oelhafen, *Photon energy dependence of the dynamic final state effect for clusters at surfaces*, Phys. Rev. B **70**, 045424 (2004); Ref. [84].
- T. Andreev, I. Barke, H. Hövel, *Adsorbed rare-gas layers on Au(111): Shift of the Shockley surface state studied with ultraviolet photoelectron spectroscopy and scanning tunneling spectroscopy*, Phys. Rev. B **70**, 205426 (2004); Ref. [20].
- T. Irawan, I. Barke, H. Hövel, *Size dependent morphology of gold clusters grown on nanostructured graphite*, in press; Ref. [25].

Acknowledgements

I would like to thank Prof. Dr. Metin Tolan for providing me the opportunity to work within the *Lehrstuhl für Experimentalphysik E1a*. He has a great stake in the pleasant, humorous, and prolific atmosphere of the group and I learned much from his numerous questions, suggestions, and discussions including topics concerning the fringes of physics.

I am especially grateful to my supervisor Priv. Doz. Dr. Heinz Hövel. His enormous physical and technical know-how and his impressive scientific overview have significantly contributed to the success of many measurements and analyses. Thanks to his friendly way and his cooperative attitude I was never afraid of asking any kind of questions which often led to fruitful discussions. He fully supported my work on the (in some respects exotic) field of Maximum Entropy Methods. Furthermore, I want to thank him for his advice and support for planning my future career.

I thank Prof. Dr. Manfred Bayer for his interest in this work and for kindly agreeing to referee the thesis.

Many of the experiments have been done in close cooperation with Thomas Andreev and Thomas Irawan, and several results are part of their diploma theses. They contributed with excellent ideas and practical work in the laboratory and I enjoyed the pronounced teamwork.

For the most part of my diploma and Ph.D. time I worked together with my colleague Christian Rettig. I savored all the scientific discussions, but also the recreational activities including the weekly badminton matches. He really managed to establish a good mood in our bureau.

I would like to thank Priv. Doz. Dr. Hans-Gerd Boyen (Ulm), Priv. Doz. Dr. Bernd von Issendorff (Freiburg), Dr. Marina Pivetta (Lausanne), Dr. François Patthey (Lausanne), and Prof. Dr. Wolf-Dieter Schneider (Lausanne) for the fruitful and successful collaborations. I thank Dr. Frank Katzenberg (Dortmund) for performing the TEM measurements.

Without the reliable supply of liquid helium and nitrogen by Mr. Eberhard Gall most of the experiments would not have been possible. Many thanks also to Mrs. Susanne Fricke and the team of the mechanical workshop, as well as to Mrs. Gisela Pike and Mr. Dirk Schemionek for numerous technical workings.

I thank Daniel Boecker, Farhad Ghaleh, and all the other members of the group E1a for the pleasant cooperation and the wonderful time.

I acknowledge the *Deutsche Forschungsgemeinschaft* (DFG) for the financial support.

I am indebted to my family for the continuous support for my work. Their strong backing was a great help.

Without the enormous emotional support of my wife Nicola it would have been much more difficult to cope with problems and disappointments which are always unavoidable in three years of research. I am sincerely grateful for her loving care and her motivating spirit.